Field tuned ferromagnetic quantum criticality in Fe-rich $NbFe_2$ itinerant transition metal system

Giri Mani

Submitted in partial fulfilment of the requirements for the degree of

Doctor of Philosophy

Supervisor

Dr. Philipp Niklowitz

Department of Physics
Royal Holloway, University of London
United Kingdom

March 17, 2023

Declaration of Authorship

I, Giri Mani, hereby declare that this thesis and the work presented in it is entirely my own. Where I have consulted the work of others, this is always clearly stated.

Signed: 

Date: 17/03/2023

Abstract

Quantum criticality plays an important role in many area of condensed matter physics. These areas includes unconventional and high temperature superconductivity and heavy fermion physics. The simplest example for quantum criticality is the ferromagnetic one. However nature tends to avoid ferromagnetic quantum critical points. When suppressing ferromagnetic second order phase transitions the transitions become either first order or modulated order emerges. The system $NbFe_2$ is a prime candidate of the latter. Additionally large single crystals exist which have allowed neutron scattering to study the order and excitations across the composition temperature phase diagrams. In this work the evolution of the $NbFe_2$ system with field has been explored. The Fe-rich samples studied contained a ferromagnetic (FM) ground state and spin density wave (SDW) and paramagnetic phase at higher temperature. Longitudinal fields H‖c and transverse fields H‖a have been applied.

With magnetic neutron diffraction in longitudinal fields the location of a tricritical point (TCP) has directly been observed at H_{tr}=53 mT and T_{tr} = 26.5 K. In magnetic neutron diffraction in transverse field suppression of SDW order has been observed but it was not possible to follow the unmasked FM-PM to low temperature. With inelastic neutron scattering in longitudinal field the evolution of spin fluctuations across the TCP has been observed. The TCP has been found to feature simultaneously enhanced and soft FM and SDW spin fluctuations. With inelastic neutron scattering in transverse field the ferromagnetic low energy excitations have been observed to show softening and an enhancement that indicate existence of a field induced unmasked ferromagnetic quantum critical point.

Acknowledgements

The completion of this thesis could not have been realized during the Covid pandemic without continuous mental and practical support from many people whom I would like to thank for their contributions both directly and indirectly to this thesis. First and foremost, I would like to express my sincere thanks to my supervisor Dr Philiip Niklowitz for selecting me as a PhD student and for providing me with excellent supervision, motivation and for explaining the theoretical concepts patiently as many times as I wanted. I am very grateful to him and the university for this opportunity that I was given to explore the fascinating area of neutron scattering and to get involved in the experiments internationally. To my thesis advisory committee, Dr Keith Refson and Dr Veronique Boisvert collectively, I would like to thank you for challenging my knowledge and for advising me in developing the thesis. I also would like to thank Dr Marijn for his support in analysing the neutron scattering data, helping me out with the technical support of the experiments and the fruitful discussions on our research projects. I express my sincere thanks to Dr Uthay Sivaperumal for his constant encouragement and for extending any help whenever I needed even if it is other than academic-related. I would like to express my deepest gratitude to Royal Holloway, University of London for awarding the College studentship and SEPnet for the travel grant to support the research-related travel in various neutron scattering facilities across the world. I also owe a great deal to the beam scientists Dr Jean-Michel Mignot at LLB-France, Dr Markos Skoulatos and Dr Robert Georgii at FRM2 - Germany, Dr Vladimir Hutanu at FRM2 - Germany, and Dr David Voneshen and Robert Bewley at ISIS - UK for their immense support in gathering the neutron data and helping me out with its analysis.

The PhD at Royal Holloway wouldn't be possible without the research experiences that I gained from the Indian Institute of Science Education and Research – Pune (IISER Pune),

India. I'm extremely grateful to Dr Surjit Singh and IISER Pune for selecting me as a junior research fellow. I would like to thank Dr Luminita Harnagea for teaching me various crystal growth techniques and instruments to carry out the experiments. I extend my thanks also to Dr Justin Josephus at the National Institute of Technology – Trichy (NIT Trichy), India for introducing the world of research during my Master's studies.

This journey would not have been fruitful without my office mates with whom I had a wonderful time. I owe a debt of thanks to Dr Timothy Lehner, Dr Rupert Mellor, Dr Saeed Ascroft, Dr Stefanos Dimitriadis, Petra Hrubcova, Terje Theisen, Tom Northam De La Fuente and Dr Adithya for introducing me to the endless new games, movies, discussions and so on. Special thanks to Stefanos for teaching me fire dance and martial arts Nunchucks and Petra for Czechoslovakian special sweets and cakes.

This endeavour would not have been possible without my friends, close or far away they contributed a lot to maintaining my mental wellbeing during the whole journey. I would like to thank Dr Sercan Arsalan whom I have started my PhD together, for making my days at Royal Hollway truly joyful with his companionship. I thank my best buddies Sebin Devasia, Dr Leela Shri and Nivetha for their support in all my ups and downs. My best buddies from IISER Pune Dr Ajith, Dr Anjusha, Dibyata, Dr Hridya, Kritika, Dr Prachi and Dr Sumit whom I am deeply indebted for endless group calls, discussions, celebrations and for always updating me on everything happening around the world. I would like to thank also my buddies Greeshma Vijay, Dr Hari Vignesh and Arun Prakash for their motivation, encouragement and cheering me up whenever I needed it. I also thank all my house mates and friends at Royal Holloway for their incredible support and love.

My eternal journey in academics would not have been possible without my beloved teachers. Words cannot express my gratitude to Mrs Susamma Thomas, my teacher and parental figure, for always being happy in all my successes and keep supporting me in my all endeavours. I would like to thank Thirumala for her encouragement and for including me in her everyday prayers. I'm extremely grateful to Mis Shantha Kumari and Mis Ammini for their constant support and motivation and also for inspiring me with their creative teaching methods. A special thanks to Mr Loluck Baby for helping me to reach new heights.

Finally, I am immensely grateful to my family as a whole for their understanding and continued support throughout my entire eduaction. Thank you so much for always believing in me and standing behind me in all my decisions.

Contents

List of Figures

List of Tables

1

Introduction & Theoretical Concepts

This chapter is intended to give a brief introduction to the field of magnetic quantum phase transitions and quantum criticality observed in various materials. A focus is on the physics connected to nature's tendency to avoid ferromagnetic quantum critical points the understanding of which is a motivation of this thesis work. Furthermore, important theoretical concepts used within this thesis are introduced.

1.1 Introduction

1.1.1 Emergent phases of electronic matter from magnetic quantum phase transitions

The study of second order phase transition at non zero temperature has been a topic of vivid interest in the condensed matter physics. Many key physical phenomena such as critical opalescence in CO_2, loss of ferromagnetism in iron at the Curie temperature, a puzzle once, are now significantly understood as phenomena of phase transitions in detail. Due to the increased interest in the study of continuous phase transitions many interesting phenomena and materials have been observed to date. Continuous phase transitions play a role outside the field of condensed matter physics, too, such as string theory, transition to chaos in dynamical systems, astrophysics [1] and even in biology [2]. The second order phase transition at finite temperature is referred as classical phase transitions where the thermal fluctuations are dominant in controlling the phases of the system [3].

Research including the field of condensed matter physics has also focussed on a type of phase transition that take place at zero temperature instead of at finite temperature called quantum

phase transition whereby the transitions are driven by the quantum fluctuations demanded by the Heisenberg uncertainty principle [4]. These fluctuations can influence a surprisingly large area of the phase diagram. The quantum phase transition can be tuned using some non thermal control parameter such as composition, magnetic field, pressure *etc.* The point in the phase diagram at which the second order phase transition takes place at zero temperature is called quantum critical point (QCP) [4]. There have been QCPs studied at the border of different types of order including valence order, charge order, or nematic order. The most common types of QCPs studied have been magnetic quantum critical points and within that group AF QCPs in particular.

In several materials it was observed that suppressing antiferromagnetic order to zero temperature an unconventional superconducting phase starts to emerge at QCP [5]. Although magnetism had originally been is thought to be detrimental for superconductivity the observation of the superconducting phase at AFM-QCP hinted that the magnetic spin fluctuations may play an important role for the emergence of superconductivity in contrary to the ordinary superconductors. This unconventional superconductivity has been observed in several heavy fermion metals when the AFM order is suppressed to zero. For example in the case of $CeCu_2Si_2$ heavy fermion metal the superconductivity was observed below T $\approx$ 0.6 K. The Figure.(1.1) shows the the AFM order vanishes as a function of effective coupling constant (g) and around AFM-QCP superconductivity emerges that even extends far into the paramagnetic regime [5].

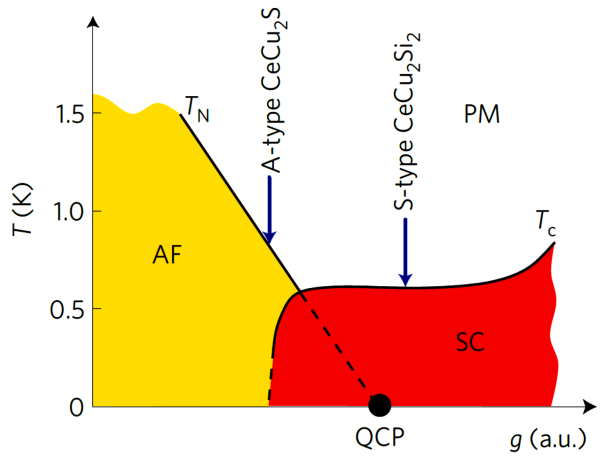

Figure 1.1: Schematic temperature (T) - effective coupling constant (g) phase diagram. Yellow area cover the AFM order and Red area cover the superconducting order. The picture is from [5]

Similarly the unconventional superconductivity was observed in other heavy fermion metals

as well for example $CePd_2Si_2$ and $CeIn_3$ when the AF order suppressed to zero temperature via pressure as a control parameter [6]. Also, in Fe-based superconductor $BaFe_2(As_{1-x}P_x)_2$ when tuning with composition As, the spin density wave (SDW) order is suppressed to zero leading to unconventional superconductivity masking the SDW-QCP [7].

While there are numerous examples available to study the behaviour and the emergence of novel phases when the material approach AFM-QCP, many studies suggest that the FM quantum critical point can rarely be reached in real materials. Instead the system finds a variety of escape routes to avoid the FM-QCP [8, 9]. For instance, the occurrence of a second order phase transition at high temperature becomes the first order phase transition when approaching QCP (Figure.(1.2)a), for example, in the phase diagrams observed in MnSi, $ZrZn_2$ [10, 11]. In this case a tricritical point is found at the end of a triple line where three-phase coexistence terminates. A 3D phase diagram illustrating this situation is shown in Figure.(1.3). Three first-order areas meet in a line of triple points. The areas are terminating in three second order phase transition lines that meet at the tricritical point. In the given example the three dimensions are temperature T, field H, and another control parameter t. Two of the second order transition lines terminate at T=0 in quantum critical points (QCPs) at finite H [12].

In 2D, a tricritical point (TCP) manifests itself as the meeting point of a second order and first order phase transition [13]. Tricritical points are special points in the phase diagrams where the usual scaling laws hold with different set of critical exponents [11]. The existence of TCP's has been experimentally identified in the phase diagrams of several itinerant magnetic systems, including $ZrZn_2$ [14], UGe_2 [15], URhGe [16], MnSi [10, 17], CoS_2 [18], $LaCrGe_3$ [19], $SrRuO_3$ [20], *etc.* The notable example of MnSi is similar to an itinerant ferromagnet that orders below T_C=29.5K by showing helical magnetic structure with a long pitch of 175$\AA$ [10,21]. When tuning MnSi system using pressure the second-order phase transition become first order while approaching the QCP at a critical pressure of P_c=14.6 kbar [10].

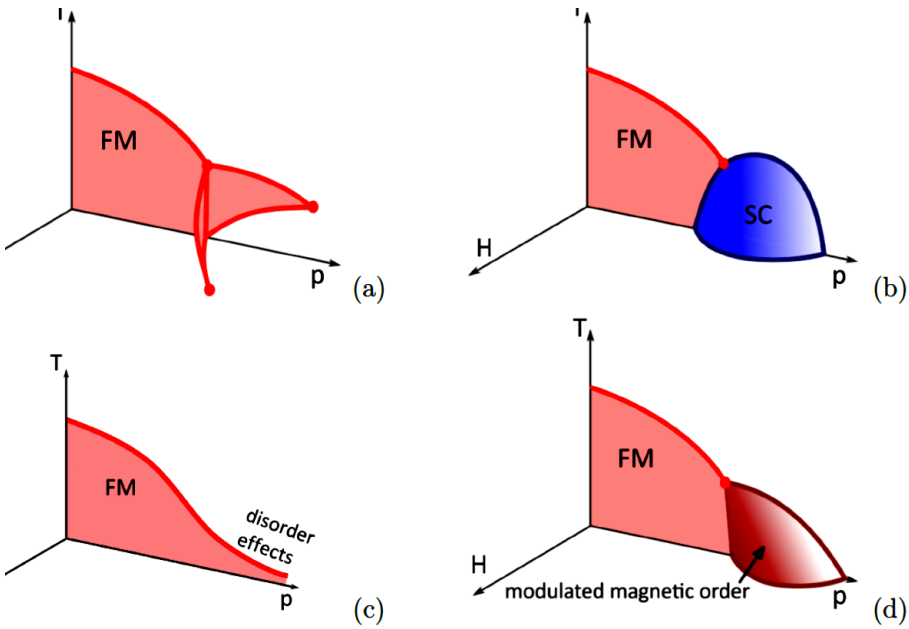

Figure 1.2: The schematic illustrations of avoided FM-QCP by different means. shown are the Temperature(T)- magnetic field(H)- tuning parameter (p) phase diagrams (a): The second order FM-PM phase transition become first order at tricritical point (TCP). With an application of external field, the phase diagram show wing like second order transition lines that terminates at quantum critical end point (QCEP) in H-p plane symmetrically on either side. (b) FM-QCP avoided by the emergence of superconducting order. (c) The FM-QCP in the disordered system is avoided to become crossover to spin glass in the tail of the phase diagram. (d) Emergence of modulated magnetic order at the QCP. The figure is take from [22]

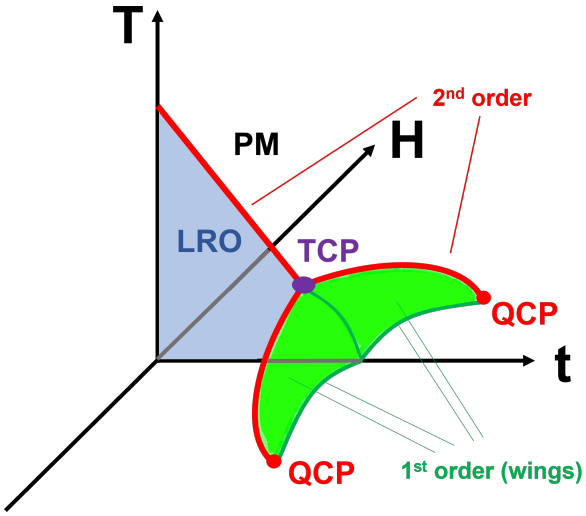

Figure 1.3: Schematic phase diagram of itinerant metallic magnetic system with tricritical point with axes are temperature (T), control parameter (t) and magnetic field (H). The red solid lines show the lines of second order transitions. The green lines and wings ("tricritical wings") shows the first order transitions. The magnetic phases of the transitions shown are paramagnetic phases (PM), long-range magnetic order (LRO). The solid circles show the tricritical point (TCP, purple) and qunatum critical points (QCP, red) [12].

The avoidance of FM-QCP due the emergence of superconducting order illustrated in Figure.(1.2b) seems to occur in systems like UGe_2 [23] or in UCoGe [24] but closer inspection reveals that again the FM QCP is avoided by the occurrence of a first order transition and superconductivity appears on the ordered side of the first order transition.

The third scenario of avoidance (Figure.(1.2)c) is observed in highly disordered systems where the system becomes freezing spin glass on approaching QCP resulting in a tail in the phase diagram beyond the position where the QCP would have been expected [22].

Figure.(1.2d) illustrate a new scenario in which the FM-QCP is avoided by the emergence of modulated magnetic order. The examples include, PrPtAl where the transition at the finite temperature to induced modulated magnetic order is observed and it is believed to mask the putative QCP [25]. In $Sr_3Ru_2O_7$ compound the field tuned metamagnetic QCP is observed to be masked by a novel form of low-temperature including SDW properties [26]. Finally, in $NbFe_2$, the subject of this thesis work the SDW order masks the FM-QCP when tuning the system to zero temperature by using composition or pressure [27, 28].

Many investigations suggest that the concept of the FM-QCP is a key ingredient in under-

standing the new emergent phases of matter including magnetically mediated superconductivity [22]. Therefore pursuing the investigation of such systems should help to understand exotic phenomena like the emergence of new phases of matter. The motivation of this thesis is to learn about the origin of the physics of avoided FM QCPs. A first step can be to gain detailed insight into the magnetic excitation spectra using neutron scattering. This has been possible for the $Nb_{1-y}Fe_{2+y}$ system in zero field due to the availability of large single crystals and direct information on the magnetically ordered states and excitations has been obtained. This work explores magnetic field tuning of this system and its effect on order and excitations.

1.2 Synopsis

This thesis is organised as follows: In the remainder of this chapter we introduce theoretical concepts that are important for this thesis. Chapter(2) is a review of the $Nb_{1-y}Fe_{2+y}$ compound. we present properties such crystal structure, electronic, magnetic, thermal properties of the system as well as the magnetic and composition - temperature phase diagrams of the system. Chapter(3) provides a description of the experimental methods including aspects of neutron scattering theory, instruments and the samples studied. The next three chapters contains the results of our investigations of Fe-rich $Nb_{1-y}Fe_{2+y}$ samples with unpolarised neutron scattering which are divided as follows: Chapter(4) presents the magnetic phase diagrams in H‖c and H‖a using elastic neutron scattering. Chapter(5) longitudinal field evolution of the magnetic excitations measured using inelastic scattering and Chapter(6) presents transverse field evolution of magnetic excitation spectrum measured using inelastic scattering. Chapter (7) summarises the main results and findings with an avenue for future investigation suggested.

1.3 Magnetic order

In solids different types of magnetic interactions that operate between magnetic dipole moments are considered to be crucial to produce various orders or the arrangements of the magnetic moments in the system. Two important aspects in the study of magnetic order concern are the arrangements of the magnetic moments at the ground state and the process of ordering itself, that is, the phase transitions and the critical behaviour near the transitions. Examples for the magnetic grounds states include ferromagnetic, anti-ferromagnetic, ferrimagnetic, helical, spin glass *etc.* In this section we will explore a few examples of these magnetic structures.

1.3.1 Ferromagnetic order

The solids in the ferromagnetic (FM) states have a spontaneous magnetization even in the absence of an external magnetic field. The arrangement of the magnetic moments in the system is that they are all aligned along a single unique direction preferentially. The FM ordering is illustrated in Figure.(1.4).

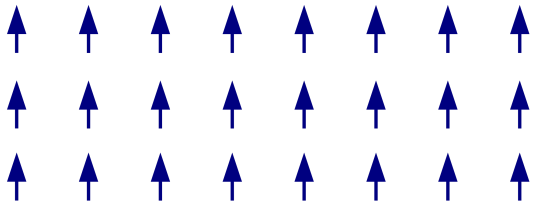

Figure 1.4: Schematic view of the Ferromagnetic order where the magnetic moments are all pointing in a single unique direction. The picture is from [29].

This type of long range magnetic order in the systems is generally due to the exchange interactions [30]. The Hamiltonian for a ferromagnet from the Heisenberg model is given as,

$$\hat{H} = -\sum_{ij} J_{ij} S_i \cdot S_j \tag{1.1}$$

where J_{ij} is an exchange constant between the ith and j^{th} spins. The essential feature of this equation is that when J_{ij} is positive, the energy is minimised when the spins are parallel, which is energetically favourable. When J_{ij} is negative the neighbouring spins are anti-parallel.

The Hamiltonian for the ferromagnet in an applied field (B) is given by,

$$\hat{H} = -\sum_{ij} J_{ij} S_i \cdot S_j + g\mu_B \sum_j S_j \cdot B, \tag{1.2}$$

where the first term in the Equation.(1.2) is the Heisenberg energy and the second term is Zeeman energy. The Weiss model of ferromagnetism solves the Hamiltonian for the observation of spontaneous magnetization in the ferromagnets. It proposes that the alignment of the magnetic moments at the low temperature gives rise to the internal molecular field that causes the alignment in the system in the first place. While the magnetic ordering at low temperature

is self sustaining with increased temperature the thermal fluctuations begin to destroy the ordering and at the critical temperature order is completely suppressed. The Curie-Weiss magnetic susceptibility that describes systems of localised magnetic moments is given as,

$$\chi = \frac{M}{B} = \frac{C_{Curie}}{T} \tag{1.3}$$

where C_{Curie} is the curie constant, $C_{Curie} = n_a \mu_B^2 \mu_{eff}^2$, the terms n_a is the number of magnetic moments per unit volume, μ_B is the Bohr magnetron and μ_{eff} is the effective paramagnetic moment at each lattice site of the system. The internal magnetic field that induces the long range order is proportional to the magnetization, $B_{int} = \lambda M$, where λ is a constant which parametrizes the strength of the molecular field as a function of magnetization. For a ferromagnet $\lambda > 0$. The molecular field in the ferromagnets are often found to be extremely large due the large Coulomb energy involved in the exchange interaction [30]. In such case the magnetic susceptibility can now be expressed as,

$$\chi = \frac{M}{B + \lambda M} = \frac{C_{Curie}}{T} \tag{1.4}$$

or rearranged to,

$$\chi = \frac{C_{Curie}/T}{1 - \lambda C_{Curie}/T} \tag{1.5}$$

therefore the magnetic susceptibility is enhanced by a factor of $1/(1 - (\lambda C_{Curie}/T))$. For T $< \lambda C_{Curie}$ the magnetic order begins to develop [30].

1.3.2 Antiferromagnetic order

If the exchange interaction in the Equation.(1.2) is negative, $J < 0$, the magnetic moments will align anti-parallel to each other, where it is more favourable for the nearest neighbour magnetic moments. A schematic view of the antiferromagnetic (AFM) alignment of the magnetic moments is shown in Figure.(1.5). The adjacent moments are oriented in such a way that one moment points up and the other down. This kind of arrangement can be considered as two inter-penetrating sublattices.

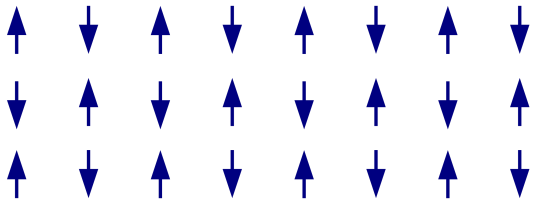

Figure 1.5: Schematic view of the antiferromagnetic order where the ordering of the magnetic moments can be viewed as two interpenetrating sublattices. The picture is from [31].

The Weiss model of an antiferromagnet solves the Hamiltonian (Equation.(1.2)) for this type of magnetic ordering by considering the molecular field on each sublattice (both up and down) given by,

$$\begin{aligned} B_+ &= -|\lambda| M_- \\ B_- &= -|\lambda| M_+ \end{aligned} \tag{1.6}$$

where λ is molecular field constant which is negative now and M_+ and M_- is the magnetization in each sublattice with same value but opposite direction. Therefore the net magnetization of the AFM order is zero. To define a difference between the two magnetizations a quantity called staggered magnetization is defined as a order parameter. This is then zero above the critical temperature of the phase transition.

The magnetic susceptibility calculated from the Weiss model for the antiferromagnet is given as

$$\chi = \frac{1}{T - \theta}, \tag{1.7}$$

where θ is the Weiss temperature. If $\theta = 0$ the antiferromagnetic order is destroyed and the material become paramagnet. If $\theta > 0$ we expect the material become ferromagnet and then $\theta = T_C$. If $\theta < 0$ the material become antiferromagnet therefore $\theta = -T_N$ [30].

1.3.3 Ferrimagnetic order

In the antiferromagnetic ordering it was assumed that the two sublattice magnetizations are equivalent but opposite in its direction, therefore, the net magnetization is zero. In case of any crystallographic reasons in the system that cause the magnetizations in the sublattices to be unequal in its value then there will be a development of net magnetization. This phenomenon of spontaneous magnetization is called ferrimagnetism and the order is called ferrimagnetic order. Because of two different molecular fields at the sublattices, the spontaneous magnetization will have quite different temperature dependence and in addition the net magnetization itself will have complicated temperature dependence. For example if the magnetization at one sublattice dominate at low temperature and other on the high temperature then the net magnetization can be reduced to zero and change sign at a temperature known as compensation temperature. The magnetization in the ferrimagntic order will not follow the Curie-Weiss law [30]. The Schematic figure for the ferri magnetic order is displayed in Figure.(1.6).

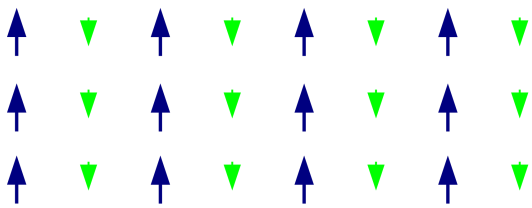

Figure 1.6: Schematic view of the ferrimagnetic order where magnetic moments are unequal and opposite directions. The picture is from [32].

1.3.4 Itinerant ferromagnetism and spin density wave order

In metals, it was observed that the spontaneous spin splitting of the bands, order the system into a ferromagnetic state if the condition of Stoner criterion is met. The total energy change due to the spin split in the system is given by

$$\Delta E = \frac{1}{2} g(E_F)(\delta E)^2 (1 - U g(E_F)) \tag{1.8}$$

where ΔE is the total energy change of the system due to the spontaneous spin split, $g(E_F)$ is density of state at the Fermi level, δE is the change in energy due to spin flip and U is the

Coulomb potential [30]. The system will order ferromagnetically if $\Delta E < 0$, which implies that $(Ug(E_F)) \geq 1$. This condition is called Stoner criterion. For the ferromagnetic instability to satisfy this condition requires that the Coulomb effects are strong and also that the density of states at the Fermi energy is large. If the Stoner criterion is not met then the system will not order into ferromagnetic spontaneously but the susceptibility may be altered which is calculated to be,

$$\chi = \frac{\chi_P}{1 - Ug(E_F)}. \tag{1.9}$$

where χ_P is the Pauli susceptibility. The calculated χ is larger than the χ_P expected without the presence of Coulomb interactions by a factor of $(1 - Ug(E_F))^{-1}$, known as Stoner enhancement [30].

The q-dependent susceptibility of the metals without the presence of Coulomb interactions can be written as,

$$\chi_q^0 = \chi_P f(q/2k_f), \tag{1.10}$$

and is also enhanced by the Coulomb interactions,

$$\chi_q = \frac{\chi_p f(q/2k_F)}{1 - Ug(E_F) f(q/2k_F)} = \frac{\chi_q^0}{1 - \alpha\chi_q^0}, \tag{1.11}$$

where $\alpha = U/\mu_0\mu_B^2$ and $f(q/2k_F)$ is Fermi function. At a value of q which is not equal to zero the χ_q^0 is maximum. If we consider the interactions parametrised by α, the χ_q will diverge when $\alpha\chi_q^0$ reaches unity at this value of q. This causes an oscillatory static magnetization to develop spontaneously in the sample. The special cases $q = 0$ corresponds to ferromagnetic order and $|q| = \pi/a$ corresponds to an antiferromagnetic order. In general, in the metal one can expect a spiral or spin density wave structures with wave vector q [30].

1.4 Phase transitions

In condensed matter, phase transitions are important physical processes that we encounter in our everyday life. In the process of phase transition, the phases of the matters which are characterised by distinct macroscopic properties change when controlled by certain parameters.

For example ice melts to liquid water or a ferromagnet becomes paramagnet when temperature is increased. The former case is an example for the structural phase transition where as the latter one is an example for the magnetic phase transition. In the structural phase transition the changes involved is in the crystal structure, on the other hand, in the magnetic phase transition the magnetic structure of system changes with temperature. Similarly we can observe many other phase transitions in nature which are involved in changing its phases from one to another (e.g, Ferroelectric transitions, superconducting transitions *etc.*). These phase transitions can be provoked by varying parameters such as temperature, pressure or magnetic field in the system.

Though microscopic details of the phase transition are very different, the methods applied to study the phase transitions are universal in nature. Traditionally the phase transitions were characterised based on the behaviour of the thermodynamic free energy as a function of some thermodynamic variables [33]. Paul Ehrenfest classified the phase transitions based on this scheme labelling the nature of the non-analytic behaviour at transition. When two phases coexist at the point of transition they have a common temperature, magnetic field and pressure therefore the Gibbs free energy (G) will be same for both phase at the point of transition. Therefore we can say that the phase transition occur at the point where the G is same for both phases which we can observe as a kink at the phase transition. Based on the nature of the kink in G the phase transitions are classified into different order of transitions. If the nth derivative of G with respect to some control parameter (eg. temperature) is discontinuous then the phase transition is called nth order [34]. For example, in the case of ice melting, the first derivative of the Gibbs free energy with respect to temperature is discontinuous where we observe a change in entropy between two phases while for higher order derivatives the entropy varies continuously, therefore the transition is first order. In the case of second order phase transition, the second derivative of G with respect to T is discontinuous (e.g, Ferromagnetic transition) [34].

Since Ehrenfest classification cannot explain the phase transition in the absence of thermal fluctuations, a more general theory of phase transition was developed by L. D. Landau where he consider a special quantity called order parameter which goes to zero. When there is a symmetry broken on cooling through the critical point, the order parameter will be related to that symmetry. Another important quantity which is central in developing the Landau theory is Landau free energy, which is a constrained Helmholtz free energy for a quasi-equilibrium state,

$$F(B, T : M). \tag{1.12}$$

The conventional Helmholtz free energy $F(B, T)$ is a mathematical function of temperature T and magnetic field B, therefore the system will have the state of equilibrium with Helmholtz free energy $F(B, T)$ when it is specified. Since the system that we have considered here on the other hand have constraints to achieve its full equilibrium state due to the constraints of magnetization to take certain value the equilibrium state of the system is achieved only if the $F(B, T : M)$ is minimised with respect to variations in M, i.e,

$$\frac{\delta F(B, T : M)}{\delta M} = 0. \tag{1.13}$$

This constrained free energy is called Landau free energy [34].

A ferromagnetic phase transition can be described in the following way. The Helmholtz free energy is defined as,

$$F = E - TS, \tag{1.14}$$

where E and S are the internal energy and entropy of the system. In order to obtain the constrained free energy M is kept as an explicit variable. The internal energy and entropy calculated using the Weiss model is,

$$E = \frac{NkT_c}{2} m^2, \tag{1.15}$$

and

$$S = -Nk \sum_j p_j ln p_j, \tag{1.16}$$

where N is the number of spins, k is Boltzmann constant, m is the reduced magnetization ($m = M/M_0$), T_c is the critical temperature and p_j probabilities of the single particle states being occupied. The simplest case of electron with spin 1/2, the entropy can be expressed as,

$$S = \frac{Nk}{2} \Big[2ln2 - (1 + m)ln(1 + m) - (1 - m)ln(1 - m) \Big]. \tag{1.17}$$

Therefore the contained free energy $F = E - TS$, can be written as,

$$F = -\frac{Nk}{2}\Big\{T_c m^2 + T\big[2ln2 - (1+m)ln(1+m) - (1-m)ln(1-m)\big]\Big\}. \tag{1.18}$$

The above equation is plotted for temperature below, equal to and above the critical temperature of the ferromagnetic phase transition in Figure.(1.7).

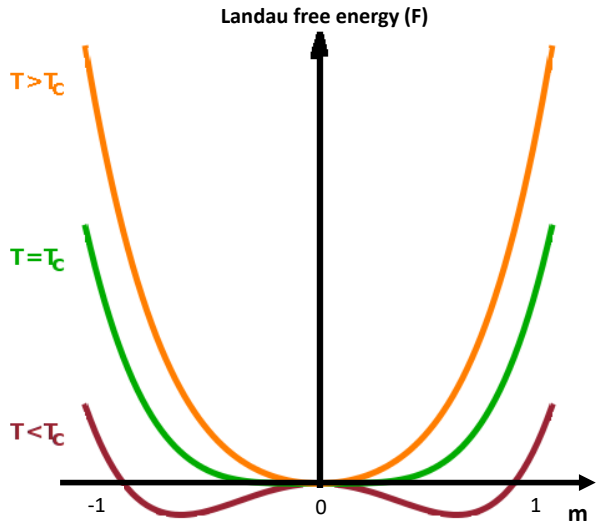

Figure 1.7: Landau free energy for Weiss model ferromagnet. The picture is from [35].

The ordering of the ferromagnetic phase transition can be seen clearly below T_c where two minima on either side of the origin in the Landau free energy are present. Above T_c we can see only a single minimum at $m = 0$. At $T = T_c$ symmetry changes precisely and the values at which Landau free energy is zero can be seen for many m values around $m = 0$, meaning the m make excursion around $m = 0$ at a negligible cost of free energy hence the large fluctuations at the critical points [34].

1.5 Classical magnetic phase transitions

In section(1.4) phase transition in ferromagnetic systems was presented. In the framework of Landau theory, It is assumed that all the spins in the system feel an identical average exchange field produced by all other neighbouring spins, and it is proportional to the magnetization (M)

of the system. Landau's approach to studying the phase transition is called a mean-field theory, and this approach is identical in itself to the Weiss model of ferromagnets [30]. The free energy or otherwise called Landau's free energy of the ferromagnets, therefore, can be expressed as a function of the magnetization M in the power series as follows,

$$F(M) = F_0 + a(T)M^2 + bM^4 \tag{1.19}$$

where F_0 and b are constants (we assume $b > 0$) and $a(T)$ is a temperature-dependent coefficient. The terms with an odd power of M in the series are ignored as there is no energetic difference between up or down spins. An appropriate phase transition in the system is observed if we allow the coefficient $a(T)$ to change sign at the transition temperature T_c, therefore $a(T)$ can be written as,

$$a(T) = a_0(T - T_c) \tag{1.20}$$

where a_0 is a positive constant. The ground state of the system can be found by minimizing Landau's free energy as given in the following equation:

$$\frac{\delta F}{\delta M} = 0 \tag{1.21}$$

this condition implies that,

$$2M[a_0(T - Tc) + 2bM^2] = 0. \tag{1.22}$$

If we solve the Equation(1.22), we get the conditions for M as given,

$$M = 0 \text{ or } M = \pm\Big[\frac{a_0(T_c - T)}{2b}\Big]^{1/2}. \tag{1.23}$$

The solutions indicate, the second condition is valid only for $T < T_c$ whereas the first condition applies for $T < Tc$ and $T > T_c$. For the $T < T_c$ case, the first condition produces only an unstable equilibrium. Thus, magnetization for $T \geq T_c$ is zero and $T < T_c$ is non-zero and proportional to $(T_c - T)^{1/2}$. Figure.(1.8) shows the schematic diagram of the magnetization curve below and above T_c as a function of temperature.

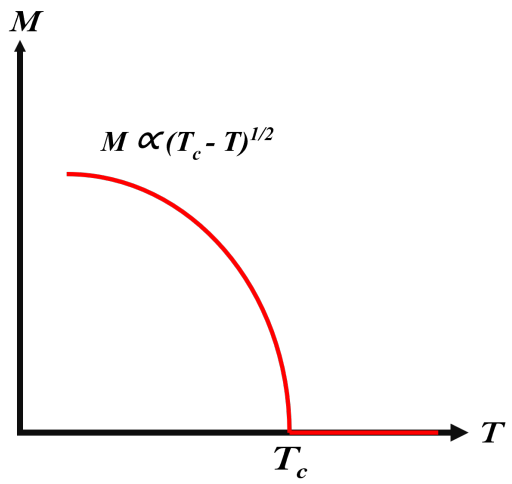

Figure 1.8: Magnetization as a function of temperature [30].

For the case close to transition temperature T_c, Mean field theory fails to describe the behaviour of the phase transition because of the assumption that all regions in the system are the same by ignoring the correlations and fluctuations in the ordering parameter M. Correlations are in general relevant up to a characteristic length scale called correlation length (ξ). When T approaches T_c, ξ becomes infinite at the critical point [30].

In the mean-field theory, the behaviour of the magnetization below the transition is predicated as $(T_c - T)^{1/2}$, however, in real systems, it is observed that the magnetization close to the transition does behaves as $(T_c - T)^{\beta}$, but the exponent is not necessarily close to $\frac{1}{2}$. Therefore the values for the exponents give crucial information about the nature of the phase transition. Similar to the magnetization, it is observed experimentally that there are other physical properties involved to show a power law behaviour with other similar exponents near the transition temperature T_c known as critical exponents. Table.(1.1) shows the physical properties involved in showing critical behaviours and their associated critical exponents.

Table 1.1: Definition of critical exponents [30]

Exponent	Physical property	Expression	
γ	Magnetic Susceptibility (χ)	$\chi \sim (T - Tc)^{-\gamma}$	$T > T_c$
β	Magnetization (M)	$M \sim (T_c - T)^{\beta}$	$T < T_c$
δ	Magnetization (M)	$M \sim H^{1/\delta}$	$T = T_c$
ν	Correlation length (ξ)	$\xi \sim \lvert T - T_c \rvert^{-\nu}$	$T = T_c$

As explained earlier, the mean-field theory ignores the correlations and fluctuations in the

vicinity of phase transitions, therefore, a correct description of the critical region with precise critical exponents cannot be obtained. However, for the systems with a spatial dimensionality (d) higher than a dimensionality called marginal spatial dimensionality (d^*) the mean-field theory gives exact results for the observed critical behaviour. For d less than d^*, the mean-field approaches are quantitatively wrong. For systems with $d = d^*$, there are only logarithmic corrections to the results of mean-field theory. It turns out that the spatial dimensionality to predict the critical exponents correctly to describe the nature of the phase transitions using mean field theory is found to be 4 [34].

The critical behaviour for a classical phase transition is if the marginal dimensionality d^* is greater than 4, then the solutions are identical to that predicted by mean field theory. In the framework of mean-field theory for the classical second-order phase transitions, the exponents of the corresponding physical quantities with reduced temperature $t = \left|\frac{T-T_c}{T_c}\right|$ are:

$$\alpha = 0,\ \beta = 1/2,\ \gamma = 1,\ \delta = 1,\ \nu = 1/2,\ \eta = 0\ [36]. \tag{1.24}$$

The critical exponents for the many physical properties of the systems with dimensionality below four can be calculated by considering a small representative set of an appropriate statistical model disregarding the microscopic details but shared by dissimilar systems as long as the hypothesis of universality is accepted. It is observed that the critical exponents are surprisingly independent of the type of phase transitions, whether the transitions are ferromagnetic-paramagnetic, superconducting-nonsuperconducting, liquid-gas or any other. Therefore, irrespective of the type of phase transitions, the critical exponents for continuous phase transition depend only on the dimensionality of the system (d), the dimensionality or the symmetry of the order parameter (D) and whether the interactions are short or long-range. Hence, to study the critical behaviour of the systems it is only important to look at particular universality classes to select the ideal statistical model in each class for extracting the critical exponents of the physical properties [30, 34].

1.5.1 Using neutron scattering to observe critical exponents

The critical exponents experimentally can be found using the respective measurement techniques of the physical properties to describe the system. In Section (3.2) a rather detailed description of neutron scattering will be provided. It will be explained that M enters the elastic neutron scattering cross section and the imaginary part of the dynamical susceptibility χ"

enters the inelastic neutron scattering cross section (see formulas (3.49) to (3.52)). Therefore, a temperature scan of elastic magnetic neutron scattering allows to determine the critical exponent β of the order parameter. In Section.(1.7) we will see that for overdamped excitations χ" contains the static susceptibility χ_q. Therefore, inelastic neutron scattering at different temperatures allows to obtain the critical exponent γ.

From measurements of χ_q one also can obtain the critical exponent ν of the correlation length. This connection arises [37] because χ_q is the Fourier transform of the correlation function $g(r)$:

$$\chi_q = \sum_r g(r) exp(iq.r). \tag{1.25}$$

Therefore, the half width of the $q = 0$ peak of χ_q is the inverse half width of $g(r)$ which is the correlation length ξ. Therefore, by measuring the neutron scattering cross-section as a function of temperature and wave vector, we can extract the critical exponents of M, χ and ξ as indicated in Figure.(1.9) with t being the reduced temperature $t = \left|\frac{T-T_c}{T_c}\right|$.

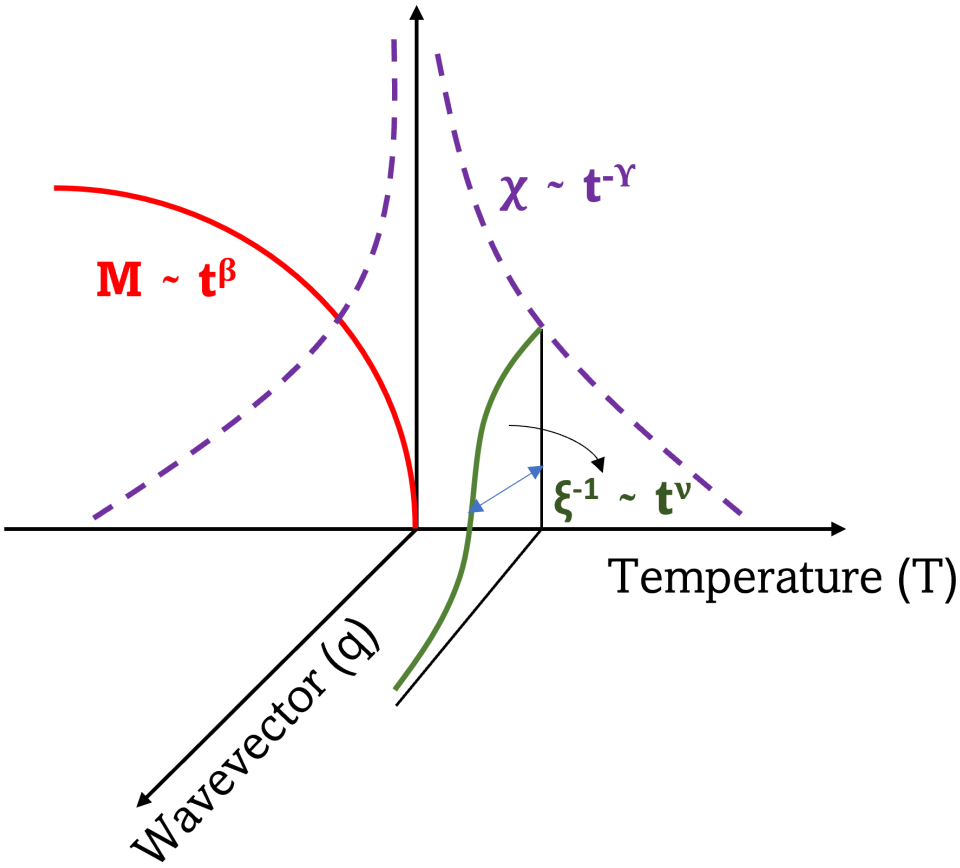

Figure 1.9: Temperature dependence of the physical quantities, wave vector dependent susceptibility, χ_q (violet); magnetization, M (red) determined directly via scattering experiment. The half width of the χ_q along q axis (green curve) is the inverse correlation range [37].

1.6 Quantum phase transitions and criticality

In conventional phase transitions the temperature is the control parameter and the critical point can be traversed upon varying the temperature. By contrast, the phase transition which occurs at absolute zero temperature is called the quantum phase transitions (QPT) where the quantum mechanical effects of the system at this temperature are more dominant and leads to the quantum fluctuations demanded by Heisenberg's uncertainty principle. The quantum phase transitions can be achieved by using non-thermal control parameters such as pressure, composition, electric field or magnetic field. The point at which the second-order phase tran-

sition takes place at absolute zero temperature is called a quantum critical point (QCP). The generic phase diagram of the second-order quantum phase transition is shown in Figure(1.10)

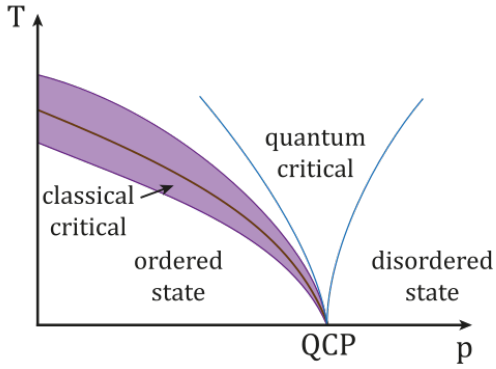

Figure 1.10: The generic phase diagram of the tuned second order quantum phase transition. The picture is from [38]

The second-order quantum phase transition can be approached generally in two ways using non-thermal control parameters r, $r \to r_c$ at $T = 0$ or $T \to 0$ at $r = r_c$. The critical exponents at the vicinity of phase transition can be now expressed using the reduced control parameters $t = \left|\frac{r-r_c}{r_c}\right|$. It is predicted that the quantum phase transition in dimension d is related to a classical phase transition in space dimension $(d + z)$ where $z = 1$ for most transitions, and hence it is concluded that the critical behaviours are similar. Therefore, since the mean-field approximation is independent of the system's dimensionality, the critical exponents of the physical quantities in the mean-field approaches tend to show the same values at both classical and quantum critical points (see Equation.(1.24) for exponent values), however, the critical amplitudes are different [34, 36, 37].

While the mean-field approximation predicts the same exponents for both classical and quantum phase transitions, and a qualitative behaviour near critical temperature, the experimental values obtained for magnetic systems were found to differ from the theoretical values due to the mean field assumption of neglecting the fluctuations in the vicinity of the critical point [34]. It is obvious that nearing the critical point huge fluctuations play a role in determining the phase change of the system. In the next section, we present a theory that considers the spin fluctuation in the magnetic metals that can be used to extract the critical exponents by measuring the neutron scattering cross section which gives directly the dynamical susceptibility.

1.7 Spin fluctuation theory

The low-energy excitation spectra near a magnetic QCP can be described by the spin fluctuation theory [39].

The aim of the spin fluctuation theory presented here is to obtain a plausible dynamical equation for the non-local magnetic susceptibility as a model of the interaction field between the spins of the electrons. The main assumption of the model is that the moments of the electron (μ) is coupled to an exchange field by a potential $-\mu \cdot h_m$, where $h_m = \lambda m$ is the exchange field and λ is a phenomenological exchange field parameter. The model is developed by considering a homogeneous cubic lattice system that is isotropic and without any symmetry-breaking transitions.

The model uses the space and time dependence of the average magnetization $M(r,t)$ in the presence of external magnetic field $H_{ext}(r,t)$.

To find the scalar dynamical field, we start with the case of static scalar magnetic field ($H_{ext}(r,t) = H$) which stabilises a uniform and static magnetization M given by some relation, $H = H(M)$. Since the system is isotropic, then the function M must be odd therefore the static field H can be expressed as Taylor expansion of the order parameter M

$$H = a_0 M + b_0 M^3 \tag{1.26}$$

where a_0 is the inverse of the Pauli susceptibility and b_0 is the anharmonicity parameter. Equation.(1.26) gives the magnetization induced just by the externally applied field without any consideration for the feedback from the exchange field λM. If we now include the exchange field in the Equation.(1.26) it becomes

$$H = aM + bM^3 \tag{1.27}$$

where $a = a_0 - \lambda$ is the inverse of the enhanced susceptibility χ if $a > 0$ and b is b_0 if the exchange field is linear in M. Since the case that we have considered is non-linear, we can assume $b = 0$. With this initial condition for the case of spatially varying but still static field H which stabilises the M, H can be expressed as given by Ginzburg-Landau equation,

$$H = H[M] = aM - c\nabla^2 M \tag{1.28}$$

where $M = M(r)$ is a space dependent magnetization and H[M] now represents the functional of M and c is a new parameter that measure the resistance of the system against the spatial modulation of M.

Therefore the effective field that represents the deviation of the system from its equilibrium can be written as,

$$H_{eff} = H - H[M] \tag{1.29}$$

where H is the applied field and H[M] is equal to Equation.(1.28), and becomes zero when the system is in equilibrium.

The time evolution of the magnetization is introduced to the model through a linear restoring term where H_{eff} small :

$$\dot{M} = \gamma \star H_{eff} \tag{1.30}$$

where $\dot{M}$ indicates the time derivative of M, γ a relaxation function, $\star$ represents the spatial convolution.

A Fourier transform of this model [39] leads to the dynamical susceptibility $\chi(q, E)$ as defined in the following set of equations:

$$H(q, \omega) = \chi^{-1}(q, \omega) M(q, \omega) \tag{1.31}$$

where,

$$\chi^{-1}(q, \omega) = \chi_q^{-1}\big(1 - i\frac{\omega}{\Gamma_q}\big) \tag{1.32}$$

$$\chi^{-1}(q) = \chi^{-1} + cq^2 \tag{1.33}$$

$$\Gamma_q = \gamma_q \chi_q^{-1} \tag{1.34}$$

where $\chi^{-1}(q,\omega)$ is the general susceptibility, $\chi^{-1}(q)$ is the susceptibility at $\omega = 0$ and χ is the susceptibility at both q and ω is zero and γ_q is the relaxation function. If there is no dependency between exchange field and the $\dot{M}$, then the relaxation function is given by

$$\gamma_q = \gamma q^n \tag{1.35}$$

where γ is a constant and n=1 for small q values.

If we consider the system is a homogeneous, non-interacting Fermi system, the movement of the electrons in the system is free and ballistic. If we consider the mean free path of the electron in the ballistic trajectory is of the order of magnetic ordering wavelength λ_e we will get,

$$\gamma_q \propto \tau^{-1}, \tag{1.36}$$

where τ is the time taken for the electron to cover the magnetic wavelength $\lambda = 2\pi/q$ obtained with the help of the Fermi velocity and given by

$$\tau = \frac{2\pi}{v_F q}, \tag{1.37}$$

therefore we get

$$\gamma_q \propto \frac{v_F q}{2\pi} \tag{1.38}$$

and

$$\Gamma \propto q \text{ (n = 1)} \tag{1.39}$$

away from the QCP. The Equation.(1.39) represents the *Landau damping* in the case of ferro and paramagnetic systems. This linear behaviour of the Fermi liquid breaks down however when critical point is approached where the fluctuation associated with that tend to freeze. At the critical point, the wavelength of the magnetic excitations become much bigger than the mean free path of the electron and slow down and $\Gamma_q \propto q^2$ (n=2).

If we consider next the generalised susceptibility of the excitations that represent the energy dependent response of each magnetic mode, it can be written as

$$\chi_{q,\omega} = \left[\chi^{-1}\left(1 - i\frac{\omega}{\Gamma_q}\right)^{-1}\right] \tag{1.40}$$

$$= \frac{\Gamma_q \chi_q}{\Gamma_q - i\omega} \tag{1.41}$$

$$= \frac{\Gamma_q^2 \chi_q}{\Gamma_q^2 + \omega^2} + i\frac{\Gamma_q \chi_q \omega}{{\Gamma_q}^2 + \omega^2} \tag{1.42}$$

From Equation.(1.42) we can recognise that the imaginary part that is measured in neutron scattering has the form of an overdamped harmonic oscillator model [40]. Thus, near the ferromagnetic quantum critical point in the paramagnetic phase we expect this behaviour. The critical exponent predicted by the spin fluctuation theory at the FM−QCP (3D FM) for the magnetic susceptibility and correlation length are $\chi_q \propto T^{-4/3}$ [39, 40] and $\xi \propto T^{-2/3}$ [41] respectively.

2

Overview of the $Nb_{1-y}Fe_{2+y}$ system

The $Nb_{1-y}Fe_{2+y}$ system, a transition metal itinerant d-electron ferromagnet with complex C14 Lave phase crystal structure [27], displays a rich magnetic phase diagram over a small doping range. The system with a scenario of masked Ferromagnetic Quantum Critical Point (FM-QCP) by the emergence of modulated magnetic order makes it an ideal case for studying theoretically predicted FM-QCP in clean itinerant intermetallic compounds. This chapter presents an overview of the properties of the $Nb_{1-y}Fe_{2+y}$ system investigated previously from various studies and measurements.

2.1 Structural properties

The stoichiometric $NbFe_2$ system crystallizes in a hexagonal C14 lave phase ($MgZn_2$ hexagonal structure) structure with space group $P6_3/mmc$ [27] displayed in Figure.(2.1a).

The unit cell of the structure consists of 4 formula units (see Figure.(2.1a)) with lattice parameters of a=b= 4.8401(2) $\AA$ and c=7.8963(6) $\AA$ [27], in crystallographic terms, $NbFe_2$ $\equiv$ $Nb_4Fe_2^{(2a)}Fe_6^{(6h)}$. The Fe atoms in the crystal form layers of kagome network at $6h$ sites perpendicular to c axis of the crystal which are separated by Fe atoms at $2a$ sites centred on the line between alternative kagome triangles [42]. The Nb atoms occupy the interstices of this Fe structures at $4f$ site, slightly out of plane with respect to Fe atom at $2a$ sites (see Figure.(2.1b)). The WyKoff positions for the Nb, $Fe^{(2a)}$ and $Fe^{(6h)}$ atoms without inversion are $4f(1/3, 2/3, x)$, $2a(0, 0, 0)$ and $6h(y, 2y, 3/4)$, respectively. From the extended view of the crystal structure shown in Figure.(2.1b) we can see that the $Fe^{(2a)}$ atoms only coordinated with every second upper (red) and lower (green) kagome triangles formed by $Fe^{(6h)}$ atoms, therefore, the bonding between the $Fe^{(2a)}$ and $Fe^{(6h)}$ atoms in the pairs are not be the same [42]. The

interatomic bond distances calculated by Tompsett *et al.,* is given in Table.(2.1). In the table, we can observe that the interatomic distances among Fe sites (from $Fe^{(2a)}$ and $Fe^{(6h)}$ sites) are similar. Therefore, the dopant site preferred is likely to be determined by the bonding network of the Fe-cage formed by the $Fe^{(2a)}$ and $Fe^{(6h)}$ atoms upon Nb doping rather than the volume availability at the site [42].

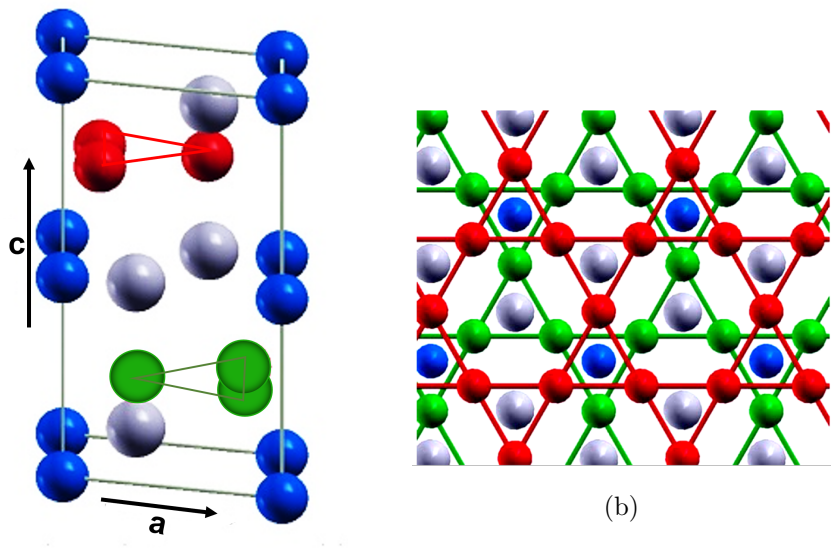

(a) (b)

Figure 2.1: The crystal structure of the $NbFe_2$ system. (a) Laves unit cell. The atoms in the colors blue, red and green, and gray represented are $Fe^{(2a)}$, $Fe^{(6h)}$ and Nb respectively. The red and green triangles indicate the upper and lower kagome layers formed by $Fe^{(6h)}$ atoms. (b) The view of the extended crystal structure along the principle axis c of the hexagonal structure. The upper and lower kagome layers ($Fe^{(6h)}$) shown respectively in red and green coordinated with $Fe^{(2a)}$ atoms and Nb atoms. The images are from Ref. [42].

Table 2.1: The shortest interatomic bond distance between two given sites for the stoichiometric $NbFe_2$ system obtained by Tompsett et al., [42].

Sites	Distance $\AA$
$Fe^{(2a)}$-$Fe^{(6h)}$	2.42
$Fe^{(6h)}$-$Fe^{(6h)}$	2.37
$Fe^{(2a)}$-$Fe^{(2a)}$	3.95
Nb-$Fe^{(2a)}$	2.84
Nb-$Fe^{(6h)}$	2.81
Nb-Nb	2.89

From the analysis of Density Functional Theory (DFT) calculations using Generalized-Gradient Approximation (GGA)-Perdew-Burke-Ernzerhof (PBE) exchange correlation function in the framework of stoner theory, it was shown that the bonding structure of the Fe cages produces inequivalent character in the kagome triangles at $Fe^{(6h)}$ layers which is instrumental in producing complex evolution of the temperature-compositions magnetic phase diagram upon doping [42].

2.2 Electronic and magnetic properties

To understand the electronic and magnetic properties of the $NbFe_2$ system the electronic structure and density of sates (DOS) calculations have been made by several groups [42–47]. The general features of all of their calculations qualitatively agree that the electronic properties are governed by partially filled $3d$ and $4d$ band crossing of Fe and Nb atoms respectively at the Fermi surface [47]. The DFT calculations using Generalized-Gradient Approximation (GGA)-Perdew-Burke-Ernzerhof (PBE) exchange correlation function in the framework of stoner theory have shown that the structure of the partial density of states calculated for $Fe^{(6h)}$ d and $Fe^{(2a)}$ d states are found to be similar and dominating at the Fermi level, in contrast, the d orbitals of the Nb atoms contributes far less to the over all structure of the DOS [42, 46]. The dominant contribution of the Fe d states of the Fe cage bonding structure to the DOS at the Fermi level found to be crucial to the evolution of the magnetic phase diagram upon doping [42].

The previous theoretical calculations to study the magnetic ground state of the stoichio-

metric $NbFe_2$ have yielded contrasting results, where it was thought to be a paramagnet [43] or antiferromagnet [45]. However, those studies also found that the antiferromagnetic state to be energetically close to two other types of ferromagnetic states [47]. The electronic structure calculations performed by Subedi *et al.* within the local spin-density approximation (LSDA) using the general potential linearized augmented plane-wave (LAPW) method has shown that the moments are highly dependent on ordering, therefore, the nature of the magnetism is itinerant [47]. Figure.(2.2) shows the various spin configurations calculated for finding energetically favourable magnetic ground state of the $NbFe_2$ using LSDA by Subedi *et al.* The calculations are made by considering only the collinear magnetic ordering cases. The cartoons in the Figure.(2.2) depict only the spins of the Fe atoms as it was observed that the induced moments of the Nb atoms are small compared to the moments of the Fe atoms.

The ground state energy per unit cell illustrated in the Figure.(2.2) is shown relative to the non spin polarised case (Figure.(2.2a)). Among various magnetic ordering pattern it was observed that the ferrimagntic ordering (Figure.(2.2c)) has the lowest energy with largest moment on $Fe^{(2a)}$ site and it is believed to represent the ground state of the stoichiometric $NbFe_2$, however, the antiferromagnetic ordering (Figure.(2.2d)) is also almost degenerate with ferrimagntic ordering suggesting competing magnetic interactions in the system [47]. The other cartoons of the spin configurations (Figure.(2.2b,2.2e, 2.2f) suggest that they are energetically unfavourable when compared to the energy of the non spin polarised case (Figure.(2.2a)) [47].

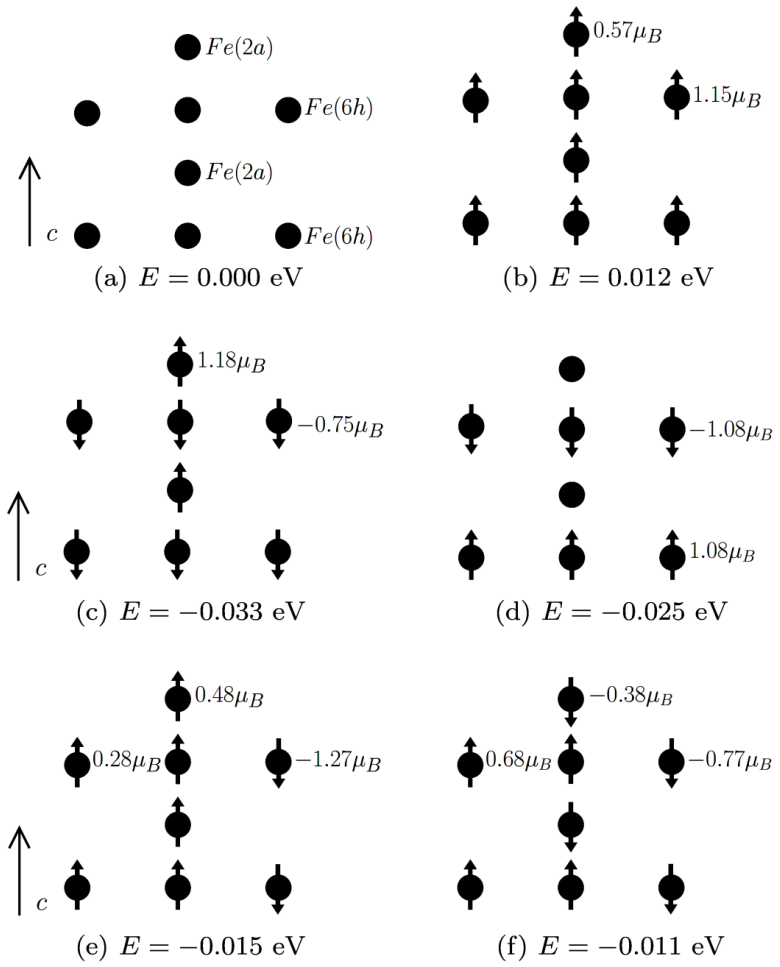

Figure 2.2: The potential magnetic ordering configurations of Fe atoms in the $NbFe_2$ system along the crystal axis c. The arrows on the Fe atoms indicate the induced moments. (a) Non spin polarised case. (b-f) Various potential configurations of spins. The spin configuration (c) is believed to represent the ground state of the $NbFe_2$ system obtained from the solution of the first principle calculations [47].

The earlier investigations on the $Nb_{1-y}Fe_{2+y}$ system have shown to reveal a rich magnetic phase diagram across a narrow doping range of compositions. The evolution of the magnetic ground states with doping for the $Nb_{1-y}Fe_{2+y}$ system were established using Nuclear Magnetic Resonance (NMR) and magnetisation measurements. The phase diagrams have shown that with doped excess Fe or Nb atoms found to exhibit ferromagnetic ordering [48]. Although the recent LSDA calculations to find the magnetic ground state of the stoichiometric $NbFe_2$ point towards the ferrimagnetic ordering and also a possible degenerate antiferromagnetic state [47] as discussed previously, the earlier investigation was found to be a weak antiferromagnet with Neel temperature (T_N) $\approx$ 10 K [48]. The antiferromagnetic ordering of the stoichiometric

$NbFe_2$ was confirmed from the Nb NMR measurements using a spin echo method by Yamada *et al.* below $T_N \approx 10$ K. Figure.(2.3) shows NMR spectra measured at temperature T = 4.2 K with two fixed frequencies of 3 and 10 MHz on the series of $Nb_{1-y}Fe_{2+y}$ samples. The figure shows that the features of the NMR spin echo intensity with field for the composition y $\leq$ -0.004 are similar for both the frequencies where as for the compositions y > -0.004, the line shape is quite different and the line width is broad for both frequencies measured. The NMR spectra at 3 MHZ for composition $y = +0.002$ shows an additional peak in the higher field side in addition to the peak at the position of zero knight shift which indicates the appearance of ferromagnetic clusters in the antiferromagnetic matrix which would be formed with an excess Fe atom occupying at the Nb site [48].

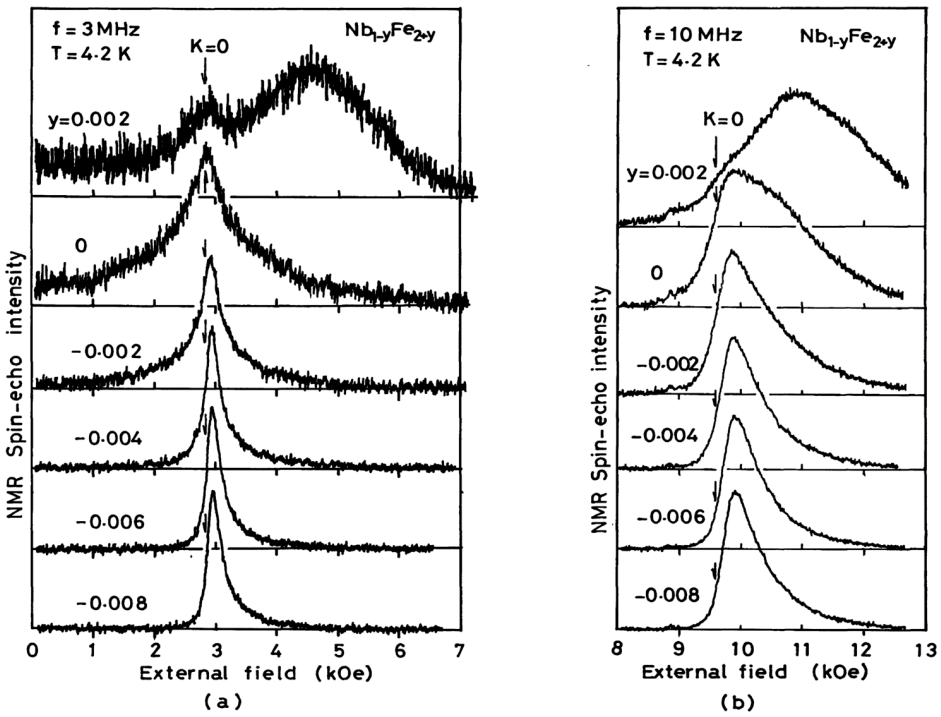

Figure 2.3: $^{9}3$Nb NMR spin echo spectra measured on a series of $Nb_{1-y}Fe_{2+y}$ with magnetic field by Yamada *et al.* at frequencies : (a) 3 MHz and (b) 10 MHz. The pictures are taken in Ref. [48]. The field of zero Knight shifts ($K = 0$) are indicated by arrows.

The past experiments to confirm the magnetic phases of the $Nb_{1-y}Fe_{2+y}$ system explored in the polycrystals by NMR and magnetic measurements while agreeing broadly the established composition-temperature phase diagrams but they differ in their classifications of the slightly

Nb rich regions of the phase diagram. The NMR studies by Yamada *et al.*, describes the region around y ≈ -0.01, down to 2K as paramagnetic [48] where as the DC magnetisation measurements using vibrating sample magnetometer by Crook *et al.* suggests the composition exhibit a mixed phases of ferromagnetic and antiferromagnetic [49]. The composition temperature phase diagram obtained by Yamada *et al.* and Crook *et al.* are shown in Figure.(2.4a) and Figure.(2.4b) respectively.

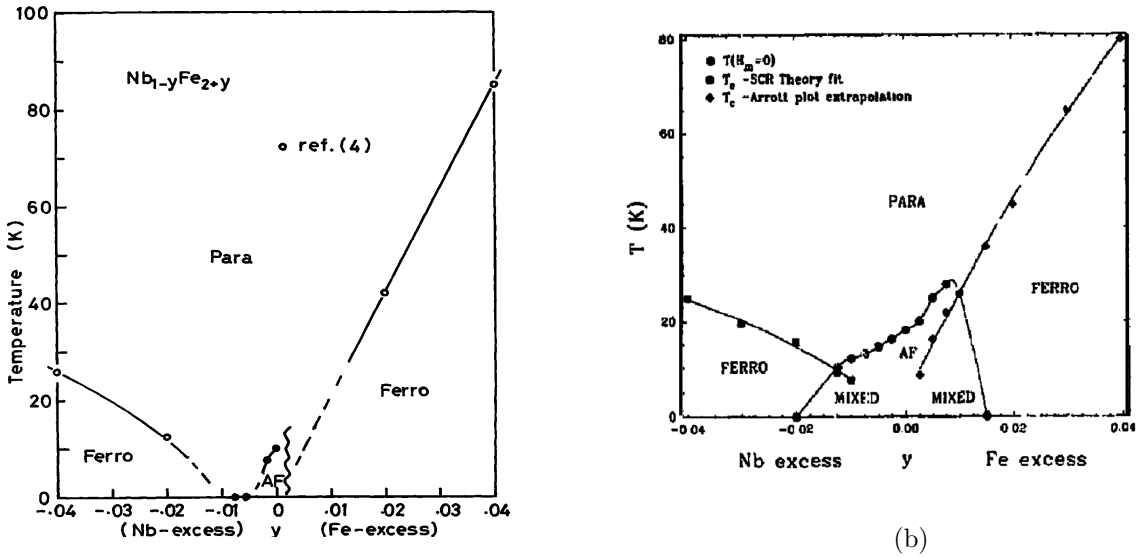

(a) (b)

Figure 2.4: The expected composition-temperature phase diagram of $Nb_{1-y}Fe_{2+y}$ system obtained from the experiments of NMR and magnetisation. (a) Established from the NMR works by Yamada *et al.* [48] and Shiga *et al.* [50]. The picture is taken from Ref. [48]. (b) The phase diagram established using the DC magnetisation measurements by Crook *et al.*, [49]. The picture is from Ref. [49].

To confirm the true magnetic phase of the $Nb_{1-y}Fe_{2+y}$ system at around $y \approx -0.01$ region and to re-examine the magnetic phase diagram of the system, recently, a systematic study of magnetism were carried out on a freshly prepared high quality samples by Moroni-Klementowicz *et al.* The Arrot plots obtained for various compositions y from their work provide an additional evidences for the respective magnetic phases observed for the similar compositions previously by Yamada *et al.* shown in Figure.(2.5). The plots show for different range of temperatures the curves appear differently above and below of the bulk antiferromagnetic transition temperature, T_N, (where the curve almost linear shown in the figure red) for the composition with a bend towards left and right, respectively. The extrapolated value of M^2 to $H/M = 0$ for the

samples $y = -0.012, -0.006$ and 0 all show negative indicating no spontaneous magnetization. For sample $y = +0.007$ the extrapolated value of M^2 to $H/M = 0$ show positive for the temperatures below 10 K indicating the existence of spontaneous magnetization. The curves for the sample $y = -0.012$ display no sign of any change to the appearance in the temperature range measured suggests the compound is paramagnet within that range [27]. Based on the earlier results and the recent neutron scattering measurements it was found that the type of the antiferromagnetic phase of the samples in the range between $-0.008 \leq y < +0.02$ is a spin density wave (SDW) ordering with an helical arrangement of the Fe spins [27, 28, 48, 49].

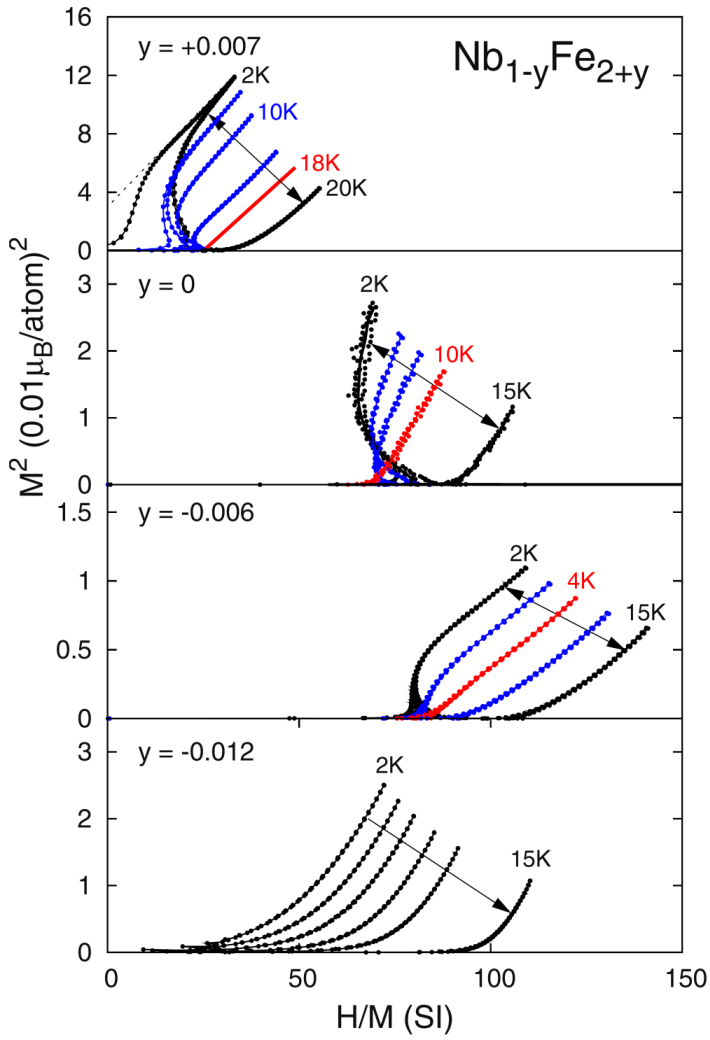

Figure 2.5: Arrot plots for $Nb_{1-y}Fe_{2+y}$ samples range from slightly Fe rich to slightly Nb rich compositions measured at different temperatures by Moroni-Klementowicz et al. The red curves indicate the Neel temperature (T_N) measurements at which the change of slope happens to the lines of extrapolation of the M^2 vs H/M linear dependence. The curves $T < T_N$ and $T > T_N$ indicate the curves with bend towards right and left respectively. The picture is taken from Ref. [27].

The zero field AC magnetic susceptibility measurements with temperature performed by Friedemann *et al.* quite recently for the selected compositions of Fe rich, Nb rich compounds and stoichiometric $NbFe_2$ provide further evidence for the different magnetic phases observed in the series of $Nb_{1-y}Fe_{2+y}$ samples. Figure.(2.6) shows the anomalies in the temperature -dependent AC magnetic susceptibility ($\chi'(T)$) as a signatures of both FM and SDW phase transitions.

For the Fe-rich sample ($y = 0.015$) the signatures of FM and SDW phase transitions are seen at $T_C \approx 24$ K and $T_N \approx 32$ K, respectively [51]. It can be seen that for the Fe-rich sample the anomaly observed at T_C during warming and cooling measurements a clear hysteresis, indicating the transition SDW-FM is first order which is also confirmed from the resistivity measurements [51]. The transition PM-SDW on lowering the temperature of the system is found to be second order where only a much weaker anomaly was observed in the derivative of the resistivity ($d\rho/dT$) [51]. The Nb rich and stoichiometric $NbFe_2$ samples display only a single transitions at $T_N \approx 3$ K and $T_N \approx 12$ K respectively with the characteristics of SDW order.

The phase boundaries for different magnetic phases with doping concentration y were identified carefully from the thermal, transport and magnetization measurements by Moroni-Klementowicz *et al.* The refined version of the composition-temperature magnetic phase diagram of $Nb_{1-y}Fe_{2+y}$ series of samples obtained is shown in Figure.(2.7).

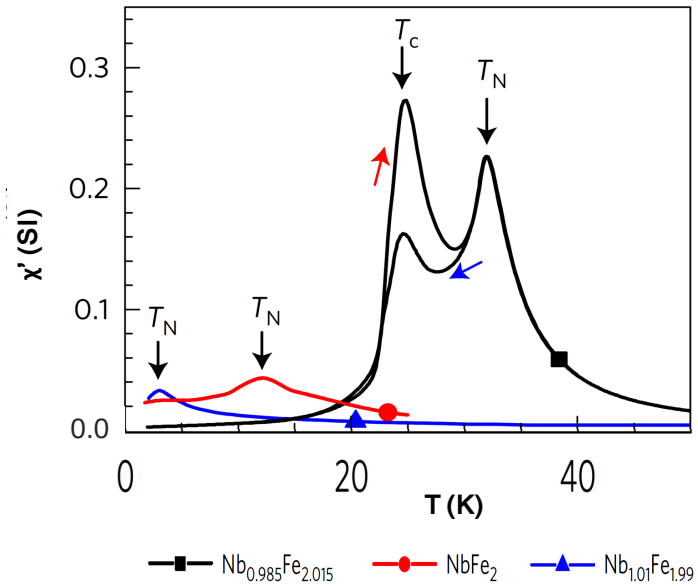

Figure 2.6: The temperature dependence of the AC magnetic susceptibility $\chi'(T)$ measured for the Fe rich, stoichiometric and Nb rich samples of the $Nb_{1-y}Fe_{2+y}$ system. The red and blue arrow indicates the measurements performed in the warming and cooling respectively. The picture is taken from Ref. [51].

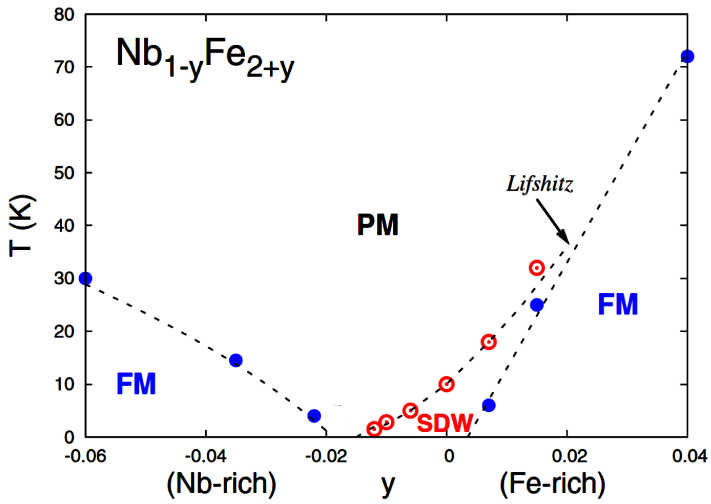

Figure 2.7: The refined composition - temperature phase diagram of $Nb_{1-y}Fe_{2+y}$ system established using the transport and thermodynamic measurements by Moroni-Klementowicz et.al., [27]. The blue solid spheres indicate the Curie temperature (T_C) and the red circles are Neel temperature (T_N). The picture is taken from Ref. [27].

The composition-temperature phase diagram measured in zero field with doping Fe and Nb

atoms exhibit different magnetic phases such as ferromagnetic (FM), SDW and paramagnetic (PM) (see Figure.(2.7)). For the doping concentrations $y > -0.02$ (Nb rich side of the phase diagram) the samples show only the FM phase where as for the Fe rich side of the phase diagram ($y \geq +0.007$) both SDW and FM phases are observed with transition from PM-SDW and SDW-FM on lowering the temperature. In the phase diagram for the composition y $\approx +0.02$ show a Lifshitz point and above that the compounds show only PM-FM phase transition. Near the stoichiometric composition range ($-0.008 < y < 0.007$) the samples show only the SDW phase below T_N. For the composition range $-0.02 < y < -0.008$, the compounds exhibit only paramagnetic phase. From the $M - H$ isotherm measurements for the excess Fe and Nb rich samples, it was found that the observed ferromagnetic phases are different in nature [27].

The characteristics of SDW and the FM phases are further investigated in the recent experiments of neutron scattering [28] and spin-dependent compton scattering [52], respectively. The outcome of the neutron diffraction measurements confirms that the existence of antiferromagnetic order in the stoichiometric $NbFe_2$ system is indeed a long-wavelength modulated magnetic (SDW) order observed on the boarder of ferromagnetic order at the low temperatures with small ordered moment $\mu_s < 0.1\ \mu_B$. The evolution of the SDW order with temperature and composition measured with neutron diffraction by Niklowitz *et al.* observed that the ordering wave vector of the SDW state is found to be $q_{SDW} = (0\ 0\ \ell_{SDW})$ which was confirmed in all the measured samples [28]. From the distribution of allowed and forbidden satellite Bragg peaks of the SDW order the magnetic structure was found to be linearly polarized with moment orientation along the c axis rather than the spiral order. From the AC susceptibility and torque magnetometry measurements it was determined that the c axis to be the magnetic easy axis of the system independent of the chemical composition [28, 53]. Figure.(2.8) shows the allowed and forbidden Bragg peaks of the SDW state in the (h 0 ℓ) plane of the reciprocal lattice [28].

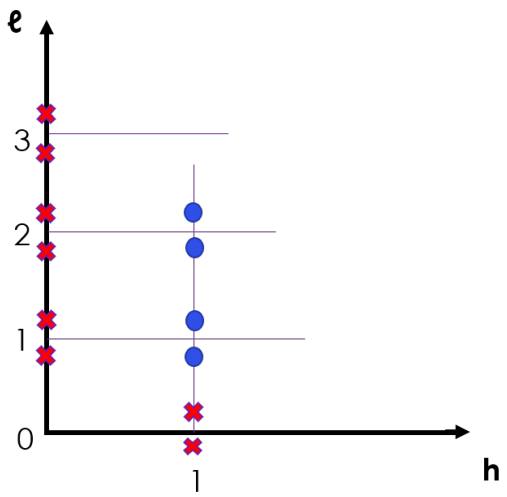

Figure 2.8: The Bragg's reflections observed for the SDW order in the (h 0 ℓ) *r.l.u.* reciprocal lattice plane. The blue dots represents the SDW peak observed and the dark pink cross represents where the peaks are forbidden

The temperature dependence of the neutron diffraction results for the Fe-rich side of the $NbFe_2$ phase diagram is shown in Figure.(2.9). The magnetic neutron scattering measured for the FM order at the weak nuclear Bragg position (1 0 2) *r.l.u.* is shown in Figure.(2.9a). The FM intensities of the samples measured are normalised by the intensities at T_C and the FM ordered moments obtained from the FM intensities are discussed in Ref. [28]. The figure shows the FM order can be observed for the Fe rich samples $y = +0.015$ and $y = +0.020$ respectively below $T_C \approx 24.5$ K and $T_C \approx 34$ K. For slightly Fe-rich sample, $y = +0.003$, no FM ordering has been observed even the temperature below 5 K [28].

Figure.(2.9b) shows the temperature dependence of the SDW ordered moment μ_s for the Fe-rich samples obtained from the integrated intensities of SDW peak temperature evolution measured at Q = (1 0 1+ℓ_{SDW}) *r.l.u.* as described in Ref. [28]. It can be seen that the ordered moment of the SDW peak rise continuously with temperature below T_N for all three samples, suggesting the PM-SDW transition is second-order. For samples Fe-rich ($y = +0.015$ and $+0.02$) the peak of the SDW ordered moment coincides with onset Curie temperature T_C and there is a temperature range below T_C both orders SDW and FM appear to coexist. This coexistence was attributed to a distribution of transition temperature within the sample [28]. Figure.(2.9c) shows the temperature dependence of the SDW ordering wave vector q_{SDW} = (0 0 ℓ_{SDW}). It was observed that the ℓ_{SDW} shows a significant dependence on temperature and composition. At the transition of SDW-FM order the ℓ_{SDW}(T) stays finite so there is

a discontinuous change in the magnitude of the wave vectors from finite q_{SDW} to zero q_{FM}. Also, from the figure we can see that for warming and cooling measurements of ℓ_{SDW} displays a significant thermal hysteresis. These observations suggest that the SDW-FM is a first order transition [28].

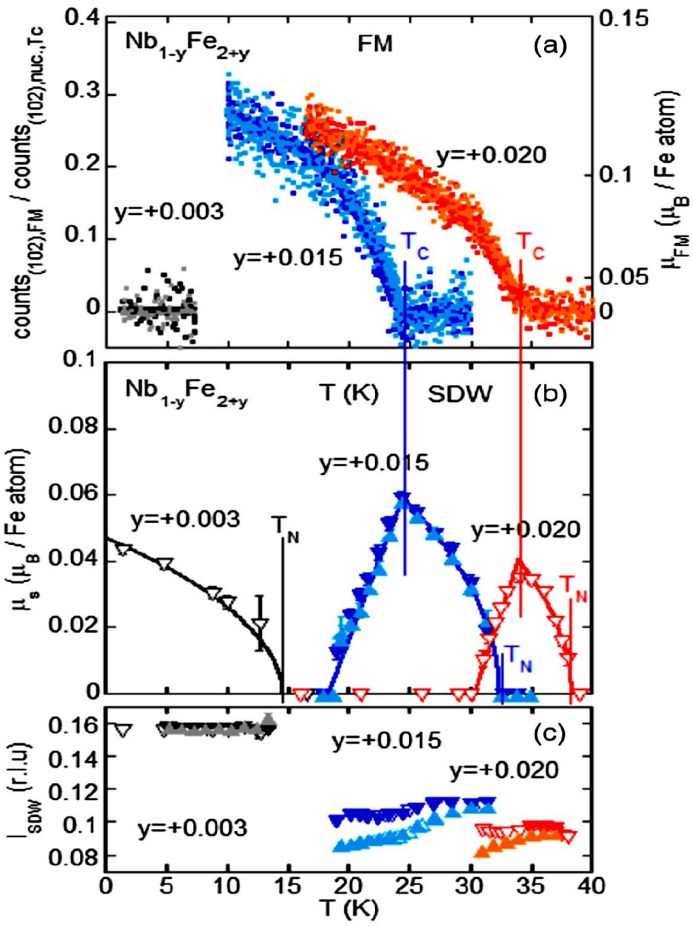

Figure 2.9: The temperature dependence of the neutron diffraction results obtained for $Nb_{1-y}Fe_{2+y}$ by Niklowitz *et al.* (a) Normalised FM intensities measured at the weak nuclear Bragg position (1 0 2) *r.l.u.* and FM ordered moments μ_{FM}. (b) SDW ordered moment, μ_s. (c) SDW ordering wave vector values of q_{SDW}. The markers downward triangles and upward triangles indicate the measurement sequences going down and up, respectively. The samples measured are $y = +0.003$ (black, gray), $y = +0.015$ (dark blue, light blue) and $y = +0.02$ (red, orange). The each samples are measured in different experiment beam times indicated by empty and filled markers. The lines are guide to the eye. The picture is taken from Ref. [28].

The FM phase was investigated by Haynes *et al.* for the Fe-rich sample ($y = +0.015$) to resolve for the true magnetic ground state adopted by the $Nb_{1-y}Fe_{2+y}$ system. From their work it was demonstrated that the magnetic structure of the Fe-rich samples are Ferrimagnetic using spin-dependent Compton scattering in conjunction with ab initio electronic structure calculations [52]. Earlier the magnetic ground state of the stoichiometric NbF_2 was also theoretically predicted to be a ferrimagnetic ordering, also a possible competing degenerate AFM ordering by Subedi *et al.* discussed previously (see Figure.(2.2)). The results of Haynes *et al.* shows the magnetic structure is ferrimagnetic in which the two inequivalent Fe sites order antiparrallel to one another as observed similarly by Subedi *et al.* but slightly with different magnitudes [52].

2.3 Non fermi liquid behaviour of $Nb_{1-y}Fe_{2+y}$ system

From the previous section we saw that the Lave phase $Nb_{1-y}Fe_{2+y}$ system exhibit a variety of magnetic phases within a narrow doping range such as FM and long-wavelength SDW orders in zero magnetic field and at ambient pressure (see Figure.(2.7)). The stoichiometric $NbFe_2$ sample shows a SDW order below $T_N \approx 10$ K, on the other hand the sample with composition $y = -0.012$ shows paramagnetic ordering. It was found that on reducing the Fe content (for small negative y), the SDW state can be suppressed completely and leading to the magnetic quantum critical point (QCP), by extrapolation the possible doping concentration to approach the QCP was found to be around $y \approx -0.015$ by Moroni-Klementowicz *et al.* [27]. The earlier measurements of resistivity and specific heat capacity on temperature around the vicinity of the QCP in slightly Nb rich single crystal $y = -0.01$, performed by Brando *et al.* have observed that close to QCP both the resistivity and the heat capacity exhibit anomalous temperature dependences consistent with logarithmic Fermi-liquid breakdown [54]. Therefore, the system $Nb_{1-y}Fe_{2+y}$ provides a rare opportunity to realize the FM-QCP in the d metal system.

Figure.(2.10) shows the resistivity versus temperature measured for the nearly critical single crystal ($y = -0.01$). It was observed that the resistivity $\rho(T)$ follows the $T^{3/2}$ power law down to T < 0.1 K indicating unconventional Fermi-liquid behaviour. The $\rho(T)$ behaviour was also observed qualitatively in a number of other samples of similar compositions by Brando *et al.*, however, the values of the exponent varies between 3/2 and 5/3 suggest the precise form of the $\rho(T)$ may depend on the sample orientation and stoichiometry [54]. The measurements of the Sommerfield coefficient versus temperature, measured by Brando *et al.* is shown in Figure. (2.11). The figure shows that the Sommerfield coefficient displays a distinct logarithmic T

dependence where it gets increased to high values on cooling to 0.1 K than the already increased value of the electronic contribution to C/T observed at 4 K [54].

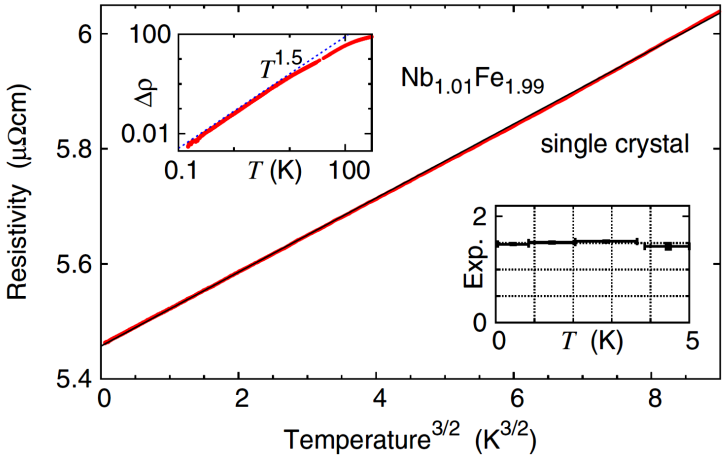

Figure 2.10: The temperature dependence of the resistivity measured for the single crystal $Nb_{1.01}Fe_{1.99}$. The insets, upper: power law for wide range of temperature and bottom: precision of exponent estimate. The red lines indicate the linear fit function. The picture is taken from Ref. [54].

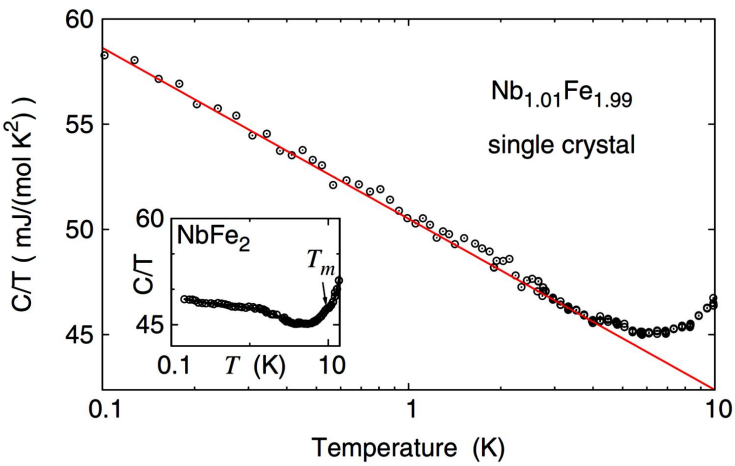

Figure 2.11: The temperature dependence of the Sommerfeld coefficient measured for the single crystal $Nb_{1.01}Fe_{1.99}$. The red line indicate the linear fit function. The picture is taken from Ref. [54].

The observed anomalous temperature dependences of the resistivity and the heat capacity of nearly critical single crystal indicates that the $Nb_{1-y}Fe_{2+y}$ system is a clear example of a

logarithmic breakdown of the Fermi liquid state, however, it cannot be decided unambiguously that whether observed low temperature behaviour is because of the FM or SDW spin fluctuations, though the C/T behaviour is consistent with the predictions for a 3D FM-QCP, the nature of the fluctuations still requires clarification [54]. Therefore, the $Nb_{1-y}Fe_{2+y}$ system provide a unique opportunity for various studies of band magnet quantum criticality at ambient pressure. The location of the expected quantum critical point (QCP) masked by the emergence of the SDW order in the zero field composition-temperature phase diagram is shown in Figure.(2.12).

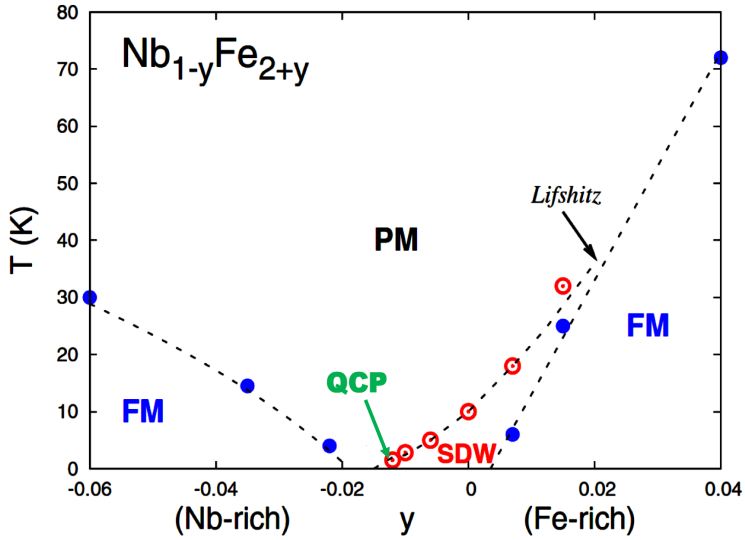

Figure 2.12: The refined composition - temperature phase diagram of $Nb_{1-y}Fe_{2+y}$ system established using the transport and thermodynamic measurements by Moroni-Klementowicz *et.al.*, [27]. The blue solid spheres indicate the Curie temperature (T_C) and the red circles are Neel temperature (T_N). The picture is taken from Ref. [27].

3

Experimental Techniques

From the review of the properties of $Nb_{1-y}Fe_{2+y}$ system we explored the unconventional Fermi-liquid behaviour, suggesting the possible existence of the ferromagnetic (FM) quantum critical point (QCP) covered up by the emergent spin density wave (SDW) order. We use this unique opportunity provided by the system to investigate the band magnet quantum criticality at ambient pressure. Since significant studies have been done previously on the system by tuning composition [55], our aim is to investigate the system using other non thermal tuning parameter, for example magnetic field to establish the temperature-magnetic field phase diagram on a specific compositions and to study the associated various special points in the phase diagram (e.g, Tricritical points (TCPs), FM-QCPs *etc.*)

We present in this chapter a detailed description of the experimental methods, instruments and the sample with specific compositions used for investigating the magnetic phase diagram and excitations at different magnetic fields and temperatures. The instruments and the principle that we used through out our studies for this purpose are neutron based. The outline of the chapter is as follows, first we introduce the samples used for the experiments, second we will look at the theory of unpolarised neutron scattering. Eventually the overview of the instruments used.

3.1 Single crystal growth of Fe-rich $NbFe_2$

The single crystals $Nb_{1-y}Fe_{2+y}$ that we used for performing the neutron scattering experiments to investigate the magnetic phase diagrams for specific compositions are grown and characterised by Dr. William Duncan, in collaboration with Andreas Neubauer and Wolgang

Münzer. The high quality inter-metallic single crystals are grown using the ultra high vacuum (UHV) optical floating zone (OFZ) furnace, at E21 institute of the Technical University of Munich. The polycrystals of the samples are first prepared at Royal Holloway, University of London, UK using a radio frequency induction furnace to make seed and feed rods prior to the single crystal growths. The growth rods are prepared using the 99.99% puratronic Fe and Nb powders which were degassed in UHV down to 10^{-8} mbar before making the rods. The single crystals are then grown by rotating the seed and feed rods using a magnetic mechanism and at the end of the growth a large section of the single crystals with specific compositions are obtained (y = 0.015 and 0.020) with a mosaicity between 0.3^o and 0.4^o.

The composition-temperature phase diagram was established by growing single crystals with varying concentrations and characterising them extensively. [56]. Figure.(3.1) shows the location of the sample that we used for the neutron scattering experiments for different beam times in the phase diagram established by Moroni-Klementowicz *et al.* The single crystals are shown in Figure.(3.2).

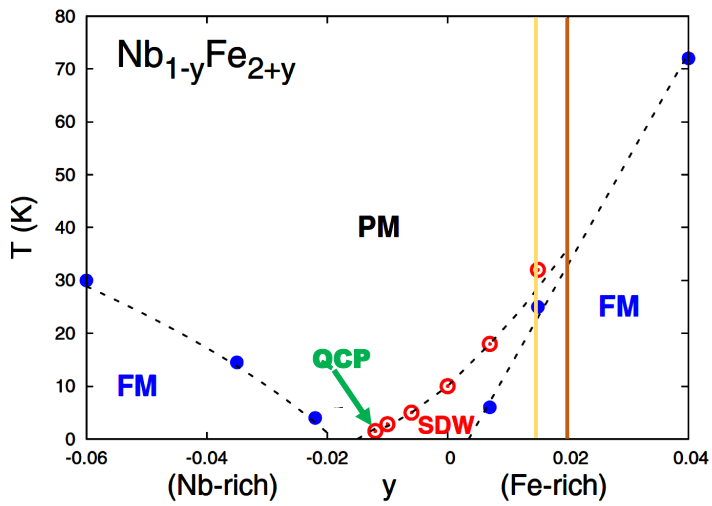

Figure 3.1: The refined composition - temperature phase diagram of $Nb_{1-y}Fe_{2+y}$ system established using the transport and thermodynamic measurements by Moroni-Klementowicz et.al., [27]. The blue solid spheres indicate the Curie temperature (T_C) and the red circles are Neel temperature (T_N). The yellow and brown lines indicates the position of the Fe rich samples with y=0.015 and 0.020 respectively that has been measured. The figure has been adapted from Ref. [27].

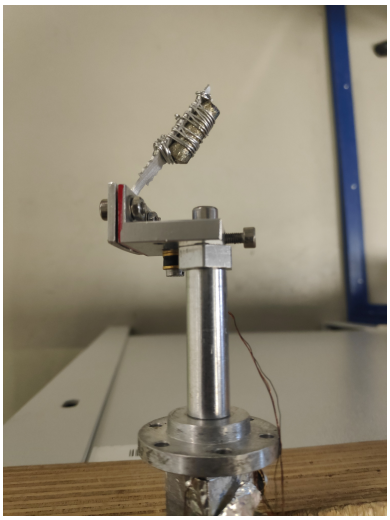

(a)

(b)

Figure 3.2: Samples for performing neutron scattering experiments (a) Fe-rich $Nb_{1-y}Fe_{2+y}$ single crystal (y=0.015), used for the beamtime at MIRA-2 (FRM2, Garhing in Germay). The Al wires are used for tying the sample with the holder rigidly to avoid any misalignments of the orientation while performing magnetic field measurements. (b) Fe-rich $Nb_{1-y}Fe_{2+y}$ single crystal(y=0.020), used for the beamtimes at 4F2 (LLB, Saclay in France), LET (ISIS, Didcot in UK). The cadmium sheet covers at the bottom of the Al holder is to reduce the background noise contribution and the Al wire is for tying the sample with the holder.

3.1.1 Quality of the samples

We studied two large single crystals approximately 6 mm wide and between 15 mm long with compositions $y = 0.015$ and 0.020, designated as OFZ27.3 (3 is the section of the growth it has been cut out from) and OFZ28.3.2.4 (OFZ28 is the name of the growth and 3.2.4 indicates the section of the growth it has been cut out from) respectively [28, 55, 57]. Based on AC susceptibility and magnetisation measurements on fragments of the single crystals, transition temperatures were found for the sample OFZ27.3 and OFZ28.3.2.4 at T_N = 31 K and T_C = 23 K [28], and T_N = 33 K and T_C = 37 K [52] respectively. The quality of the single crystals has also been determined using the resistivity measurement on a small piece from the same growth with a small cross section, revealing the residual resistivity ρ_0 of 16.9 $\mu\Omega cm$ and 17.5 $\mu\Omega cm$ for the sections of samples OFZ27.3 and OFZ28.3.2.4 respectively. A bulk characterization of Neutron Depolarization measurements were used that revealed the level of magnetic homogeneity in the single crystal growths: for sample y = 0.015, the onset of FM has

been found to occur between T=24 K and T=26 K and homogeneous FM is observed below T=19 K [57]. For sample y = 0.020, the onset of FM has been found to occur between T=34 K and T=38.3 K and homogeneous FM is observed below T=30 K [57].

The compositions of the single crystals are then determined utilizing the composition phase diagram established by Moroni-Klementowicz *et al.* through a comprehensive analysis of the composition using wavelength and energy dispersive x-ray spectroscopy (WDXS) on the $Nb_{1-y}Fe_{2+y}$ system [27, 58]. Polycrystalline samples were used for determining the final compositions and it was observed that the final compositions are slightly richer in Nb content than the nominal compositions. Figure.(3.3) shows the average volume per atom of the C14 structure versus the nominal (solid line) and WDXS (dashed line) Nb content.

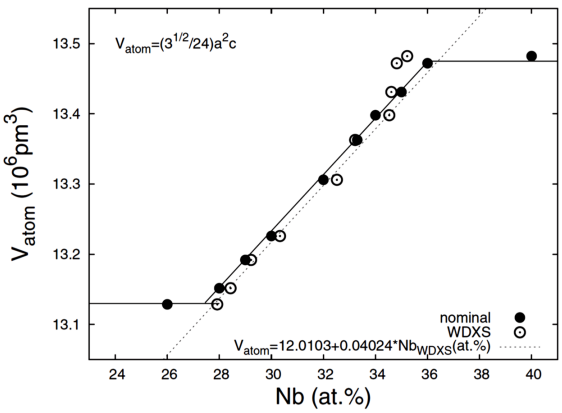

Figure 3.3: Unit-cell volume of the hexagonal C14 Laves phase $Nb_{1-y}Fe_{2+y}$ system calculated from the unit cell parameters versus the nominal and WDXS composition. dashed line indicates the dependence of the average atomic volume on the composition determined by WDXS to extract the compostions of samples with small values of y. The limits of the homogeneity region are 27.4 and 36.3 at. % Nb. The figure is taken from Ref.([27]).

The measurements of WDXS on the samples have shown a linear dependence of the atomic volume on composition in the range 28 and 34 atomic percentage of Nb according to Vegard's volume. By fitting the data using a least square fit function in the linear range, a relation is obtained between Vegard's volume and the sample's Nb content, as given in Equation.(3.1),

$$V_{atom} = 12.0103 + 0.04024x(at.\%Nb_{WDXS}). \tag{3.1}$$

The Equation.(3.1) was used to deduce the compositions of samples with varying y by measuring the lattice parameters. The accuracy in the WDXS experiments was found to be of

the order of 0.1% limiting the accuracy on y to ~ 0.003. A small systemic error of about 0.2 at. % was also observed in the measurements, however, the error would only shift the absolute values without changing the shape of the phase diagram.

3.1.2 Magnetic phase transitions

The existence of the modulated magnetic order (SDW) and the ferromagnetic order (FM) on our crystals have been studied using neutron diffraction [28]. The evolution of the magnetic phases with temperature have been probed on the single crystal y = 0.015 and 0.020 [28]. Figure.(3.4) show the T dependence of the normalized FM intensities, and FM and SDW ordered moments.

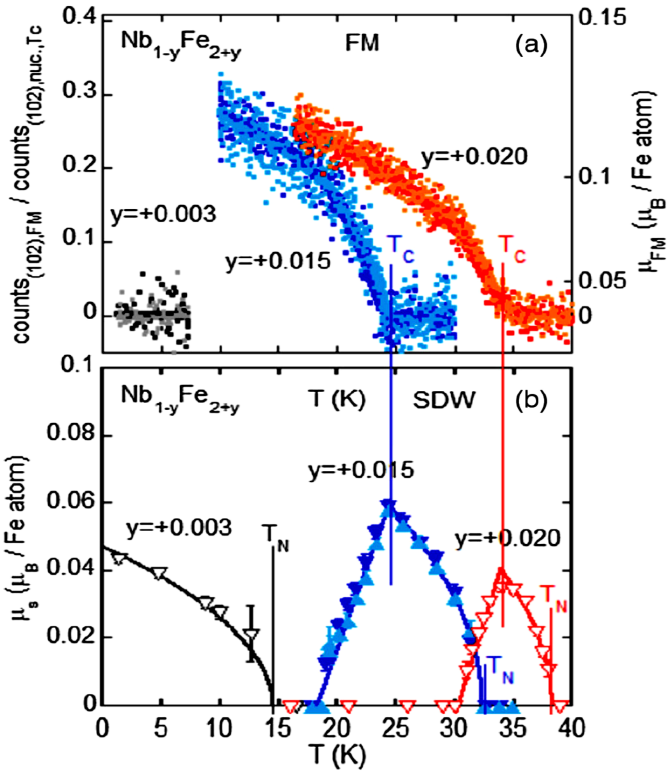

Figure 3.4: T dependence of the normalized FM intensities and FM-ordered moments, SDW-ordered moments obtained through neutron diffraction measurement for samples y = +0.003 (black, gray), +0.015 (dark blue and light blue), +0.020 (red and orange). The upward triangles and downward triangles represent the measurement sequences going down or up in T [28].

From the measurements of the FM signals and the peaks of the SDW signals, the onset temperatures for FM have been found to be at $T_C = 24.5$ K and $T_C = 34$ K for the compositions y = 0.015 and 0.020 respectively. The temperature dependence of the SDW ordered moment

for sample y=0.015 has shown that below T_N= 32.3 K, the SDW order starts to appear and is fully suppressed below T=18.5 K, whereas, for sample y=0.020, the SDW phase start to appear below T_N = 38.3 K and is fully suppressed below T = 30.5 K. The intensities of the SDW phase have been observed as a continuous rise below the onset transition temperature T_N not inconsistent with a second-order PM-SDW transition [28].

Previous measurements of, e.g., χ and ρ have provided evidence that the PM-SDW transition is second order, while the SDW - FM transition is first order [51]. A discontinuous onset of the magnetisation and discontinuous suppression of the SDW ordered moment would therefore be expected at T_C. However, Figure.(3.4) shows a steep but gradual increase of the magnetisation, which is accompanied by a simultaneous steep but gradual suppression of the SDW ordered moment.

This overlap can be attributed to a distribution of the transition temperatures within the sample. The overlap region of the SDW and FM order can be calculated from the onset T_N and T_C measured from the neutron scattering, giving 6 K and 3.5 K for the sample y = 0.015 and 0.020 respectively. The variations in the transition temperature are corresponding to variations in the compositions [28]. In the sample y = 0.015, a temperature variation of T_C by ± 3.0 K corresponds to the variation in the composition y = ± 0.0016, and that leads to the variation in T_N by ± 2.2 K. This causes the transition temperatures measured using neutron scattering to be 3.0 K (2.2 K) lower than the onset temperatures for $T_C(T_N)$. Similarly, for sample y = 0.020, a temperature variation of T_C by ± 1.8 K corresponds to the variation in the composition y = ± 0.0009, and that leads to the variation in the bulk transition temperatures are observed to decrease 1.8 K (1.2 K) below the onset temperatures for $T_C(T_N)$. The homogeneity of the FM order below T = 19 K and 30 K for y = 0.015 and 0.020, where neutron measurements show complete suppression of the SDW order respectively are confirmed using neutron depolarization measurements, suggesting no coexistence of the SDW order below those temperatures ranges [57]. The bulk transition temperature T_N=30.1 K and T_C=21.5 K for sample y=0.015, and T_N=37.1 K and T_C=32.2 K for sample y=0.020, which is in good agreement with the bulk magnetic response traced on these samples.

3.2 Neutron scattering theory

The neutron scattering experiment is a very versatile and powerful experimental method to probe the dynamics and structure of the condensed matter on the atomic and nanometer scale.

The basic properties of the neutron makes their scattering a powerful tool for investigating the important features of the matter. It is generally in the neutron scattering community agreed that the four key characteristics of the thermal neutrons find extremely useful over the other means of experimental techniques to investigate hard, soft, or biological materials.

The value of the mass of the neutron ($m_n = 1.67493 \times 10^{-27}$ Kg) rather close to the proton results in the de Broglie wavelength (around 1.8 Å) of the thermal neutrons being comparable to the inter-atomic distances and an energy (20 meV) similar to the elementary excitations of the condensed matter system can thus provide information on the structural and dynamical details of the system simultaneously [59]. Secondly, because of the fact that the neutrons are electrically neutral particles they are capable of penetrate deep inside the target even very close to the nuclei where they don't need to overcome any Coulomb barrier [60]. Since the neutrons interact with nuclei via strong nuclear forces, the scattering by thermal neutrons can be used for investigating the different isotopes and lightweight elements. The scattering cross section varies in a hugely erratic manner between elements and even between isotopes of the same element the neutron scattering can be used in soft matter and life sciences because of the ability to differentiate even between hydrogen (^1H) and deuterium (^2D) where in the case of X-rays they are virtually transparent to these light weight hydrogen. Since the neutrons can penetrate easily inside the materials, it can be used to probe even the bulky materials with various sorts of environment, for example magnets, furnaces, pressure cells, Cryostats, *etc.* Thirdly, the weak interaction between the neutrons and solids is very useful to investigate the bulk of the sample not just only its surface. Since the higher order effects are generally very small in their interactions they are either ignored or corrected. Therefore, the neutron scattering data can be used for quantitative comparisons to theoretical models. Fourthly, the neutron's magnetic moment (magnetic gyromagnetic ratio, $\gamma = -1.91304$, the nuclear magnetron, $\mu_N = 5.05078 \times 10^{-27}$ J/T and the spin value $s = 1/2$) find its usefulness in probing the magnetic materials and in resolving their magnetic structures. The way neutron interacts with the unpaired electrons in the magnetic atoms, the information regarding the arrangements of the electron spins and the density of distribution of the unpaired electrons can be investigated by scattering the neutrons elastically with the system. On the other hand, the inelastic neutron scattering can be used to probe the magnetic excitations in the system because of the fact that the excitation energies are comparable to the neutron energy, permitting a study of the time dependent spin correlation using this method.

To investigate the various magnetic orders and the possible magnetic quantum criticality

of our sample we used neutron scattering methods of elastic and inelastic using unpolarised (where the spin orientations are not aligned in any specific directions) neutron beams. The common principle of neutron scattering relies mainly on perturbing the system weakly in such a way that it does not alter the intrinsic properties of the system. In our case the system is our sample, the perturbation is the neutron incident on the system which carries the spin. In the following, we will see the important equations of the neutron scattering for unpolarised beams which helps to probe finally the magnetism in the system.

3.2.1 Neutron scattering cross-section

Because the neutrons are quantum particles they exhibit particle-wave duality property [61] during the scattering experiments. When they are created and detected before and after the scattering via nuclear process they behave predominately as particles, respectively. On the other hand, they behave as interfering waves when they are scattered. The wave like nature of the neutron moving with constant velocity v can be ascribed as de Broglie wavelength, given by

$$\lambda = \frac{2\pi\hbar}{mv}, \tag{3.2}$$

where m is the mass of the neutron (1.67493×10^{-27} Kg) and $\hbar$ is the Planck's constant. The wave nature of the neutron is referred in terms of wave number,

$$k = \frac{2\pi}{\lambda}, \tag{3.3}$$

or as wave vector in the same direction as the velocity v:

$$k = \frac{mv}{\hbar}. \tag{3.4}$$

The kinetic energy of the neutron as non-relativistic particle and its momentum are linked by

$$E = \frac{\hbar^2 k^2}{2m}, \tag{3.5}$$

when neutrons are at the room temperature the energy $E \approx k_b T$ and corresponding wavelength $\lambda \approx 2$ Å, which is of the order of inter-atomic distances in the condensed matter [59].

The neutron scattering events are governed the laws of momentum and energy conservation. The energy and momentum of the neutrons during the scattering events will either absorbed into or gained from the scattering system with initial state $E_i = \frac{\hbar^2 k_i^2}{2m}$ and $\hbar k_i$, before and with final state $E_f = \frac{\hbar^2 k_f^2}{2m}$ and $\hbar k_f$, after respectively. The energy ($\hbar\omega$) and momentum ($\hbar k$) gained or lost by the scattering system is give by,

$$\hbar\omega = E_i - E_f, \tag{3.6}$$

$$\hbar k = \hbar k_i - \hbar k_f. \tag{3.7}$$

The scattering of the neutron beams with materials are described by introducing the central concepts of cross sections. First we consider a beam of neutron flux $\varphi(k_i)$ where neutron particles all have momentum k_i given by,

$$\varphi(k_i) = \frac{\text{number of neutron particles impining on a surface per second}}{\text{surface area perpendicular to the neutron beam direction}}, \tag{3.8}$$

we define the neutron scattering cross section denoted by σ, the system's ability to scatter neutrons as:

$$\sigma = \frac{1}{\varphi(k_i)} \cdot \text{number of neutron particles per second}, \tag{3.9}$$

which has the unit of area. The quantity $\varphi(k_i)\sigma$ is the scattering rate of neutrons by the system in all directions with final energy. The scattering intensity divided by the neutron flux makes σ intrinsic to the system and independent of the neutron flux at the particular experimental set-up.

In Figure.(3.5), the scattering cross-section, σ correspond to the surface of the entire sphere surrounded by the sample (in diagram only $1/4^{th}$ of the sphere is shown) where the neutron crossings are counted. In neutron scattering, the angular dependence is most important aspect to investigate the structure and dynamical properties of the system. The dependence of the angle and the neutron scattered in one direction delimited by the particular solid angle $d\Omega$ and crossing the infinitesimal surface dA is described by the quantity called differential scattering cross-section, $d\sigma/d\Omega$ (see Figure.(3.5)) and the scattering rate is $\phi(k_i)(d\sigma/d\Omega)d\Omega$ [62]. The

relation to total number of scattered neutrons per solid angle over all of the 4π solid angle to the differential equation is given by,

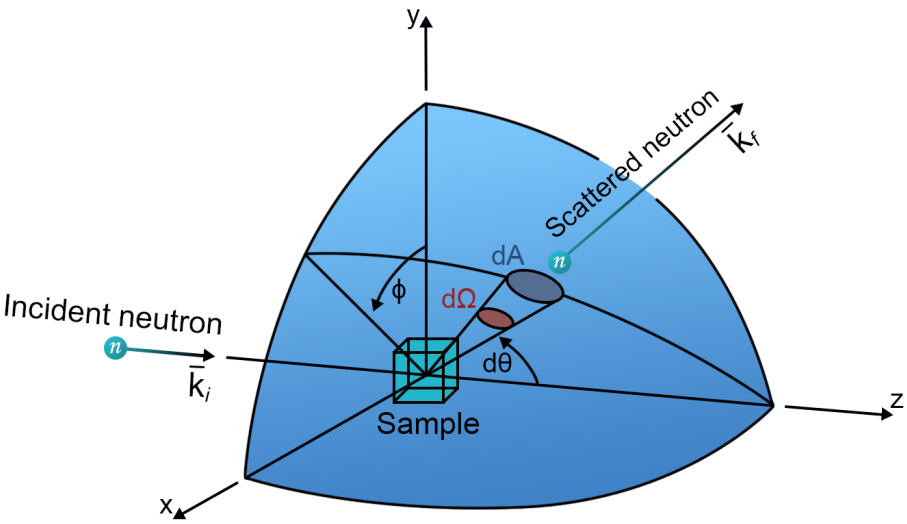

Figure 3.5: An illustration of the neutron scattering cross-section geometry. The incoming neutron k_i incident at the centre of the sample with scattering angle 2θ and azimuthal angle ϕ. The final wave vector k_f of the neutron scattered into the solid angle element of $d\Omega$ (or detector area dA). The picture is taken from [63].

$$\sigma = \int_{\text{all direction}} \frac{d\sigma}{d\Omega} d\Omega. \tag{3.10}$$

As we have seen above that during some neutron scattering process, the neutron exchange energy and momentum to the system which is governed by the energy conservation laws. This type of scattering is called inelastic scattering. For describing the inelastic neutron scattering, the energy dependence of the scattered neutrons must be considered. The quantity which describe this is called partial differential cross section, defined as the scattering of the neutrons by the system only in the the restricted direction $d\Omega$ and the with final energy $E_f \leq E \leq E_f + dE_f$ given as $d^2\sigma/d\Omega dE_f$ and then the scattering rate is $\phi(k_i)d^2\sigma/d\Omega dE_f$, where $\phi(k_i)$ is the neutron flux [62]. The relation to differential equation from the partial differential equation can be reached on integrating over the all final energies E_f, given by

$$\frac{d\sigma}{d\Omega} = \int_{\text{all energies}} \frac{d\sigma^2}{d\Omega dE_f} dE_f. \tag{3.11}$$

The incoming(or initial) neutrons can be represented as a (complex) plane waves [62]. The wave function $\psi_i(z)$ of the incident beam if propagates along z with origin at the scattering

centre, then

$$\psi_i(z) = e^{ik_i z}. \tag{3.12}$$

Due to the spherical symmetry, the wave function of a scattered neutron by a single nucleus at distance r can be represented, as follows [62]

$$\psi_f(z) = -\frac{b}{r} e^{ik_i z}, \tag{3.13}$$

where b is the scattering length, which depends on the nucleus spin state and isotope [62].

If we now consider the scattering process by many centres composed by the targeted system, the number of transitions per unit time and per solid angle $d\Omega$ per dE_f (the partial differential equation), the state of the system from λ_i to λ_f and the state of the neutron changes from k_i to k_f can be represented using Fermi's golden rule, by re-defining the incoming plane wave $\psi(k_i) = e^{ik_i \cdot r}$, the partial differential cross-section for the many scattering centres can be written as [62],

$$\left.\frac{d\sigma^2}{d\Omega dE_f}\right|_{\lambda_i \to \lambda_f} = \frac{k_f}{k_i}\left(\frac{m}{2\pi\hbar^2}\right)^2 \left|\langle k_f \lambda_f | V | k_i \lambda_i \rangle\right|^2 \delta(E_{\lambda_i} - E_{\lambda_f} + E_i - E_f), \tag{3.14}$$

where E_i and E_f are the initial and final energies of the neutron respectively, and E_{λ_i} and E_{λ_f} respectively are the initial and final energies of the scattering system. In mathematical terms the energy distribution of the scattered neutrons is a δ-function [62].

If the potential of the neutron due to the lth nucleus is $V_l(r - r_l)$ then the potential for the whole scattering system is,

$$V = \sum_l V_l(r - r_l). \tag{3.15}$$

Now, in order to consider for all possible scattering process, we average over the possible initial states λ_i and sum over the compatible final states λ_f to obtain the partial differential equation for the whole scattering system [62], given by

$$\left.\frac{d\sigma^2}{d\Omega dE_f}\right|_{\lambda_i \to \lambda_f} = \frac{k_f}{k_i}\left(\frac{m}{2\pi\hbar^2}\right)^2 \sum_{\lambda_i, \lambda_f} p_{\lambda_i} \left| \sum_l \left|\langle \lambda_f | e^{ik \cdot r_l} | \lambda_i \rangle\right|^2 \delta(E_{\lambda_i} - E_{\lambda_f} + E_i - E_f), \tag{3.16}$$

where the statistical weight p_{λ_i} for the state $|\lambda_i\rangle$ is given by the Boltzmann distribution [62]:

$$p_{\lambda_i} = \frac{1}{Z} \exp\left(\frac{-E_{\lambda_i}}{k_B}\right), \tag{3.17}$$

Z is the partition function inserted in the equation to ensure that $\sum_\lambda p_\lambda = 1$, given by

$$Z = \sum_{\lambda_i} \exp\left(\frac{-E_{\lambda_i}}{k_B}\right). \tag{3.18}$$

Because of the random distribution of several different scattering lengths in the scattering system due to the presence of many different atoms, isotopes and with different spins where they generally composed, the partial differential cross section can be written as two terms :

$$\frac{d\sigma^2}{d\omega d\Omega} = \left.\frac{d\sigma^2}{d\omega d\Omega}\right|_{coh} + \left.\frac{d\sigma^2}{d\omega d\Omega}\right|_{incoh} \tag{3.19}$$

where the cooperative effects (e.g., Bragg scattering, magnons, *etc.*) between the atoms and spins in the scattering system obtained from the term $d\sigma^2/d\omega d\Omega\big|_{coh}$ and the dynamics of the system (e.g., motion or diffusion of the individual scattering centre, *etc.*) can be obtained from $d\sigma^2/d\omega d\Omega\big|_{incoh}$ term [64].

The scattering length b of the nucleus varies from one to another due to the nuclear spin or presence of isotopes or both. If we consider b_n as the scattering length of one particular isotope-spin combination which appears in the system with frequency c_n then the average of the scattering length for the system can be written as,

$$\bar{b} = \sum_n c_n b_n, \tag{3.20}$$

this is now the average of the scattering length for the whole scattering system for all spin-isotope combination weighted by the frequency [62]. Therefore the average coherent cross-section can be given as,

$$\sigma_{coh} = 4\pi\bar{b}^2. \tag{3.21}$$

Similarly the total scattering cross-section can be written as [64],

$$\begin{aligned}\sigma &= \sum_l c_l 4\pi b_l^2 \\ &= 4\pi \bar{b}^2.\end{aligned} \tag{3.22}$$

Therefore the total scattering cross-section for the incoherent part can be obtained as $\sigma_{incoh} = \sigma - \sigma_{coh}$, given by

$$\begin{aligned}\sigma_{incoh} &= 4\pi(\bar{b_l^2} - \bar{b}^2) \\ &= 4\pi b_{incoh}^2 \\ b_{incoh} &= \sqrt{\bar{b_l^2} - \bar{b}^2}.\end{aligned} \tag{3.23}$$

Nuclear scattering :

The partial differential cross-section for the nuclear scattering, the potential in the system can be treated as delta function [64]. The Fourier transform of the potential between the lth nucleus in the scattering system with scattering length b_l, given by

$$V_l(k) = \frac{2\pi\hbar^2}{m} b_l. \tag{3.24}$$

Scattering in Bravais crystal : The coherent scattering in Bravais crystal, $i.e$, a crystal with one atom per unit cell, for the pairs of the scattering centres l and l' in the crystal can be written as,

$$\left.\frac{d\sigma^2}{d\omega d\Omega}\right|_{coh} = N\frac{\sigma_{coh}}{4\pi}\frac{k_f}{k_i}S(k,\omega), \tag{3.25}$$

with

$$S(k,\omega) = \frac{1}{2\pi\hbar N}\sum_{l,l'}\int_{-\infty}^{\infty} dt \langle e^{-ik\cdot r_{l'}(0)} e^{ik\cdot r_l(t)}\rangle e^{-i\omega t}, \tag{3.26}$$

where $S(k,\omega)$ is known as coherent scattering function [62].

Similarly, the incoherent nuclear scattering for the independent scattering centres, l in the Bravais lattice can be written as,

$$\left.\frac{d\sigma^2}{d\omega d\Omega}\right|_{incoh} = N\frac{\sigma_{incoh}}{4\pi}\frac{k_f}{k_i}S(k,\omega), \tag{3.27}$$

with

$$S(k,\omega) = \frac{1}{2\pi\hbar N}\sum_l \int_{-\infty}^{\infty} dt\langle e^{-ik\cdot r_l(0)}e^{ik\cdot r_l(t)}\rangle e^{-i\omega t}, \tag{3.28}$$

where $S(k,\omega)$ is known as incoherent scattering function [62].

Principle of detailed balance : During the scattering process, the probability of a neutron to lose or gain energy ($\hbar\omega$) or the system to transits from its initial to final state in either direction are the same. The equal probability for this transitions is give by *principle of detailed balance* function,

$$S(k,\omega) = \exp\Big(\frac{\hbar\omega}{k_bT}\Big)S(-k,-\omega) \tag{3.29}$$

The above equation conveys that it is more probable for a system to be in its lowest energy than the excited state initially. Hence the function $S(k,\omega)$ is shown to increased by a factor of $\exp(\hbar\omega/k_bT)$ [62].

Scattering in non-Bravais crystal : We now consider the case for non-Bravais crystal, *i.e*, a crystal with more than one atom per unit cell. The crystal composed of N unit cells of volume v_0. In the lth unit cell, the position of the scattering centre is defined as, [62],

$$r_{ld} = l + d + u_{ld}, \tag{3.30}$$

where $l+d$ is the position of the scattering centre at equilibrium and u is the displacement out of equilibrium. The coherent scattering in the non-Bravais crystal can be elastic when there is no transfer of energy between neutron and the system ($E_i = E_f$) or inelastic if there is an exchange of energy between them. The coherent differential cross section for the elastic case is given by [62, 64],

$$\left.\frac{d\sigma}{\Omega}\right|_{coh}^{el} = N\frac{(2\pi)^2}{v_0}\sum_G \delta(k-G)\big|F_N(G)\big|^2, \tag{3.31}$$

with nuclear unit cell structure factor,

$$F_N(G) = \sum_d \bar{b_d} e^{iG \cdot d_e} e^{-W_d} \tag{3.32}$$

and

$$W_d = \frac{1}{2} \langle \left[k.u(t) \right]^2 \rangle \tag{3.33}$$

where $\exp(-W_d)$ is known as Debye-Waller factor that accounts for any fluctuations in the equilibrium position of the atom [62]. The incoherent nuclear scattering in the non-Bravais lattice for the elastic case is given by [64],

$$\left. \frac{d\sigma}{d\Omega} \right|_{incoh}^{el} = N \frac{N}{4\pi} \sum_d \sigma_{incoh,d} \exp(-2W_d) \tag{3.34}$$

Magnetic scattering :

During the magnetic scattering process, the magnetic dipole moment of the neutron μ_n interacts with the magnetic fields produced by the unpaired electrons with combination of the magnetic moments due to its spin μ_e and the orbital degrees of freedom [62].

The dipole moment of the neutron and electron are given by,

$$\boldsymbol{\mu_n} = -\gamma \mu_N \boldsymbol{\sigma} \tag{3.35}$$

$$\boldsymbol{\mu}_e = -2\mu_B \boldsymbol{s}, \tag{3.36}$$

where μ_N and μ_B are the nuclear and Bohr magnetron, $\boldsymbol{\sigma}$ and $\boldsymbol{s}$ are the Pauli spin operator and spin angular momentum operators of the neutron and electron respectively. The γ is the gyromagnetic ratio of the neutron, $\gamma = 1.913$. The μ_N and μ_B are given by,

$$\mu_N = \frac{e\hbar}{2m_p} \tag{3.37}$$

$$\mu_B = \frac{e\hbar}{2m_e}, \tag{3.38}$$

where e is the charge of the proton, m_p and m_e are the masses of the proton and electron respectively.

The total magnetic magnetic field produced by the unpaired electron can written as,

$$B = B_S + B_L, \tag{3.39}$$

where B_S is the magnetic field generated by the electron with momentum p at point R due to its magnetic dipole moment, given by

$$B_S = \frac{\mu_0}{4\pi}\frac{\mu_e \times \hat{R}}{R^2}. \tag{3.40}$$

where $\hat{R}$ is a unit vector in the direction of the R. The magnetic field due to the momentum of the electron is given by,

$$B_L = \frac{\mu_0}{4\pi} I \frac{dl \times \hat{R}}{R^2}. \tag{3.41}$$

where Idl is the current element of the moving electron. The total magnetic field due to an electron of momentum p therefore is [62],

$$B = B_S + B_L = \frac{\mu_0}{4\pi}\Big\{curl\Big(\frac{\mu_e \times \hat{R}}{R^2}\Big) - \frac{2mu_B}{\hbar}\frac{p \times \hat{R}}{R^2}\Big\}. \tag{3.42}$$

If we consider the jth electron in the system, the potential $V_{m,j}$ of a neutron in the magnetic field generated by the electron is [62] given by,

$$V_{m,j} = -\mu_n \cdot B_j = -\frac{\mu_0}{4\pi}\gamma\mu_N 2\mu_B \sigma_j \cdot \Big\{\nabla \times \Big(\frac{s_j \times \hat{R}}{R^2}\Big) + \frac{1}{\hbar}\frac{p_j \times \hat{R}}{R^2}\Big\}. \tag{3.43}$$

The total interaction with all the unpaired electrons in the system by neutron therefore given by [62],

$$V_m = \sum_j V_{m,j}. \tag{3.44}$$

In order to obtain the partial differential cross-section for the magnetic scattering we also need to consider the spin state of the neutrons. If $\boldsymbol{\sigma}_i$ and $\boldsymbol{\sigma}_f$ are the initial and final state of the neutron in the scattering process, then the final equation is given by,

$$\left.\frac{d\sigma^2}{d\Omega dE_f}\right|_{\sigma_i\lambda_i\to\sigma_f\lambda_f} = (\gamma r_0)^2\frac{k_f}{k_i}\left|\langle\sigma_f\lambda_f|\boldsymbol{\sigma}\cdot Q_\perp|\sigma_i\lambda_i\rangle\right|^2\delta(E_{\lambda_i}-E_{\lambda_f}+\hbar\omega), \tag{3.45}$$

with [62]

$$r_0 = \frac{\mu_0}{4\pi}\frac{e^2}{m_e} \tag{3.46}$$

where r_0 is the classical electron radius

$$\begin{aligned} Q_\perp &= \sum_j e^i k\cdot r_j\Big\{\hat{k}\times(s_j\times\hat{k}) + \frac{i}{\hbar k}(p_j\times\hat{k})\Big\} \\ &= \hat{k}\times(Q\times\hat{k}) \\ k &= k_f - k_i(\text{scattering vector}). \end{aligned} \tag{3.47}$$

where Q is Fourier transform of the total magnetization operator $M(r)$ and $Q_\perp$ is the vector projection of the Q on to the plane perpendicular to k [62]

$$Q(k) = -\frac{1}{2\mu_B}\int M(r)e^{ik\cdot r}dr = -\frac{1}{2\mu_B}M(k), \tag{3.48}$$

The contribution of the spin and orbital degrees of freedom of the unpaired electrons to the magnetic scattering can be obtained from the equation.(3.48), where it shows the neutrons are scattered by the magnetic fields generated by the unpaired electrons that is normal to the scattering wave vector k in the system.

The Final master equation for the magnetic neutron scattering resulting from the static magnetic moments (elastic scattering) and the fluctuating part (inelastic scattering) of the system is given in Equation.(3.49) [65].

$$\frac{d\sigma^2}{d\Omega dE_f} = \Big(\frac{\gamma r_0}{2\mu_B}\Big)^2\frac{k_f}{k_i}\sum_{\alpha\beta}(\delta_{\alpha\beta}-\hat{k_\alpha}\hat{k_\beta})\Big(\big(2\mu_B\big)^2\langle Q^\alpha(k)\rangle\langle Q^\beta(-k)\rangle\delta(\hbar\omega)+\big(n_b(\hbar\omega)+1\big)\frac{\chi''_{\alpha\beta}(k,\omega)}{\pi}\Big), \tag{3.49}$$

with

$$S_{el}^{\alpha\beta} = \big(2\mu_B\big)^2\langle Q^\alpha(k)\rangle\langle Q^\beta(-k)\rangle\delta(\hbar\omega), \tag{3.50}$$

the elastic part of the Equation.(3.49). And,

$$S_{inel}^{\alpha\beta} = \big(n_b(\hbar\omega) + 1\big)\frac{\chi_{\alpha\beta}^{"}(k,\omega)}{\pi}, \tag{3.51}$$

is the inelastic part of the Equation.(3.49). The part, $\big(n_b(\hbar\omega) + 1\big)$, describes the *principle of detailed balance* and $\chi_{\alpha\beta}^{"}(k,\omega)/\pi$ is the imaginary part of the dynamical magnetic susceptibility [65] which can be calculated using the spin fluctuation theory discussed in chapter 1. The Equation.(3.49) implicitly consists of the Fourier transform of the density $\rho(r)$ called *magnetic form factor* to account for the distribution of the unpaired electron density on an atom, given by

$$F_d(k) = \int \rho(r)e^{ik\cdot r}dr. \tag{3.52}$$

3.3 Neutron scattering instrumentation

The neutron scattering experiments are extensively used to carry out many different researches that deal with the study of condensed matter, life sciences and so forth. To suit the specific needs of the research the instruments are built in many different designs. Based on the method of production of the neutron beams at the sources, they are mainly classified into two, namely the reactor and spallation neutron sources. In a standard reactor source, the neutron beams are produced in a constant rate hence they are called continuous or steady state neutron sources. Typical examples of the continuous reactors include LLB (saclay) and ILL (Grenoble) in France, FRM2 (Garching) in Germany or High-Flux Isotope Reactor (HFIR) (ORNL, Oak Ridge Tennessee) in USA. In the case of spallation, the neutron beams are created by hitting a metal targets like uranium, lead, tungsten [66] with a high-energy protons produced by accelerator for a very short time ($\approx 1\mu s$) with frequency 10 Hz-50 Hz. The neutrons from the metal targets are spalled by using the pulsed beams of accelerated proton so that the neutron beams generated at sources are named pulsed sources. The examples for the pulsed sources include ISIS (Didcot) in UK, SNS in the USA or J-SNS in Japan. The produced neutrons from both the sources come with different energy range which are not always suitable for the scattering experiments, therefore the neutron beams are thermalised to harvest the effective useful energy range for various set of experiments. The useful energy range of the thermal neutrons typically are 50-100 meV [64]. The cold neutrons on the other hand, produced at

the sources using a cryogenic moderator roughly have the energy range of 0.1-10 meV which is very useful for performing the low energy experiments [64]. When the energy needed for the experiments are greater than 100 meV, the hot neutrons are used instead by moderating the neutron beams with graphite at 2400 K like at ILL in Grenoble [64]. The extracted neutron beams (cold, thermal, hot) from the sources are then efficiently transported to the spectrometers for performing various type of experiments.

For our case, the experiments are performed using unpolarised cold neutrons for the elastic and inelastic scattering with triple axis spectrometer (TAS) of the continuous sources (LLB (Saclay) and FRM2 (Garching)) and a multi-choppers spectrometer (MCS) of the pulsed source (ISIS (Ditcot)). In the remainder of this section we will have an overview of the instruments for TAS (4F2, MIRA-2) and MCS (LET) used for different measurements.

3.3.1 Triple axis spectrometer (TAS)

The triple axis spectrometer invented by Bertram Brockhouse at the NRX nuclear experimental reactor in Canada in 1956 is widely used to study the thermal or magnetic excitations in the condensed matter systems. The name TAS refers to the axes of three main components i.e, the monochromator, the sample table and the analyser where the components are used respectively for selecting the incoming neutron energy, to select the q position in the reciprocal lattice of the sample and to select the energy transfer between the neutron and the sample. The monochromator and the analyser typically consists of a materials like copper, beryllium, pyrolytic graphite or germanium crystals. In order to shape the neutron beam before arriving to the monochromator, the white beams are adjusted using several other components of the instrument such as collimators: to remove the components of the beam that are not parallel to the beam axis, beam shutters: which can be used to access the instrument and slits: for adjusting the size of the beam, acting as a diaphragm.

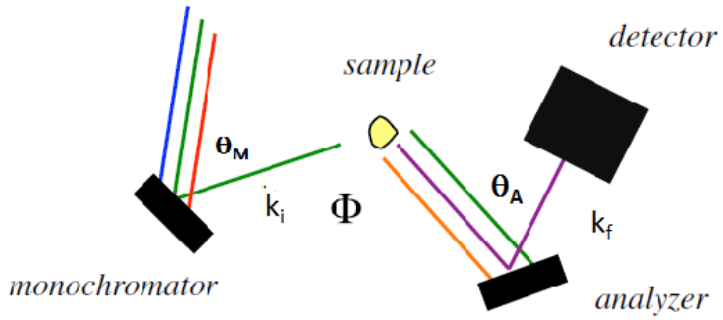

Figure 3.6: A schematic diagram of TAS. Picture is taken from [67]

A schematic diagram of a standard TAS with single monochromator crystal is shown in Figure.(3.6). A initial wave vector (k_i) is selected from a white beam of the neutrons by allowing to scatter through an angle $2\theta_M$ at the monochromator. The selected neutron beam is then made to scatter though an angle Φ in the sample producing scattered neutrons with a broad range of energies and associated final wave vectors. A particular k_f is selected at the analyser by scattering the white beam at a selected Bragg angle $2\theta_A$ to record at the detector. The θ_M and θ_A are changed to suit the need of the measurement for selecting particular energy of the wave vector. With many different combinations of k_i and k_f, the TAS can be used to perform a complete scan of the momentum and energy in the physically accessible range of the reciprocal space of the system.

There are two types of scan modes normally used to investigate the excitations:(1) Constant-Q and (2) Constant-E method. The Constant-Q method commonly used to probe the phonons (quantized lattice vibrations) and magnons (quantized spin waves) whereas the constant energy transfer $\hbar\omega$ is used for probing the excitations (particles with low lying excited states, For example, quasi particles and collective excitations). The both methods satisfy the laws of conservation of scattering vector (Q) and energy ($\hbar\omega$) between the sample and the neutron, given by

$$\begin{aligned} \hbar Q &= \hbar(k_f - k_i) \\ \hbar\omega &= \frac{\hbar^2 k_i^2}{2m_n} - \frac{\hbar^2 k_f^2}{2m_n} \end{aligned} \tag{3.53}$$

3.3.1.1 4F2 - LLB

In a standared TAS with single monochromator to probe the system, the entire spectrometer has to move in order to select for each different desired incident neutron energy. Due to the requirement for a substantial flooring arrangement for the instrument to move, the options for selecting any range of k_i to scan the sample is limited. 4F2 TAS (Saclay) instrument located at the cold neutron source at Laboratoire Lèon Brillouin (LLB) in France overcome this issue with its double monochromator arrangement. The monochromators are arranged inside the shielding where one monochromator is flat and the second one is curved and vertically focused on the sample [64]. Although the 4F2 has the advantage of reduced background and fixed position of the sample table it has the disadvantage of reduction in the intensity due to additional reflections and the increased neutron flight path [64].

Figure.(3.7) shows the instrument set-up for the 4F2 at LLB. The double monochromator crystals are made by pyrolytic graphite providing the wavelengths between 6 and 2 Å($1.05 < k_i < 2.7$ Å^{-1}). This spectrometer is well suited for measuring various excitations with low energy transfers ($\hbar\omega < 4$ meV). The k_i dependence of the energy resolution is shown in Figure(3.8). To measure the sample at different values and directions of the magnetic field, different magnets are available to use. For measuring sample in horizontal direction up to 0.7 to 1.4 T electromagnets are used. For vertical fields up to 0.14 T the Helmoltz coils and for up to 1.4 T electromagnet is used. To measure samples at temperatures ranging from 300 K to 1.5 K ^{4}He cryostat is used. For filtering out the higher order neutrons from the incoming beam cooled Be or a graphite filters are used. The scattered neutrons are detected using ^{3}He detectors [68].

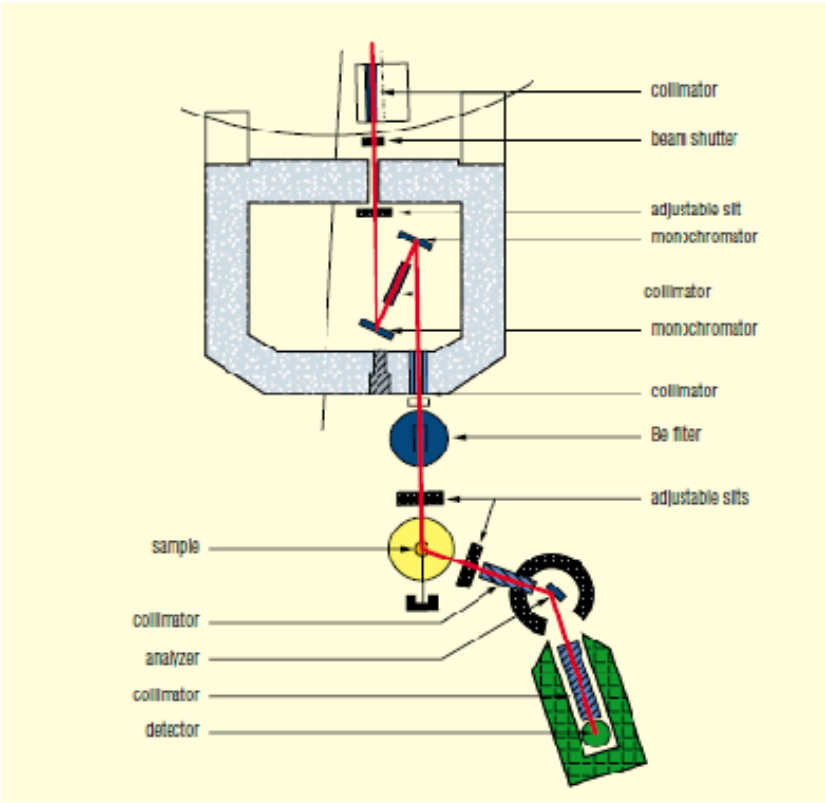

Figure 3.7: Schematic representation of TAS of the 4F2 instrument at the LLB (Saclay) in France. The picture is taken from [68].

The incoming neutron flux (k_i) measured by the monitor is also sensitive to unfiltered higher harmonic neutrons by the monochromator, the monitor counts were therefore corrected for higher order neutrons. The experimentally determined k_i dependent correction factor [69] shown in Figure.(3.9) is therefore applied to the monitor neutron counts. The data of the k_i dependent correction factor is fitted using the polynomial given in Equation.(3.54), the coefficient a_n's and a constant determined were given in Table.(3.1).

$$C(k_i) = \sum_{n=1}^{9} a_n k_i + constant \tag{3.54}$$

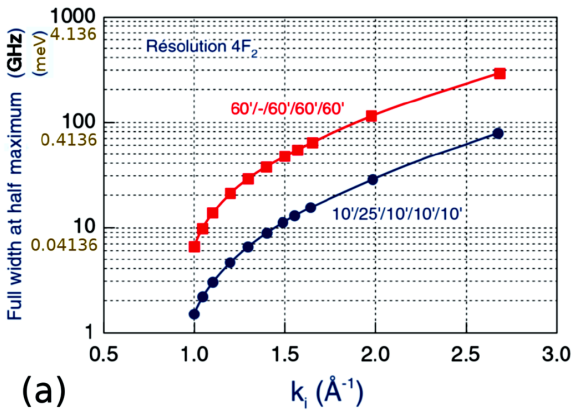

Figure 3.8: The incident wave vector k_i dependence of energy resolution of 4F2, Collimations respectively are : in-pile/M1-M2/M2-sample/sample-analyzer/analyzer-counter. Picture is taken from [68].

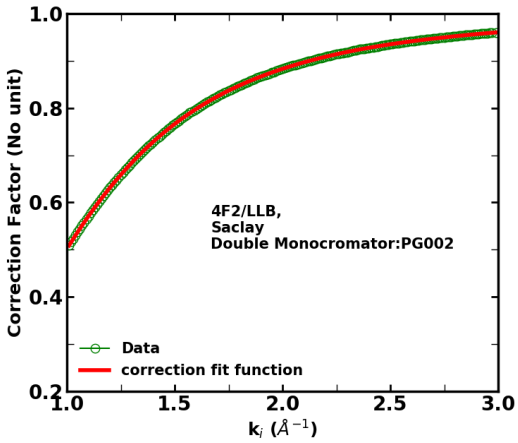

Figure 3.9: 4F2 monitor higher harmonic correction function [69].

Table 3.1: The fit values for coefficients of the k_i dependent monitor correction factor function (Equation.(3.54)).

Coefficients	fit values
a_1	-8.013220
a_2	21.028071
a_3	-27.291570
a_4	21.969787
a_5	-11.712000
a_6	4.154766
a_7	-0.943714
a_8	0.124103
a_9	-0.007177
constant	1.192220

The neutron scattering data that we collected using 4F2 are by varying k_i in our experiments at LLB. Therefore the monitor count values are corrected using the experimentally determined k_i dependent correction factor [69].

3.3.1.2 MIRA-2 - FRM2

MIRA is multipurpose instrument used for measuring various low energy excitations with excellent resolution in momentum transfer and reduced background noise operating at FRM2 (Garching) in Germany [70]. MIRA has two beam ports MIRA-I and MIRA-2 that use cold neutrons from the reactor to perform experiments. To investigate our sample we used MIRA-2 beamport in TAS mode shown in Figure.(3.10).

The range of the wavelengths that can be extracted from the two beam ports is 3.5 Å$\leq \lambda \leq$ 20 Å. From an array of seven horizontally focusing HOPG monochromators the MIRA-2 can offer shorter wavelengths for probing the systems. The higher order neutrons are filtered out using a cooled Be-filters. For measuring the samples in the certain environments MIRA-2 is fully compatible to various environments available at FRM-2 such as dry cryostats, furnaces and magnets. Low temperature measurements for temperatures ranging from room temperature down to 3 K can be achieved using a cryogenic free closed-cycle cryostat. To study the sample in the modest magnetic field, a water cooled electromagnet which can rotate independently

delivering the field from -0.3 T to 0.3 T can be used. For fields up to 7.5 T, cryo-magnet of the FRM II is used. In addition, Helmholtz coil set ups capable of producing fields up to 2.2 and 0.3 T are also available. In the TAS mode MIRA-2 can offer resolution $\delta Q = 0.014$ Åat Q=2 Å^{-1} and an incident energy 4 meV [70].

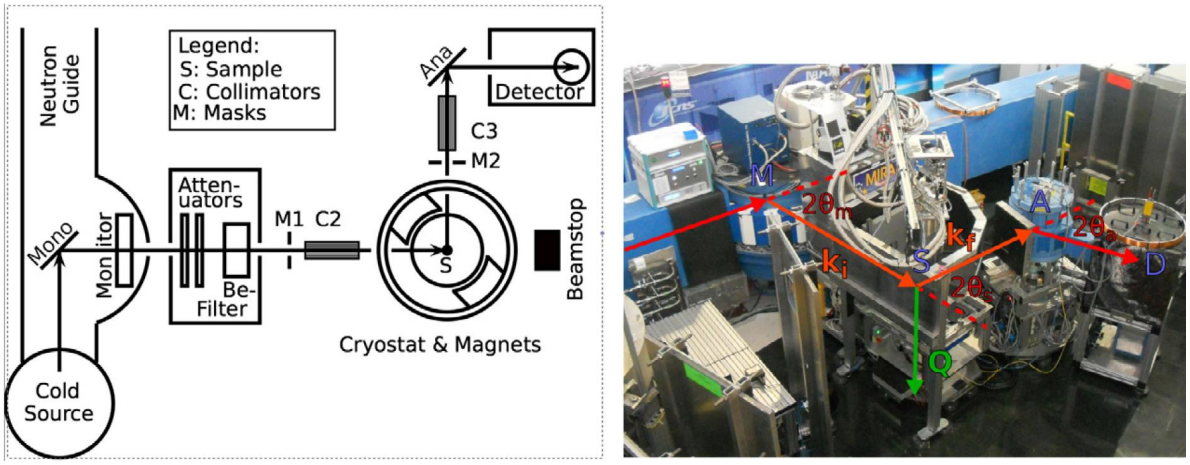

(a) (b)

Figure 3.10: A schematic and instrument set-up of MIRA2 at FMR2 (Garhing) in Germany. (a) Schematic view showing MIRA 2 in TAS mode. M, C and S are monochromator, collimator and sample respectively. (b) MIRA 2 instrument with a sketch of the beam path (offset for clarity): are incoming neutron beam (k_i), the out-going beam (k_f), the monochromator take-off angle ($2\theta_m$), the scattering angle (θ_s) and the direction of the momentum transfer Q [70] . The picture is taken from [70].

3.3.2 Multi-choppers spectrometer (MCS)

The multi-chopper spectrometer (MCS) is a direct geometry neutron scattering instrument used extensively for surveying the excitations with various energies simultaneously using a monochromatic pulse of neutrons with different E_i's in the extended region of (Q, ω) space using time-of-flight (TOF) technique. The TOF technique is a method that generally determines the kinetic energies of the neutrons from the time that they take to travel from one point to another if the distances are known. The monochromatization of the neutron pulses are achieved with a crystal followed by a cascade of disk choppers that take care of the desired velocities required for the need of the experiment for scattering it on the sample. The significant advantage of the MCS over the TAS is that its ability to scan the sample in a wide regions of phase space where multiple detectors are used to collect the scattered neutron with different energies. However,

the the ability to measure wide regions of the reciprocal space comes with a disadvantage of significant reduction in the intensity on the sample due to the pulsed nature of the neutrons. This has been remedied with a new breed of direct geometry spectrometer LET located at ISIS(Ditcot), UK [71].

3.3.2.1 LET - ISIS

LET is a cold neutron multi-chopper direct geometry spectrometer installed on a target station 2 (TS2) with target metal Tungsten located at ISIS (Ditcot), UK and operated by STFC. From the frequency 50 Hz of the synchrotron, the TS2 take one pulse in five from the existing machine with a duty cycle of 10 Hz. It is a versatile spectrometer to investigate the excitations with the energy resolution over a wide range from 8μeV to 80 meV [71]. To measure the samples at different temperatures a ^{4}He cryostat with a rotation stage is used that offers temperature ranges from 1.8 to 300 K.

Figure.(3.11a) illustrates the schematic diagram of the LET spectrometer. The LET spectrometer positioned at the port of W6 in the TS2 with a flight path between moderator and sample of 25 m. The neutron pulses are transported to the sample with a straight super-mirror guide. To shape the pulses arriving from the moderator a total of five disk choppers are used before scattering it on the sample for the purpose of shaping (chopper 1), to correct for the frame overlap (chopper 2), pulse removal (chopper 3), containment removal (chopper 4) and for selecting the desired resolution (chopper 5) of the neutron pulse with a characteristic width.

The samples are kept for the measurement 25 m away from the moderator inside a tank of volume 100 m^3 with no windows between sample and detectors which is 3.5 m away. To achieve the high intensity neutron pulse a solid methane material is used as the moderators. The chopper disks are made out of carbon fibre composite material with coatings of ^{10}B for absorbing unwanted neutrons [71]. The role of the choppers are illustrated in the Figure.(3.11b) for the case of three measured incident neutron energies, E_i = 5 meV, 1.5 meV and 0.7 meV. The blue lines represent the trajectories of the neutrons after the scattering event through the multiple choppers. The split in the trajectories after the sample indicate the neutrons arrived at the detectors with different energies with a gain or loss of energy transfers from the sample. The red lines in the Figure.(3.11a) represent the ^{3}He position sensitive detectors (PSD) composed of 4 m long 384 vertical tubes with diameter 1 inch at 10 atm pressure, arranged in a half circle fashion by covering the sample at its centre. The tubes are kept straight by small aluminium straps at the 1/3 and 2/3 positions. When a neutron hits the detector array,

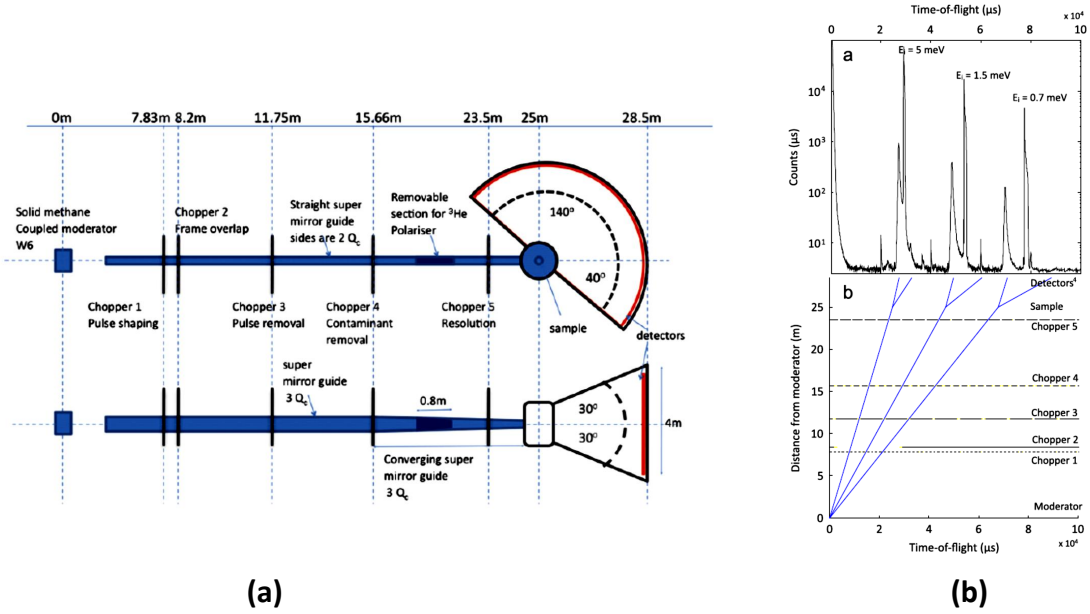

Figure 3.11: (a): Global illustration of the LET instrument set-up. (b): (Top) Integrated flux measured as a function of time from detectors for a vanadium sample. (Bottom) Trajectory of the neutron pulses from moderator to detector indicating the role of five choppers represented in blue line [71]. The picture is taken from [71].

it counts the number of neutrons using the nuclear reaction that takes place between neutron and the ^{3}He, given by

$$^3_2He +^1_0 n \rightarrow^3_1 T +^1_1 p, \tag{3.55}$$

where ^{3}He is the helium isotope, ^1_0n is a neutron, ^3_1T is a tritium and ^1_1p is a proton. The counts of the neutrons are made by measuring the current that generated in the Pt wire at the centre of the tube where the proton hits.

The measured scattering data S (Q, ω) at the detector is a function of momentum and frequency measured in four dimensional manifold in the reciprocal space (three reciprocal space directions and energy) of the sample [73]. For a fixed E_i and the sample orientation the coordinate frame for a Q position that was chosen in the sample is $Q_\alpha = Q_\alpha\ (\theta, \phi, t_{det}, \Psi)$ where θ and ϕ are the spherical polar coordinates which defines the direction of the final wave vector k_f, t_{det} is the time of arrival to the detectors which in turn has the one to one correspondence with the energy transfers, Ψ is the rotation of the sample about an axis by some angle to scan the reciprocal space and the subscript α = 1-4. Since the four variables in the four dimensional volume are independent of each other, the excitations can be visualized

along any chosen direction. Since the data after the acquisition are automatically corrected and normalised by the instrument software called Horace, no other manual corrections are needed to perform except for the background correction [73].

3.4 Analysis software

To fit and analyse the data collected at various neutron scattering experiments, we used Python codes written by Dr James Poulten and improved and adapted further by Dr Marijn Lucas and myself. We mainly used curve fitting optimization that uses the non-linear least squares to fit model functions to data. In addition to Python programming, to make different phase diagrams and plots of the neutron scattering data I have also used Matlab programming language. To visualize and analyse the large datasets measured with LET instrument we used Horace software which is a set of programs that can be used to build, visualize and analyse the large datasets from time-of-flight neutron inelastic scattering spectrometers [73].

4

Magnetic phase diagrams of Fe-rich $NbFe_2$ system

In Chapter(2), the composition-temperature phase diagram of $Nb_{1-y}Fe_{2+y}$ in zero field was reviewed. Fe-rich samples show a FM ground state. Approaching the FM quantum phase transition near the stoichiometric composition a SDW phase emerges that masks the FM quantum critical point. This chapter contains the results of elastic neutron scattering measurements of $Nb_{1-y}Fe_{2+y}$ in a magnetic field.

4.1 Introduction

Due to the anisotropic nature of $Nb_{1-y}Fe_{2+y}$ system the application of a magnetic field in different directions leads to different phase diagrams. Two cases have been explored: the field has been applied along the magnetic easy axis (H‖c) and perpendicular to it (H‖a). For H‖c the presence of a field-induced tricritical point (TCP) has previously been indicated [51]. A main motivation to explore the H‖a case has been to test whether the transverse field can suppress the easy c-axis FM state and lead to a field-induced FM QCP. This chapter is organised as follows: the remainder of this section will contain background information on $Nb_{1-y}Fe_{2+y}$ system in a longitudinal field H‖c (Subsection.(4.1.1)) and in a transverse field H‖a (Subsection.(4.1.2)). Data fitting of elastic neutron scattering for both field directions is described in Section.(4.2). The elastic neutron scattering measurements are discussed in Section.(4.3) for the H‖c case and in Section.(4.4) for the H‖a case.

4.1.1 Longitudinal field H‖c

Recently, the studies of the $Nb_{1-y}Fe_{2+y}$ system by Friedemann *et.al.* [51] in the longitudinal field H‖c have shown the indications of TCP, a point where the three-phase coexistence ends

and χ_q is expected to become critical at Q_{FM} and Q_{SDW} [51]. The existence of the TCPs at finite field and temperature was observed from the measurements of AC susceptibility for a series of $Nb_{1-y}Fe_{2+y}$ samples. A scalar two-order parameter Landau model for a system with second order SDW transition and first order FM transition reproduces the TCP in the H‖c-T phase diagram. Also, it describes the location of avoided FM-QCP accurately inside the emergent SDW dome, and the existence of quantum tri-critical point (QTCP) at a finite field. At the TCP, the critical fluctuations are associated with both SDW and FM phases, therefore it is argued that the seemingly contradictory temperature dependence of the heat and resistivity near the SDW QCP is due to the contributions of the SDW and FM fluctuations to the excitation spectrum associated with the QTCP. The theory in terms of scalar order parameters (the scalar description of the order parameter in an easy-axis system like $NbFe_2$ is adequate only as long as the fields point in the easy axis (H‖c)) is formulated by expanding the Landau free energy in terms of the two-order parameters, given as,

$$\frac{F}{\mu_0} = \frac{a}{2}M^2 + \frac{b}{4}M^4 + \frac{\alpha}{2}P^2 + \frac{\beta}{4}P^4 + \frac{\eta}{2}P^2M^2 - HM \tag{4.1}$$

where M denotes the uniform magnetization, which couples linearly to the applied magnetic field whereas P denotes a general further order parameter which does not couple directly to the field but has a biquadratic coupling to the uniform magnetization [51]. Here, the order parameter P is associated with the SDW phase.

When the magnetic field is zero, the minima of the global free energy will correspond to either paramagnetic state $M = P = 0$ or one of the possible states $M = 0$, $P \neq 0$, $M \neq 0$, $P = 0$, or $M \neq 0$, $P \neq 0$ depending on the parameters $\{a, b, \alpha, \beta, \eta\}$. From the extensive studies of the polycrystalline and single crystal samples of $NbFe_2$, in zero field, it has been observed that the mixed phase $M \neq 0$, $P \neq 0$ does not occur and cooling the system first the SDW order emerges and then it is replaced by uniform magnetization. This behaviour constrains the temperature coefficient $\alpha(T)$ to go through zero at a higher temperature than $a(T)$. For finite fields, the expected schematic H‖c-T phase diagram based on Landau's two-order parameter theory depending on the sample composition is shown in Figure.(4.1). The Figure.(4.1) shows the accessible parts of the phase diagrams: in a slightly Nb-rich sample only the top part of the SDW phase is observed. For stoichiometry $NbFe_2$ sample, the TCP is exposed with a cut-off just below the tri-critical temperature (T^*). In the Fe-rich sample, all aspects of the phase diagrams are observed.

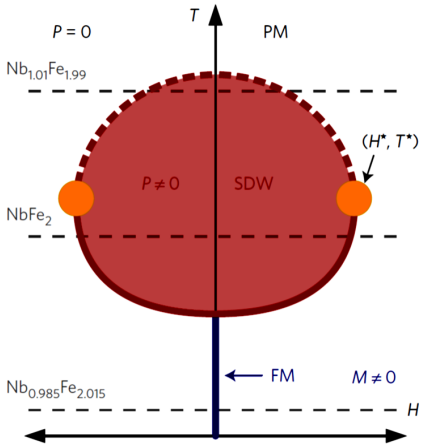

Figure 4.1: Schematic phase diagram based on the Landau's two order parameter model as applied to $Nb_{1-y}Fe_{2+y}$. Solid blue and red lines indicate the first order transition phase boundary of the SDW and FM phases. Red dashed lines indicate the second order SDW phase boundary between SDW and PM phases at high temperatures. The orange circles indicate the tricritical points. Gray horizontal lines are the zero temperature assigned to different samples of the compositions $Nb_{1-y}Fe_{2+y}$. The image is taken from Ref [51].

The magnetic phase diagram established for the $Nb_{0.985}Fe_{2.015}$ single crystal sample including the TCP is shown in Figure.(4.2). The temperatures of the anomalies at T_N and T_C signalling the second order SDW-PM and first order FM-SDW transition, respectively, approaching towards each other with field (see Figure.(4.2)) and merge at $H_{tr} \simeq 60$ mT and $T_{tr} \simeq 28$ K.

The SDW-PM transition remains second order up to H_{tr}, therefore, critical fluctuations at Q_{SDW} are expected along the whole phase transition line up to H_{tr}. The FM-SDW first order but ends in critical point at H_{tr} (therefore, critical fluctuations at Q_{FM} are expected at H_{tr} only) and this is indicated by the strong enhancement of the susceptibility ($\chi'(H,T)$) observed at the merger of two signatures at $H_{tr} \simeq 60$ mT and $T_{tr} \simeq 28$ K. For fields above H_{tr} only a weak maxima reminiscent of crossovers are observed in the susceptibility.

By extrapolating the line of TCPs to zero temperature and at finite field the existence of quantum tricritical point (QTCP) at which both the uniform and finite wave vector diverge in the $Nb_{1-y}Fe_{1+y}$ system has been established. The global H‖c-y-T generic phase diagram obtained from the results of the experimental analysis and the use of two-order parameter Landau theory is shown in the Figure.(4.3).

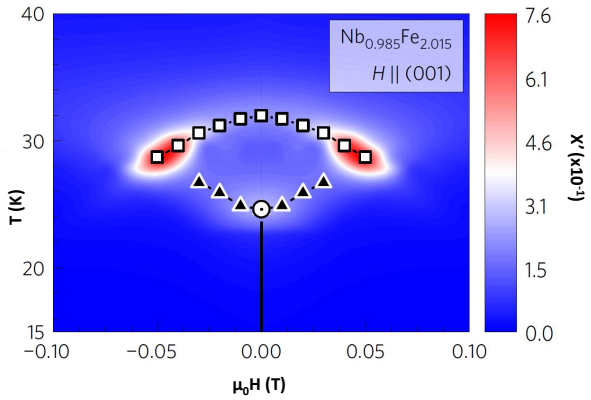

Figure 4.2: H‖c - T phase diagram for $Nb_{0.985}Fe_{2.015}$ single crystal. Colour represents the real part of the AC magnetic susceptibility $\chi'(H,T)$ as a function of field and temperature. Markers indicate the second-order transition at T_N (white squares), the bulk Curie temperature at T_C (solid black triangle) and the first order bulk Curie temperature T_C at zero field (white circle) [51].

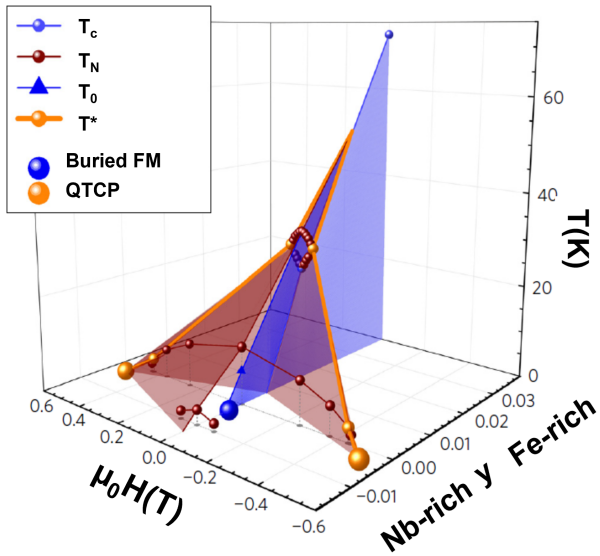

Figure 4.3: The global phase diagram of $Nb_{1-y}Fe_{2+y}$ system with axes spanned in the space are over all composition (y), magnetic field (μH) and temperature(T). The highlighted are the position of the FM-QCP (blue ball) and QTCPs (orange ball). the underlying ferromagnetic transition temperatures are obtained from the Arrott plots analysis a(T_0)=0 of the system. The SDW and FM phase boundaries are obtained from the magnetization and susceptibility measurements [51].

4.1.2 Transverse field H‖a

While the FM-QCP is masked by SDW order at zero fields the application of a transverse field (H‖a, i.e., perpendicular to the magnetic easy axis) creates the possibility to reach a ferromagnetic quantum phase transition (FM QPT), or even an FM QCP depending on the nature of the transition after the point where the merger of second-order SDW and first order FM phase boundaries takes place (dashed blue line in Figure.(4.4)). For H‖a, Landau's two-order parameter model would have to be formulated using the vector order parameters because of the more complicated coupling terms to the applied field in contrary to the H‖c phase diagram. Such a model has not yet been developed for $NbFe_2$.

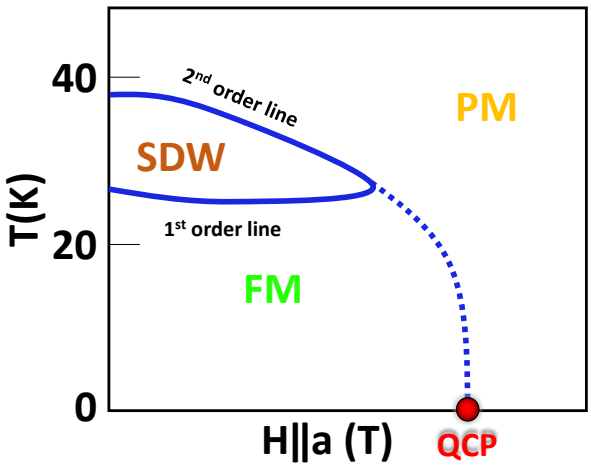

Figure 4.4: Speculative schematic H‖a-T phase diagram for $Nb_{1-y}Fe_{2+y}$ system in transverse field for the case where the FM transition turns second order at high field.

Nevertheless, one can anticipate that the application of the magnetic field destabilizes not only the SDW order but the application of the field perpendicular to the magnetic easy axis (i.e., the c axis) should also suppress the FM order, so, both magnetic phases are expected to be suppressed by a H‖a field. There are three main scenarios for the change from the FM state with moments along c to the field-polarised state with moments along a: 1. the first order transition terminates in a TCP similar to the H‖c case and a crossover via increased canting of the moments is found that is suppressed to lower temperatures with increased field; 2. the first-order FM transition continues to higher fields and is suppressed at a QPT; 3. the FM

transition turns second-order and is suppressed at an unmasked FM QCP.

4.2 Data fitting

In neutron diffraction the SDW phase appears in the data as satellite peaks of the nuclear and FM peak positions, $Q_{SDW} = (Q_{FM} \pm \ell_{SDW})$. Independent of the field direction the SDW satellite peaks have first been normalized and then fitted with a standard Gaussian distribution plus a constant background function. The data fit function is given in Equation.(4.2).

$$f(x) = A\mathrm{e}^{-(\frac{(\mathrm{x}-\mathrm{b})^2}{2\sigma_{\mathrm{x}}^2})} + cst \tag{4.2}$$

where A is the amplitude, b is the peak position (indicates the position of ℓ_{SDW}), σ_x is standard deviation and cst is the constant background. The onset transition temperatures of the SDW order at different fields are determined from the temperature dependence of the satellite peak properties peak intensity (I), Full Width at Half Maxima ($FWHM$) and the peak position (ℓ_{SDW}). The $FWHM$ is calculated using Equation.(4.3) and the peak intensity is calculated using the Equation.(4.4).

$$FWHM = 2\sqrt{2ln2\sigma_x} \approx 2.355\sigma_x \tag{4.3}$$

$$I(B,T) = FWHM * A \tag{4.4}$$

The onset temperature (T_C) of FM order is deduced from the temperature dependence of the FM peak (Q_{FM}) intensity by applying the phenomenological fit function based on the Landau's mean field approach (see Section.(1.5)) as given in Equation (4.5)

$$f(T) = a * T + b * \left\{ \frac{(1 - \frac{T}{T_C}) + \left|(1 - \frac{T}{T_C})\right|}{2} \right\}^{0.5} + cst \tag{4.5}$$

where a, b, T_c, and the constant background cst are fit parameters [30, 34].

4.3 Phase diagram for H‖c

In this section we establish the H‖c-T phase diagram using neutron diffraction measurements by analysing the temperature dependence of the SDW peaks and FM peak (Q_{FM}) intensities at different fields (H‖c). The neutron diffraction measurements have been performed on a high quality $Nb_{0.985}Fe_{2.015}$ single crystal using triple axis spectrometer MIRA-II at FRM 2.

4.3.1 Data acquisition and correction

The elastic neutron scattering has been performed on a single crystal $Nb_{0.985}Fe_{2.015}$ with the support of the beam scientist Dr Markos Skoulatos, MIRA-2 instrument, FRM-2. The sample has been oriented with a* and c* axes in the horizontal scattering plane. The higher order neutrons from the incoming neutron flux ($2k_i$, $3k_i$) were eliminated by using a Be-filters. The vertical and horizontal alignments of monocromator and analyser were kept focused and flat respectively. The uniform magnetic field H‖c was produced using a 2.2 T Helmholtz coil set-up. The SDW order has been observed via intensity scans across the satellite peak at (1 0 -2+ℓ_{SDW}) position. FM order has been studied via temperature scans at the Bragg reflection at (1 0 2) where it was observed the nuclear Bragg peak background is comparatively weak. Table.4.1 summarizes the instrument settings.

Table 4.1: MIRA-II experimental Settings for the neutron diffraction.

	MIRA-II
Scattering Plane	*(1 0 -2) - for SDW, (1 0 2) - for FM*
Monochromator horizontal	Flat
Monochromator vertical	Focused
Analyser horizontal	Flat
Analyser vertical	Focused
$k_i = k_f$	1.55 $Å^{-1}$
Collimation	No
High order filter	Beryllium
Scattering mode	Elastic

Previous studies of the temperature dependence of the SDW satellite peaks have revealed that there is no significant thermal hysteresis with regards to the values of T_N and T_C, but that there is thermal hysteresis with regards to the precise SDW ordering wave vectors. [28,55]. Therefore, for the purpose of establishing the H||c-T phase diagram we used decreasing steps of 1 K in temperature only between intensity scans across the SDW peaks. To determine T_C up-sweeps in temperature were used.

4.3.2 Neutron diffraction analysis and results

Only a set of representative scans of the neutron diffraction data are presented in this section. Before data fitting we first normalized the data to a monitor value of $\approx$ 38000 counts corresponding to an exposure time of approximately 5 minutes.

The zero-field temperature dependence of the SDW peak evolution measured in the temperature range between 34 K and 17 K around the Q position (1 0 -2+ℓ_{SDW}) is shown in Figures.(4.5a & 4.5b). The SDW peaks are fitted using Equation.(4.2). We can see from the figures that as the temperature is lowered a peak signalling the onset of the SDW order begins to emerge at temperature $T_N \approx 32$ K. The amplitude of the peak reaches maximum at T $\approx$ 24 K and then the peak is getting suppressed completely again below the temperature T $\approx$ 18 K. The suppression of the peak is expected given the ordering of ferromagnetism below temperature $T_C \approx 18$ K as observed similarly in the previous measurements [28].

The SDW peak intensity normalised to the value at 24 K displayed in Figure.(4.5c). The normalised intensities shows rise and fall in its value with temperature. The $FWHM$ of the SDW peak shown in Figure.(4.5d) calculated via Equation.(4.3) stays fairly constant but gets slightly broadening at low temperature. The peak position ℓ_{SDW} of the SDW order shown in Figure.(4.5e) is fairly constant between 32 K and 18 K but slightly moving towards the nearest nuclear ℓ_{FM} value of -2 below 26 K.

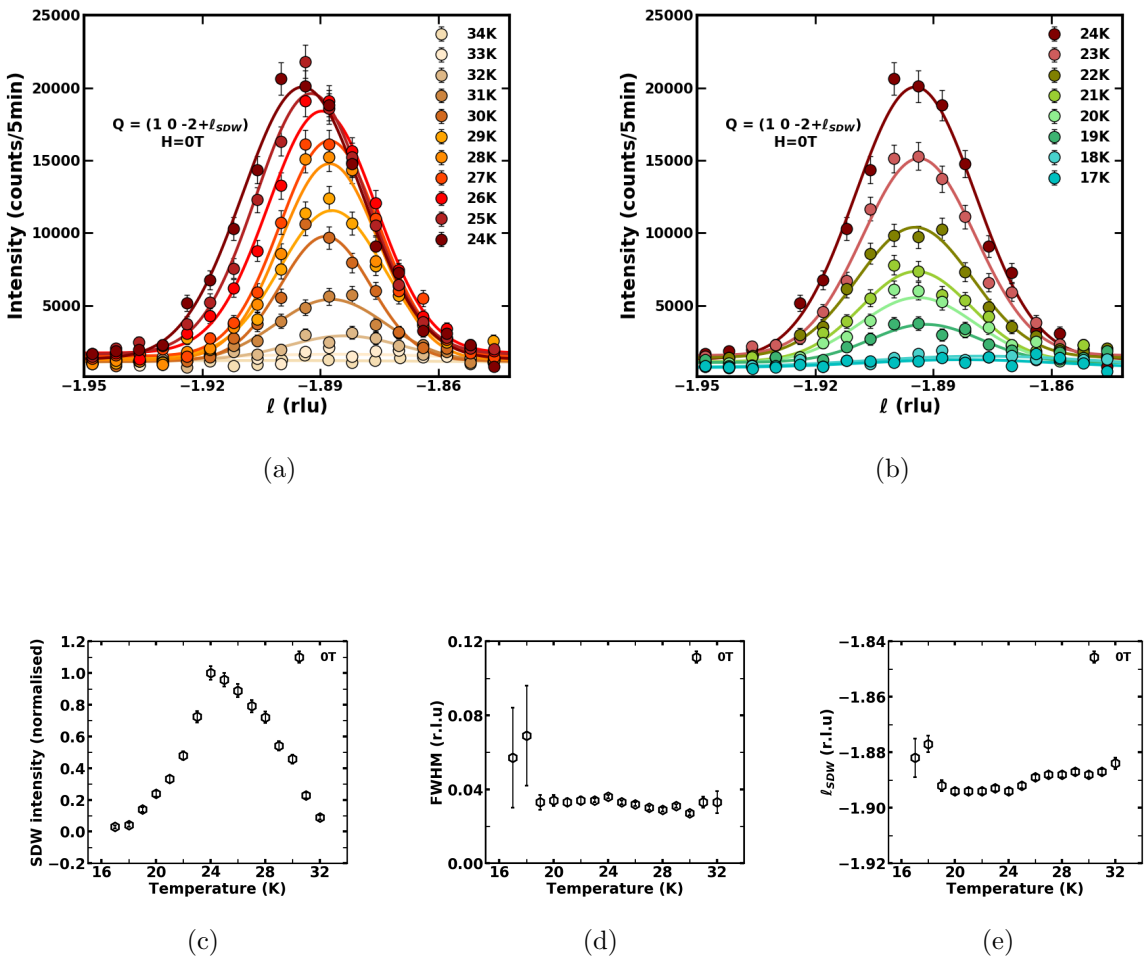

Figure 4.5: Top: (a)&(b) The temperature dependence of the SDW peak in zero magnetic field at (1 0 -2+ℓ_{SDW}) between the temperature range 34K and 17K. The solid lines are Gaussian fits (Eq.4.2). Bottom: The SDW peak properties at different temperatures: (c) SDW intensity, (d) FWHM (calculated using Equation.(4.3)), (e) ℓ_{SDW} value.

Equivalent measurements of the SDW peak at H=30 mT between 34 K and 17 K are shown in Figures.(4.6a & 4.6b). At this field the peak begins to emerge at $T_N \approx 31$ K. The amplitude of the peak reaches maximum at T $\approx$ 28 K and then the peak is getting suppressed completely at T $\approx$ 21 K indicating the ordering of ferromagnetism. Figure.(4.6c) shows the temperature evolution of the peak intensity normalised to the maximum value at 28 K and 30 mT with temperature. The FWHM of the SDW peak stays fairly constant but gets slightly broadened at low temperature (Figure.(4.6d)). The peak position ℓ_{SDW} of the SDW order shown in Figure.(4.6e) is fairly constant between 31 K and 21 K but slightly moving away from the nearest ℓ_{FM} value of -2 below 26 K.

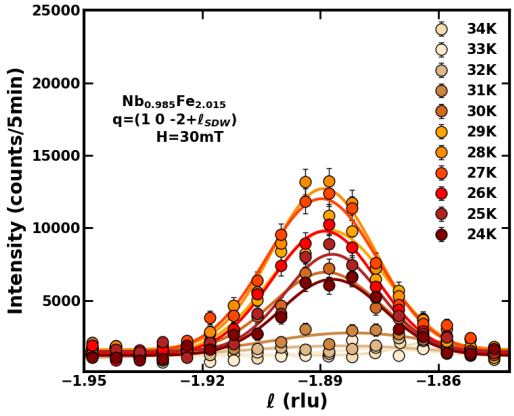

(a)

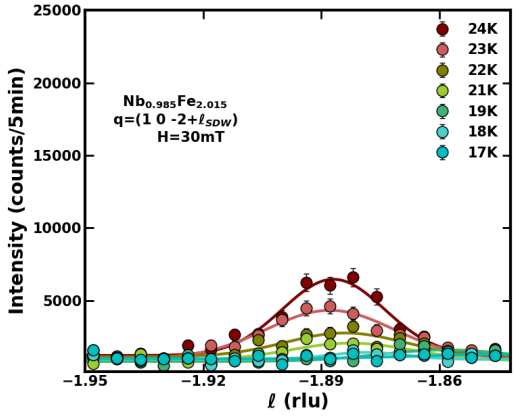

(b)

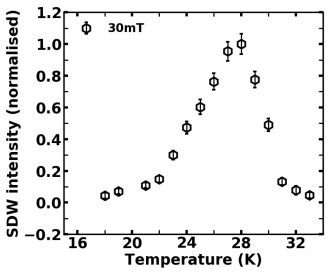

(c)

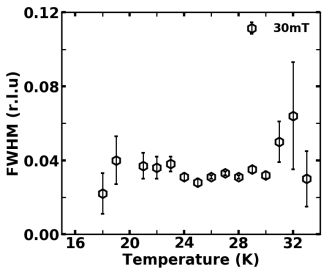

(d)

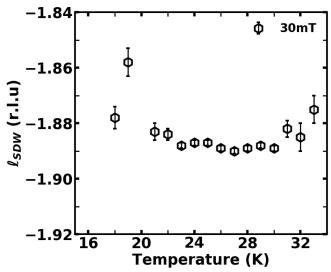

(e)

Figure 4.6: Top: (a)&(b): The temperature dependence of the SDW peak at (1 0 -2+ℓ_{SDW}) at H=30mT between 34K and 17K. The solid lines are Gaussian fits (Eq.4.2). Bottom: The SDW peak properties at different temperatures: (c) Normalised intensity, (d) FWHM (calculated using Equation.(4.3)), (e) ℓ_{SDW} value.

Figure.(4.7a) shows data obtained at H = 55 mT between 29 K and 23 K. At this increased field value we can see the SDW peak observed at field zero is almost suppressed except for the hint of a peak appearing at T $\approx$ 26 K. The absence of peak of the SDW peak except around 26 K indicates the almost complete suppression of SDW order at 55 mT. ferromagnetism is expected to form below 26 K. Figure.(4.7b) shows the normalised SDW peak intensity which is reaching a maximum at 26 K and 55 mT with temperature. The FWHM of the SDW signal has a minimum at 26 K (see Figure.(4.7c)). The peak position ℓ_{SDW} of the SDW peak shown in Figure.(4.7d) is found to shift away from the value observed at fields below 55 mT except at T $\approx$ 26 K.

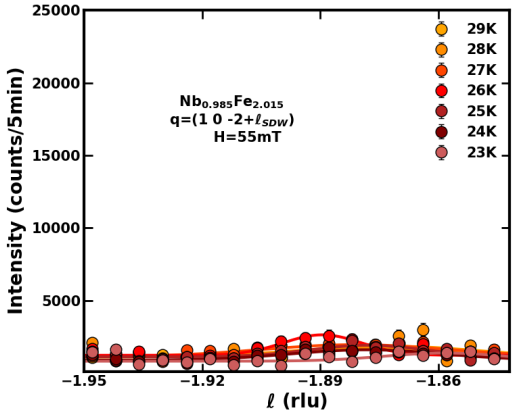

(a)

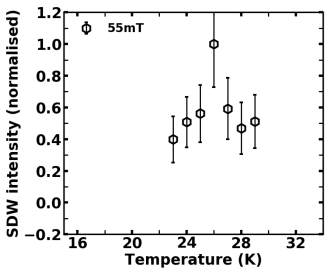

(b)

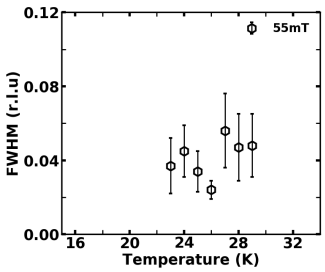

(c)

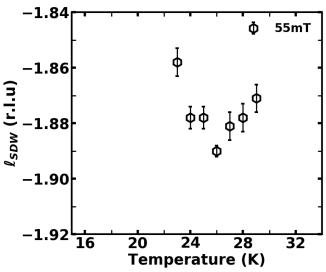

(d)

Figure 4.7: Top: (a): The temperature evolution of the SDW peak (1 0 -2+ℓ_{SDW}) at H=55mT between 34K and 17K. The solid lines are Gaussian fits (Eq.4.2). Bottom: The SDW peak properties at different temperatures: (b) Normalised intensity, (c) FWHM (calculated using Equation.(4.3)), (d) ℓ_{SDW} value.

Table.(4.2) shows T_N and T_C obtained from the analysis of the temperature evolution of the SDW peak by considering its onset and complete suppression of its peak intensity in the whole crystal respectively at different magnetic fields as described above.

Table 4.2: Field dependence of the transition temperature T_C of the full suppression of SDW order and formation of the FM order in the whole crystal and T_N of the onset of SDW order. The errors are roughly $\pm 1K$

Magnetic field (mT)	T_C (K)	T_N (K)
0	18	32
10	18	32
20	19	32
30	20	31
40	21	30
50	23	28
55	26	26

In the following, we provide the analysis of elastic scattering from the FM order to obtain the onset ferromagnetic transition temperature (T_C) at the weak nuclear Bragg reflection Q_{FM} = (1 0 2). Measurement have been done in the field range 0 - 80 mT. A selection of temperature scans of the peak intensity is shown in Figure(4.8). The FM intensities are normalised to their maximum (i.e, low temperature) values. The onset T_C's are extracted by fitting Equation(4.5)

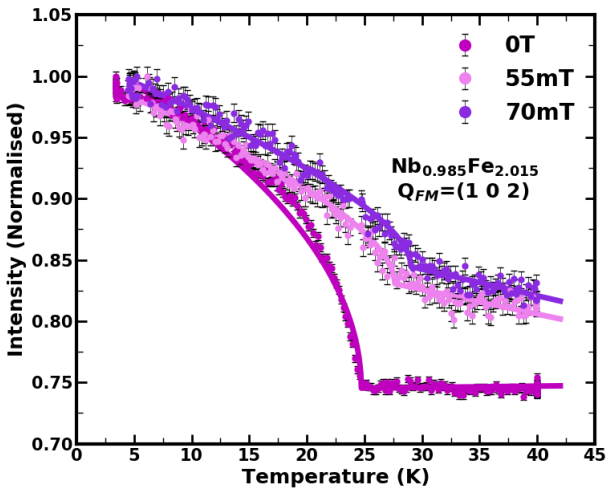

Figure 4.8: The selected temperature dependence of FM nuclear intensity (Q_{FM} = (102) $r.l.u.$) measured at different magnetic fields. The T_C onsets are obtained by fitting Eq.4.5.

The sharp feature of the ferromagnetic signal observed at zero field is smoothed out with field. Above this field the onset of FM shows a similar feature. The Curie temperature T_C extracted from the fits using Equation(4.5) is increasing with field. The T_C extracted from the fits are given in Table.(4.3)

Table 4.3: The onset Curie temperature T_C at different magnetic fields extracted from the fits using Equation.(4.5) to the temperature dependence of the peak intensities at (1 0 2).

H (mT)	0	10	20	30	40
T_C (K)	24.72(0.03)	25.43(0.10)	26.21(0.10)	26.73(0.12)	27.73(0.13)
H (mT)	50	55	60	70	80
T_C (K)	27.55(0.15)	26.63(0.15)	28.24(0.13)	28.17(0.20)	29.44(0.29)

4.3.3 Discussion

The resulting H‖c-T phase diagram for $Nb_{0.985}Fe_{2.015}$ obtained from the presented single-crystal neutron diffraction measurements is displayed in Figure.(4.9).

The phase diagram shows that with increasing field the second order (T_N) and first order (T_C) transitions shift to lower and higher temperature respectively, and merge eventually at a critical field of $H_{tr} \simeq 53$ mT and critical temperature $T_{tr} \simeq 26.5$ K. This point could be interpreted as the TCP proposed by Friedemann *et al.* based on AC susceptibility measurements [51]. The resulting phase diagram of that work (Figure(4.2)) has been confirmed in this elastic neutron scattering study by direct observation of FM and SDW order in $Nb_{0.985}Fe_{2.015}$. The observed location of the TCP agrees well with the results by Friedemann *et al.* $H_{tr} \simeq 60$ mT and $T_{tr} \simeq 28$ K for the same composition established from the AC magnetic susceptibility χ' (H, T) measurements.

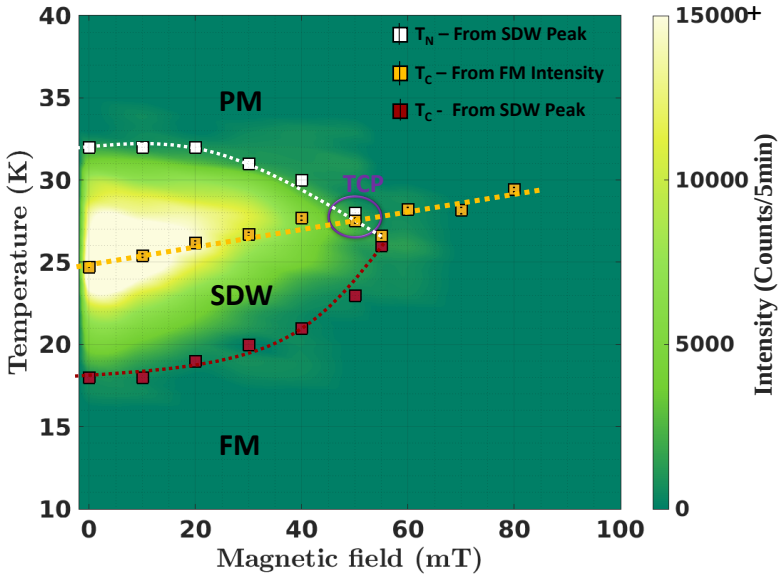

Figure 4.9: H‖c-T phase diagram of $Nb_{0.985}Fe_{2.015}$ obtained from elastic neutron scattering. The colour scale represents the neutron intensities of the SDW peaks. Squares indicate the onset T_N (white) and full suppression T_C (red) of SDW order defined as the initial appearance and full suppression of SDW peaks at (1 0 -2+ℓ_{SDW}) as well as the onset of FM order T_C (orange) defined as the appearance of an FM signal at (1 0 2). The purple circle represents the smeared out TCP ($H_{tr} \simeq 53$ mT, $T_{tr} \simeq 26.5$ K). Dashed lines are the guide to the eye.

The onset Curie temperature (T_C) obtained from the temperature scans of the FM signal suggest that the SDW peak intensity coincides with the FM onset transition temperature T_C, below which there is a temperature range in which both SDW and FM order appear to coexist. This overlap can be attributed to the distribution of transition temperatures within the sample which was observed similarly in the previous neutron diffraction measurements at zero field (see Section.(3.1.2)) [28]. The distribution of transition temperatures follows from the combined effect of small sample inhomogeneity and a strong sensitivity of the transition temperatures on the precise Nb content. A consequence is that the TCP location is somewhat smeared out.

To discuss in more detail whether a TCP has been observed we recall the expectations for the field evolution of the phase transitions from the two-order parameter Landau model (Section (4.1.1)): the SDW transition is expected to remain second order and the FM transition is initially first order but terminates in a critical point at the suspected TCP and changes into a crossover at higher field. In this study the onset T_C increases with magnetic field and even beyond the TCP. The change of the T_C signature at (1 0 2) from a fairly sharp kink below

H_{tr} to a broader feature at and above H_{tr} could be caused by the change of the order of phase transition from first order below H_{tr} to second order at H_{tr} and possible change to a crossover above H_{tr}. A proof of this is difficult, however, due to the small inhomogeneity that is present in the large neutron sample but the findings are not inconsistent with the presence of a TCP. Equally the continuous onset of the SDW order at finite field as shown in Figure.(4.6c) suggests that the SDW transition continues to be second order in field. The presence of small sample inhomogeneity prevents strong conclusions, but the reported observations are not inconsistent with the presence of a TCP.

The result can be compared with a similar H‖c-T phase diagram obtained for the more Fe-rich $Nb_{0.981}Fe_{2.019}$[1] sample [74]. The phase diagram is shown in Figure.(4.10). The phase diagram obtained from the SDW peak intensity in elastic neutron scattering measurements is qualitatively similar to the results presented here. The effect of increased Fe content is merely an increase in the transition temperatures including the temperature of the the tricritical point $T_{tr} \simeq 33$ K. Furthermore, the critical field is reduced to $H_{tr} \simeq 20$ mT.

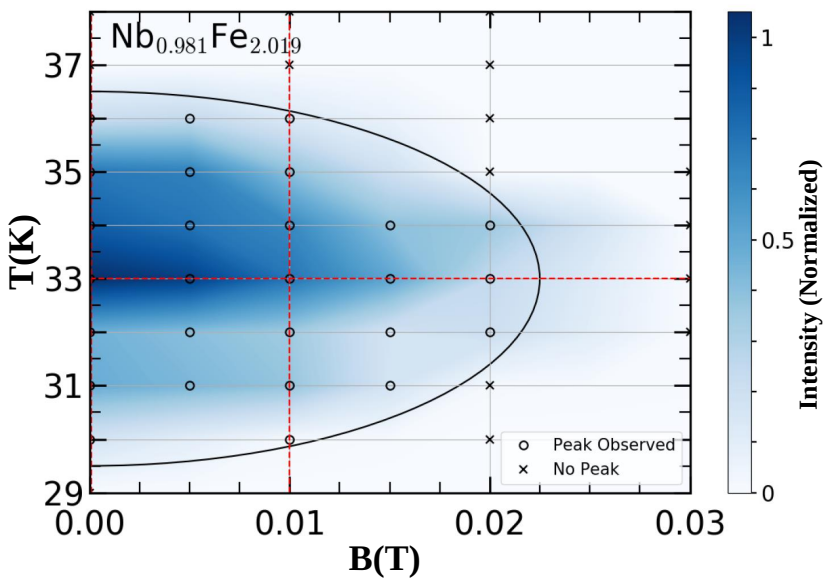

Figure 4.10: H‖c-T phase diagram of $Nb_{0.981}Fe_{2.019}$[1] single crystal obtained from elastic neutron scattering at the SDW peak position (1 0 -2-ℓ_{SDW}) [74]. Colour scale represents the neutron intensities of the SDW peaks each normalised to peak at H=0 T and T=33 K. The solid black line serves the guide to the eye to indicate the SDW phase boundary.

The phase diagram clearly shows the existence of the SDW phase between the region ≈ 30 K and 36 K, darker regions represents the strong ordering of the SDW signal. With introduction

[1]The same sample of our measurement with y later was confirmed to be 0.020

of the external magnetic field the SDW phase is suppressed completely for the field ≈ 20 mT at 33 K, beyond this field and temperature the SDW phase become undetectable and away from 33 K the critical field decreases rapidly. A rough phase boundary enclosing the existence of the SDW phase in the small parameter space between the temperature 30 K and 36 K and the field below ≃ 20 mT suggests that the existence of possible TCP point in this composition may be found at H ≃ 20 mT and at T ≃ 33 K.

Figure.(4.11) shows the composition dependence of the suspected TCP temperature and field obtained in this work and previous neutron and AC magnetic susceptibility studies [51, 74]. The combined results show a common trend for the composition dependence of the TCP location that leads to a QTCP at y ≃ -0.003 at H_{tr} ≃ 500mT [51].

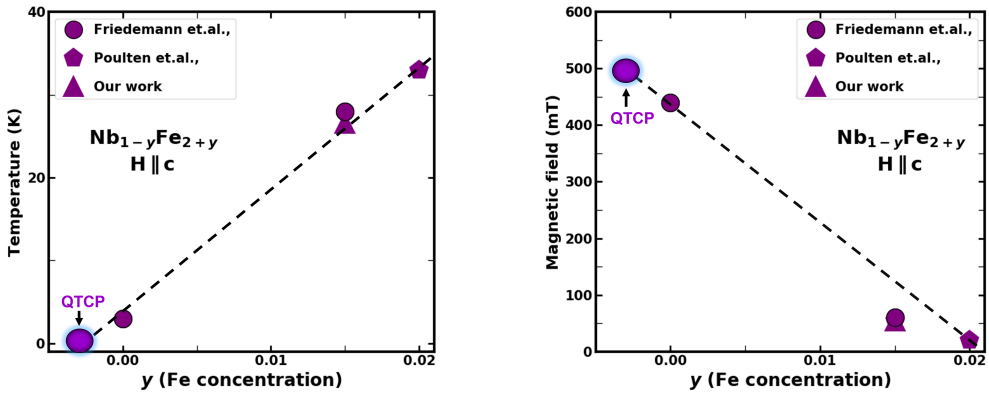

(a) (b)

Figure 4.11: Composition dependence of (a) temperature and (b) field for $Nb_{1-y}Fe_{2+y}$ series of samples obtained from ours, Paulten and Friedemann *et.al.,* [51,74]. The dashed black line are guide to the eye. Glowing purple spheres indicate the QTCP obtained from the extrapolation of TCPs by Friedemann et.al.

4.4 Phase diagram for H‖a

This section presents the H‖a-T phase diagram using neutron diffraction measurements by applying the field perpendicular to magnetic easy c axis. We have tested whether the transverse field can suppress the easy c-axis FM state and lead to a field-induced FM QCP. Similar to the previous Section.(4.3) we have investigated the SDW peak evolution and the temperature dependence of the FM signal at different fields. The neutron diffraction measurements have

been performed on high quality $Nb_{0.981}F_{2.020}$ single crystal using triple axis spectrometer 4F2 at LLB with the support of the beam scientist Dr Jean-Michel Mignot.

4.4.1 Data acquisition and correction

The single crystal with composition $Nb_{1.981}Fe_{2.020}$ has been oriented with a* and c* axes in the horizontal scattering plane. Table.4.4 summarize the instrument settings used. To eliminate the higher order neutrons Be-filters have been used. The vertical and horizontal alignments of the monocromator and analyser have been focused and flat respectively. The uniform field H||a was produced using a 6 T cryomagnet.

	4F2
Scattering Plane	a*-c*
Monochromator horizontal	Flat
Monochromator vertical	Focused
Analyser horizontal	Flat
Analyser vertical	Focused
$k_i = k_f$	1.3 $Å^{-1}$
Collimation	No
High order filter	Beryllium
Scattering mode	Elastic

Table 4.4: 4F2 experimental Settings for the neutron diffraction.

At different fields SDW order has been observed via ℓ scans across the satellite position (-1 0 -2+ℓ_{SDW}) at different temperatures. FM order has been measured via temperature scans at the weak nuclear peak position (-1 0 -2).

Due to the temperature-hysteresis of the SDW ordering wave-vector position [28, 55], we measured the evolution of the SDW peak with decreasing (1K) steps in temperature only. To determine T_C up-sweeps in T were used.

4.4.2 Neutron diffraction results and analysis

The collected data for the SDW peak evolution have first been monitor corrected to filter out the higher harmonic neutrons from the incoming neutron flux (k_i). The monitor correction are applied to the data using the experimentally determined ki dependent correction factor (see Chapter(3)).

Before presenting the results in a transverse field we look at the zero-field results. Figure.(4.12) shows the temperature evolution of the SDW peak between 40 K and 30 K. On lowering the temperature a magnetic Bragg peak starts to emerge at Q_{SDW} = (-1 0 -2+ℓ_{SDW}) at temperature $T_N \approx 38$ K. The peak is reaching a maximum at T $\approx$ 35 K and then the amplitude is reduced on further decreasing the temperature. The SDW peak gets completely suppressed below temperature T $\approx$ 32 K. The suppression of the peak is expected given the ordering of ferromagnetism below temperature T $\approx$ 32 K, observed similarly in the previous neutron diffraction measurements [28]. The SDW peak properties are extracted by using a fit function as given in Equation.(4.2). Figure.(4.12b) shows the temperature evolution of the intensity normalised to the peak at 35 K. The FWHM of the SDW peak calculated via Equation.(4.3) stays fairly constant but gets slightly broadened at low temperature shown in Figure.(4.12c). The peak position ℓ_{SDW} of the SDW ordering shown in Figure.(4.12d) is slightly moving towards the nearest ℓ_{FM} value of -2 r.l.u. with decreasing temperature.

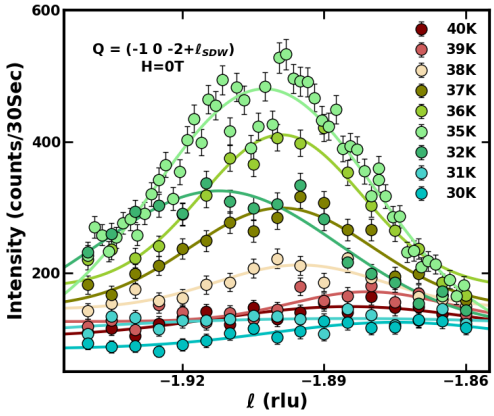

(a)

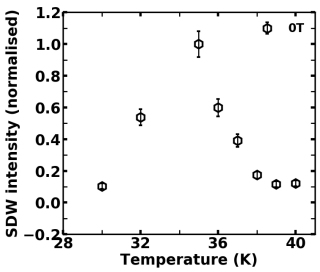

(b)

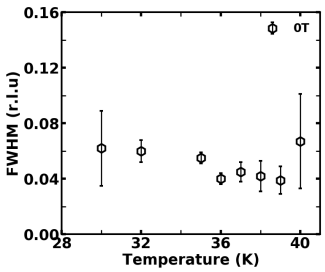

(c)

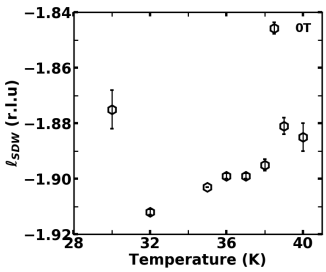

(d)

Figure 4.12: Top: (a) The temperature dependence of the SDW peak in zero magnetic field at (-1 0 -2+ℓ_{SDW}) between 40 K and 30 K. The solid lines are Gaussian fits(Equation.(4.2)) Bottom: The SDW peak properties at different temperatures; (b) Normalised intensity, (c) FWHM (calculated using Equation.(4.3)), (d) ℓ position.

In Figure.(4.13) we show the temperature evolution of the SDW peak measured at 0.5 T between 39 K and 30 K. A peak appears at T $\approx$ 35 K. The peak reaches maximum in its intensity at T $\approx$ 33 K and then is fully suppressed. The SDW peak properties extracted by fitting are shown in Figure.(4.13b) shows the temperature evolution of the intensity normalised to the maximum value at 35 K, Figure.(4.13c) shows the FWHM of the SDW peak calculated via Equation.(4.3) which stays fairly constant but gets slightly broadened at the edges of the measured temperature range. The peak position ℓ_{SDW} of the SDW ordering displayed in Figure.(4.13d), shows that the obtained values are fairly constant in the temperature range that shows significant integrated SDW peak intensity.

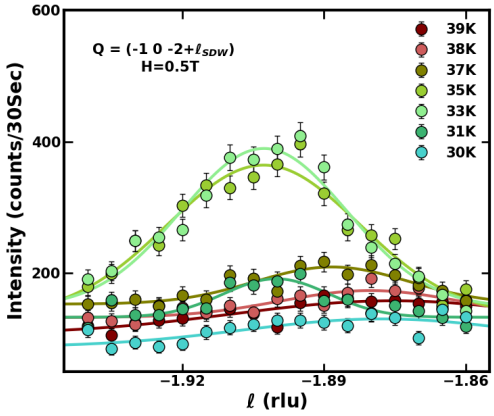

(a)

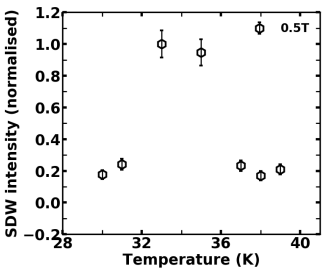

(b)

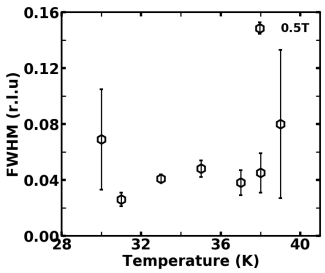

(c)

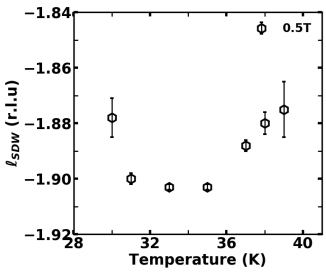

(d)

Figure 4.13: Top: (a) The temperature dependence of the SDW peak with magnetic field 0.5 T at (-1 0 -2+ℓ_{SDW}) between 39 K and 30 K. The solid lines are Gaussian fits (Equation.4.2). Bottom: The SDW peak properties at different temperatures; (b) Normalised intensity, (c) FWHM (calculated using Equation.(4.3)), (d) ℓ position.

Figure.(4.14) shows the measurements at H = 1 T range between 41 K and 29 K. We can see that at this field SDW peak is almost suppressed at field 1 T except for the very small peak at T≈ 32 K. As we did not observe the emergence of any peak signalling the onset of SDW order above the field 1 T. H = 1 T represents the transverse critical field for the suppression of SDW order. Figure.(4.14b) shows the normalised SDW peak intensity does not reveal the presence of an SDW peak. The FWHM of the SDW peaks are broadened except at temperature 32 K, see Figure.(4.14c). The ℓ_{SDW} values shown in Figure.(4.14d) are observed to shift away from the value observed at fields below 1 T except at T≈32 K.

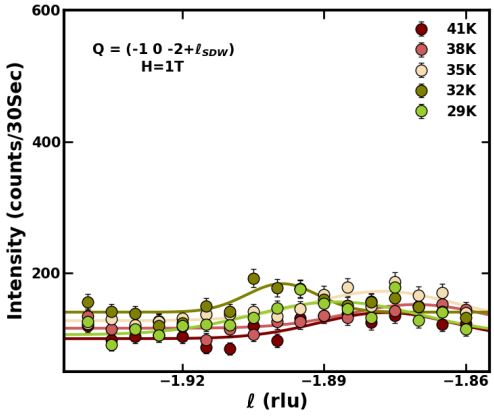

(a)

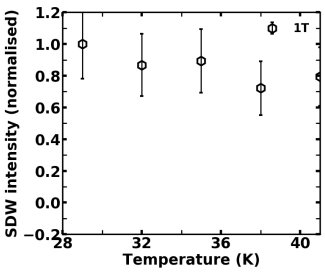

(b)

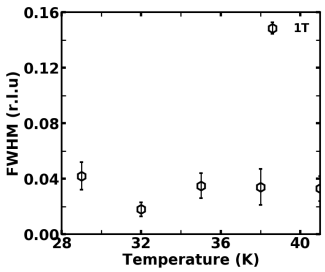

(c)

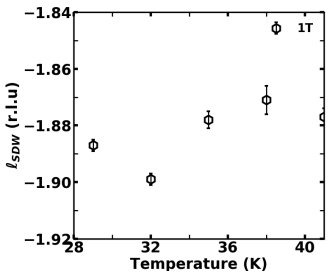

(d)

Figure 4.14: Top: (a) Temperature dependence of the SDW peak at 1 T at (-1 0 -2+ℓ_{SDW}) between 39 K and 30 K. The solid lines are Gaussian fits (Equation.(4.2)) Bottom: The SDW peak properties at different temperatures; (c) Normalised intensity, (d) FWHM (calculated using Equation.(4.3)), (e) ℓ position.

Table.(4.5) shows the temperatures T_N of the onset of SDW order and T_C of the full suppression of SDW order and formation of FM order in the whole crystal as obtained from the properties of the temperature evolution of the SDW peak at different magnetic fields (H‖a).

Table 4.5: H||a dependence of the transition temperatures T_C of the full suppression of SDW order and formation of FM order in the whole crystal and T_N of the onset of SDW order.

Magnetic field (T)	T_C (K)	T_N (K)
0	32	38
0.5	31	35
1	32	32

In the following, we will present the analysis of magnetic neutron scattering from the FM order to obtain the onset ferromagnetic transition temperature (T_C) at the Bragg reflection Q_{FM} = (-1 0 -2). Measurements have been done in the field range 0 - 2.5 T. A selection of temperature scans of the peak intensity is shown in Figure.(4.15). The intensities are normalised to the maximum value (15 K intensity of the 0T data set). The onset T_C's are extracted by fitting Equation.(4.5).

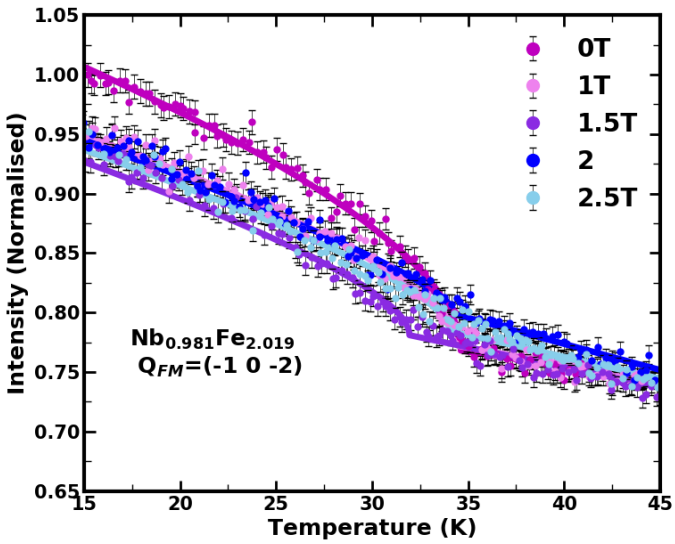

Figure 4.15: A selection of temperature scans at Q_{FM} = (-1 0 -2) measured at different magnetic fields. The T_C onsets are obtained by fitting with Equation.(4.5.)

Figure.(4.15) shows that for zero magnetic field the ferromagnetic transition is observed at $T_C \approx 38$ K as obtained similarly in various previous measurements on the same composition, demonstrating the good reproducibility of the data [28, 55, 74]. On increasing the magnetic field, the sharp feature of the ferromagnetic signal is broadened. The Curie temperatures T_C

extracted from the fits using Equation.(4.5) are given in Table.(4.6).

Table 4.6: The onset Curie temperature T_C at different magnetic fields extracted from the fits using Equation.(4.5) to the temperature dependence of the peak intensities of ferromagnetic signals.

H (T)	0	0.5	1	1.5	2	2.5
T_C (K)	34.61(0.08)	32.24(0.08)	35.53(0.12)	32.66(0.152)	34.49(0.32)	33.02(0.14)

4.4.3 Discussion

The resulting H‖a-T phase diagram from neutron diffraction measurement on $Nb_{0.980}Fe_{2.020}$ single crystal is displayed in Figure.(4.16). It can be seen that the onset second order transition temperature T_N decreases and the first order bulk FM transition temperature T_C slowly increasing with increasing magnetic field and eventually both phase transitions approaching each other close to 1 T.

The onset ferromagnetic transition temperature T_C obtained from the fits of the FM intensity (Q_{FM} = (-1 0 -2) *r.l.u.*) at different magnetic fields show that the T_C's are fairly constant within the range of the magnetic fields we measured. From our measurements we didn't see any decreasing trend of the T_C as speculated in Subsection(4.1.2) beyond the 1T, with field applied transverse to the magnetic easy axis c. The difference in T_C obtained from the SDW and FM signals suggests that there is a temperature range in which both SDW and FM orders coexist. This overlap can be attributed to the distribution of transition temperatures within the sample which is also observed similarly in the previous neutron diffraction measurements [28].

From the raw data in Figure.(4.15) one can see that the feature defining T_C is broadening and getting less pronounced with increasing field. This makes it difficult to follow the FM signal beyond 1 T. This observation could be caused by the change of the FM transition to a crossover at higher fields. As the field is perpendicular to the FM ordered moment, it is expected that the crossover region will be suppressed to lower temperatures with further increased field and that a critical field can be reached for the location of the crossover low temperatures. Therefore, the neutron data suggests that there is no field-induced QPT or unmasked FM QCP in $NbFe_2$ as otherwise a well-defined FM onset signal should have been observed down to low temperature. Whether the SDW is suppressed in a TCP as in the H‖c case will depend on where the first-order FM transition terminates in field and whether the SDW transition stays second order,

which cannot be conclusively determined with the data set presented here.

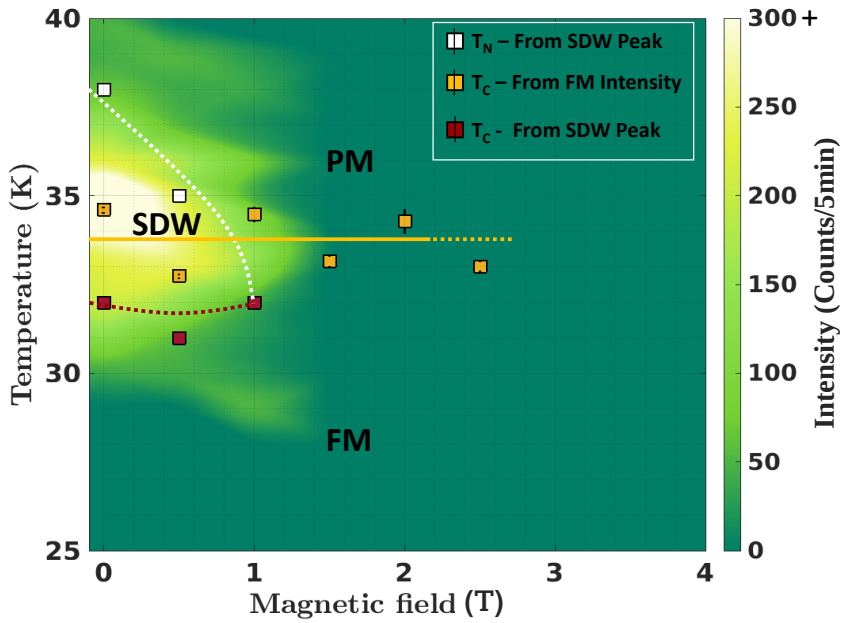

Figure 4.16: H||a-T phase diagram of $Nb_{0.980}Fe_{2.020}$ obtained from elastic neutron scattering. The colour scale represents the neutron intensities of the SDW peaks. Squares indicate the onset (white) and full suppression (red) of SDW order defined as the initial appearance and full suppression of SDW peaks at (-1 0 -2+ℓ_{SDW}) as well as the onset of FM order (orange) defined as the onset of an FM signal at (-1 0 -2) at different fields. Lines are guides to the eye.

5

Longitudinal field evolution of magnetic excitation spectrum in Fe-rich $NbFe_2$

In the previous chapter we used magnetic neutron diffraction to explore the magnetic phase diagram of the $Nb_{1-y}Fe_{2+y}$ system with magnetic field applied in different directions. Two cases has been studied: the field applied along the magnetic easy axis (H‖c) and perpendicular to it (H‖a). In the H‖c magnetic phase diagram we determined the location of Tri-Critical Point (TCP) in an Fe-rich sample. In this chapter, we investigate how the magnetic excitation spectrum evolves when approaching the field tuned TCP in the phase diagram. We perform inelastic neutron scattering experiments to investigate this evolution.

5.1 Introduction

As we have established the location of the TCP in the previous Chapter(4), in this chapter, we report the evolution of the low-energy excitation spectra in the TCP-containing $H \parallel c-T$ phase space measured using triple axis spectrometer MIRA-2 at FRM 2 with the support of the beam scientist Dr Markos Skoulatos on high quality single crystal with composition $Nb_{0.985}Fe_{2.015}$. Low energy magnetic excitations have been collected in the reciprocal space between (0 0 2) and (0 0 2.4) which also includes Q_{SDW}. The chapter is organised as follows: First, we describe the data acquisition of the unpolarised inelastic neutron scattering experiment measured in Section(5.2). Then we outline the data correction in Section.(5.3) and data analysis in Section.(5.4). Finally we will present the results and discussion in Section.(5.5) and Section.(5.6) respectively.

5.2 Data acquisition

In this section we present the data acquisition of inelastic neutron scattering experiment. We performed the inelastic neutron scattering in the constant-Q method where the energy scans are carried out by tuning the k_f and keeping $k_i = 1.55$ Å^{-1} fixed. Table.(5.1) summarize the instrument settings used for measuring the unpolarised inelastic neutron scattering. The same high quality single crystal with composition $Nb_{0.985}Fe_{2.015}$ used for establishing the TCP previously in Chapter(4) was used to collect the low energy magnetic excitations. To produce the uniform field of H‖c a 0.3 T Helmholtz coil set-up was used. The higher order neutrons from the incoming neutron flux (k_i) are eliminated using a Be-filters. The vertical and horizontal alignments of the monocromator and analyser are kept focused and flat respectively.

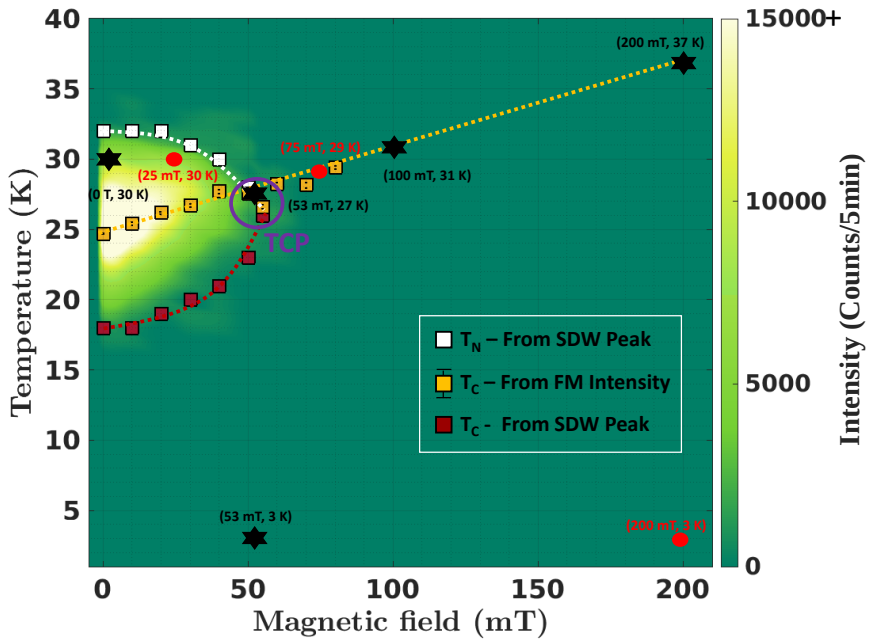

Figure 5.1: H‖c-T phase diagram of $Nb_{1-y}Fe_{2+y}$ obtained from elastic neutron scattering. The Colour scale represents the neutron intensities of the SDW peaks. Squares indicate the onset T_N (white) and and full suppression T_C (red) of SDW order defined as the initial appearance and full suppression of SDW peaks at (1 0 -2+ℓ_{SDW}) as well as the onset of FM order T_C (orange) defined as the appearance of an FM signal at (1 0 2). Purple circle represents the broadened TCP ($H_{tr} \simeq 53$ mT, $T_{tr} \simeq 26.5$ K). Dashed lines are the guide to the eye. Black stars indicate the locations in $H \parallel c - T$ phase space where measurements have been between the Q positions (0 0 2) and (0 0 2.4) and the dots indicate locations where measurements have only been done at Q_{FM} and/or Q_{SDW}.

Table 5.1: MIRA-II experimental Settings for the unpolarised inelastic neutron scattering.

	MIRA-II
Scattering Plan	*(h 0 ℓ)*
Monochromator horizontal	Flat
Monochromator vertical	Focused
Analyser horizontal	Flat
Analyser vertical	Focused
k_i	1.55 $Å^{-1}$
Collimation	No
High order filter	Beryllium

Figure.(5.1) shows $H \parallel c - T$ phase diagram obtained from the temperature dependence of the SDW satellite peak and the FM peak (Q_{FM}) intensity with different fields (H‖c) as explained in the previous chapter (see Section(4.4)). The (H‖c, T) positions where we have collected inelastic neutron scattering data are also shown in the figure. We have ensured to measure in the region of the TCP (broadened by a small amount of sample inhomogeneity), which is centred at $H_{tr} \simeq 53$ mT and $T_{tr} \simeq 26.5$ K.

5.3 Data correction

5.3.1 Higher-order monitor correction and normalisation

The inelastic neutron scattering data depending on the intensity of the signal was collected with different measurement times during the energy scans. The counting of the signals were longer at energies where the signals were weaker. The collected data have been then normalized to a unique monitor count value $N_{value} \simeq 5000$ counts before applying data fitting equating roughly to 5 min exposure time. The higher order monitor correction has not been done due to use of constant k_i and consequence that correction would only be a common scaling factor to all data of this measurement.

5.3.2 Energy shift correction

The elastic line in the MIRA-2 data is often seen to be shifted from its nominal zero energy position by an amount of the order of up to $E_s \approx 0.05$ meV. We compensated for E_s by applying corresponding corrections before fitting the data.

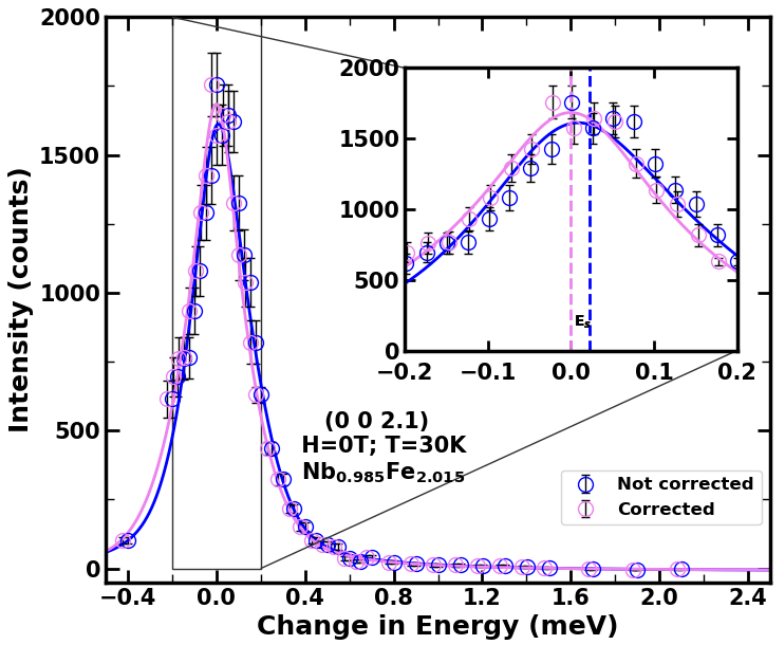

Figure 5.2: Representative illustration of the energy shift correction for the Q position (0 0 -1.8) measured at H=0 T and T=6 K during LLB-I at 4F2. The data shows the energy scan with uncorrected (blue) and corrected (violet) energy shift. The inset shows the magnified view of the elastic line with uncorrected Gaussian fit centred at E_s (blue dased line) and energy shift corrected at 0 meV (violet dashed line). The solid lines represents the Gaussian fits (Equation.(5.1))

Figure.(5.2) illustrates the energy shift in the measured data collected during MIRA-2 for the representative Q position (0 0 2.1) at $H = 0$ T and $T = 30$ K. The figure consists of energy scan with uncorrected (blue) and corrected (violet) scattering data. We obtained the energy shift (E_s) by fitting three parameter Gaussian function given in Equation.(5.1),

Gaussian function:

$$f(x) \longmapsto A\exp\Big(-\frac{(\mathrm{x}-\mathrm{b})^2}{2\sigma^2}\Big) + \mathrm{Cst}, \tag{5.1}$$

where A is the amplitude of the Gaussian peak, b is the centre of the peak, σ is the peak width

and Cst is a constant. The data was then corrected by adding the offset energy (E_s) to the energy transfer.

5.3.3 Background subtraction

In the following, we present the details of subtraction of background contribution to the inelastic signal measured from the sample to improve the quality of the signal. We collected background data at Q_b = (0.85 0 1.4) position in zero magnetic field at temperature 3 K and 30 K, far away from the region around Q_{FM} = (0 0 2) with its significant low energy excitations to investigate the temperature dependence.

After applying the monitor correction and the normalisation to the data as explained in the subsection(5.3.1) we fitted the data with a three parameter Gaussian function and a constant as given in Equation.(5.2).

$$f(x) \longmapsto A\mathrm{exp}\Big(-\frac{(\mathrm{x}-\mathrm{b})^2}{2\sigma^2}\Big) + \mathrm{cst} \tag{5.2}$$

where A is the amplitude of the Gaussian peak, b is the peak centre, σ is the peak width and cst is a constant term. The peak centre b is a fit parameter, as no correction for E_s has previously been done for the background data. Figure.(5.3) shows the background signal measured at H = 0 T at temperature T = 3 K and 30 K. By fitting the Equation.(5.2) we determined the energy at which the elastic line scattering is insignificant (where the Gaussian peak amplitude is less than 1%) as ±0.2 meV (indicated by the green dashed lines in the Figures (5.3a and 5.3b)). Figure.(5.3c) shows the temperature dependence of the constant background obtained by fitting the Equation.(5.2). From the data fit we found that the constant background has no significant dependence with the temperature therefore we used the average value of the temperature independent constant background of 5.9 ± 0.9 counts/5mins to subtract it from the normalised data. The parameters obtained by fitting the Equation.(5.2) to the background signals are given in Table.(5.2.) The values obtained for the amplitude of the background signal is found to have temperature dependence where it decreases with temperature as shown in Figure.(5.4). The rest of the Gaussian fit parameters are independent of the temperature hence we used the average of the fit parameters to subtract the background contribution.

$$f(x) \longmapsto m * x + c \tag{5.3}$$

where $f(x)$ is the linear function with slope m and constant c. The values of the fit parameters obtained from the fit for m and c are -4.8 counts/K and 766 counts/5mins respectively. Table.(5.3) shows the extrapolated values for the signal amplitude at different temperatures to subtract the background signal contribution to the inelastic neutron scattering data.

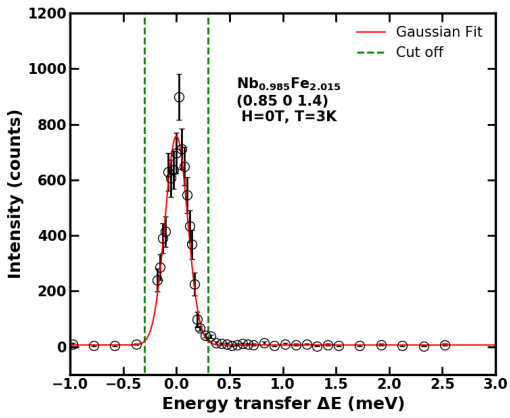

(a)

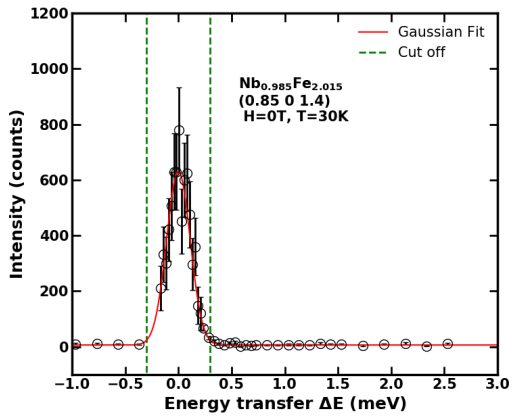

(b)

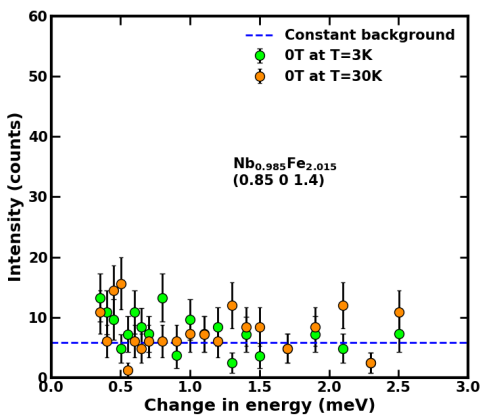

(c)

Figure 5.3: Background measurement of inelastic neutron scattering data measured at Q_b = (0.85 0 1.4) at (a) : $H = 0$ T, $T = 3$ K and (b): $H = 0$ T, $T = 30$ K. The red solid line indicates the Gaussian fit function with a constant (Equation.(5.2)), the green dashed lines represent the point above which the elastic line contribution is insignificant (± 0.2 meV). (c): The data of the constant background where the elastic line contribution is insignificant. The blue dashed line indicates the average constant background value (5.9±0.9).

To include the temperature dependence of the background in the inelastic neutron scattering data we extrapolated temperature evolution of the amplitude of the background signal using the fit parameters extracted from the linear fit function (Equation.(5.3))

Table 5.2: The fit parameters of the background measured at $H = 0$T at temperatures $T =$ 3K and 30K. The background signal is fitted using Equation.5.2.

Fit parameters	T =3 K	T=30 K
Amplitude (A)	752 ± 29	624 ± 49
Standard deviation (σ)	0.106 ± 0.003	0.111 ± 0.005
Constant (c)	5.9 ± 0.5	5.9 ± 0.6

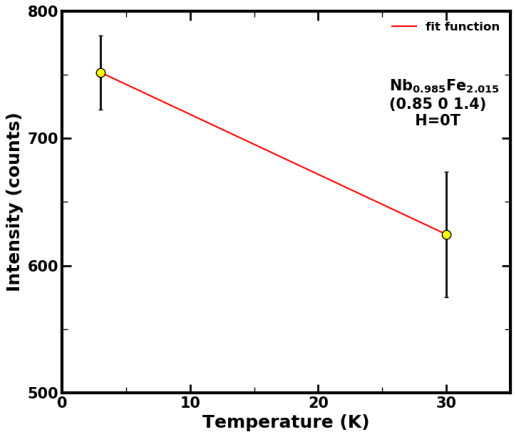

Figure 5.4: The temperature dependence of the amplitude of background signal measured at (0.85 0 1.4) at the field H=0T. The red line indicates linear fit to obtain the temperature dependence.

5.4 Data Fitting and Analysis

In this section, we will explain how we fitted MIRA-2 data after the necessary corrections applied to the raw scattering data as explained in the previous sections. To extract the physical parameters, we fitted the whole signal including the elastic line for all measured Q positions except for the Bragg position $Q_{FM} = (0\ 0\ 2)$. In this case the fits would be dominated by the large intensities of the elastic line and lead to large errors in the fit parameters describing the magnetic excitations. In such a case, we only included the tail of the elastic line up to 1% of

Table 5.3: The extrapolated amplitude of the background signal for different temperatures. The values are calculated using Equation.5.3.

Temperature (K)	Peak amplitude (Counts)
3	752
27	639
29	629
30	623
31	620
37	591

its maximum value in the fitted data.

5.4.1 Fit functions

To investigate the evolution of the magnetic excitations, the corrected data measured at different magnetic fields and temperatures were fitted using a damped harmonic oscillator model for the imaginary part of the dynamical susceptibility. This has been motivated by the prediction of over-damped harmonic oscillator behaviour in spin-fluctuation theory (see Chapter(1)) [39]. We used three-parameters damped harmonic oscillator function (DHO) or two-parameters over-damped harmonic oscillator function (ODHO) to fit the inelastic data [39, 55, 74].

The DHO function:

$$f_{DHO}(E) = \frac{E\chi_0 D E_0^2}{(E^2 - E_0^2)^2 + E^2 D^2}, \tag{5.4}$$

where E is the neutron energy loss (in meV), χ_0 is the static susceptibility or resonance amplitude (in counts), D is the damping factor (in meV), E_0 is the resonance energy (in meV). Additionally, one can define $\Gamma := E_0^2/D$ which can be interpreted as the quasielastic linewidth in the overdamped regime (see below).

Many E scans have been fitted well using the DHO function due to the presence of a distinct inelastic peak away from the elastic signal. However, there are scans where it is difficult to identify a distinct inelastic peak. These scans occur when the magnetic excitations are either very soft or overall rather weak. We used the ODHO function in those situations to fit the data instead, given in Equation.(5.5).

$$f_{ODHO}(E) = \frac{E\chi_0\Gamma}{E^2 + \Gamma^2}, \tag{5.5}$$

where Γ is the line width (in meV) [39].

5.4.2 Detailed balance

To account for detailed balance (see Chapter(3)) this has also been included via the factor in Equation.(5.6) [62].

$$f_{db(E,T)} = \frac{1}{|1 - \exp(\frac{-\mathrm{E}}{\mathrm{k_B T}})|} \tag{5.6}$$

5.4.3 Representative examples of the fits

Figure.(5.5) shows the representative examples of the plots fitted with DHO functions to the data measured at MIRA-2 for Q_{FM} = (0 0 2) position measured at H = 53 mT, T = 3 K (Figure.(5.5a)) and H = 0 T, T = 30 K (Figure.(5.5b)). In the damped regime (H = 53 mT, T = 3 K), the magnetic excitations form a distinct peak away from the elastic line approximately at 0.5 meV (see Figure.(5.5a)), in the overdamped regime the signal becomes quasi elastic where the features of the magnetic excitations are hard to distinguish from the elastic line (see Figure.5.5b)). Fits at the ferromagnetic ordering wave vector Q_{FM} = (0 0 2) are obtained by excluding the counts above 1% of the maximum elastic line intensity. Due to the instrument's finite resolution ellipsoids the detected signals are often composed of two Gaussian peaks at the elastic line for the Q positions measured at MIRA-2. In those cases, to fit the whole signal we used two Gaussian functions to fit the elastic line along with the functions of detailed balance and DHO or ODHO for the inelastic part of the signal.

Figure.(5.6) shows the representative examples of two Gaussian peaks observed at the elastic line for selected Q positions scanned at the elastic line for the Q position (0 0 2.05). The fit function used for fitting the whole signal with two Gaussian peaks is given in Equation.(5.7).

$$f_{fit}(E) = f_{DHO/ODHO}(E)Db(E) + A_1\exp\Big(-\frac{(\mathrm{E}-\mathrm{b}_1)^2}{2\sigma_1^2}\Big) + A_2\exp\Big(-\frac{(\mathrm{E}-\mathrm{b}_2)^2}{2\sigma_2^2}\Big) \tag{5.7}$$

where A_1 and A_2 are the amplitudes of the Gaussian peak 1 and 2, σ_1 and σ_1 are the peak widths and b_1 and b_2 are the Gaussian peak centres.

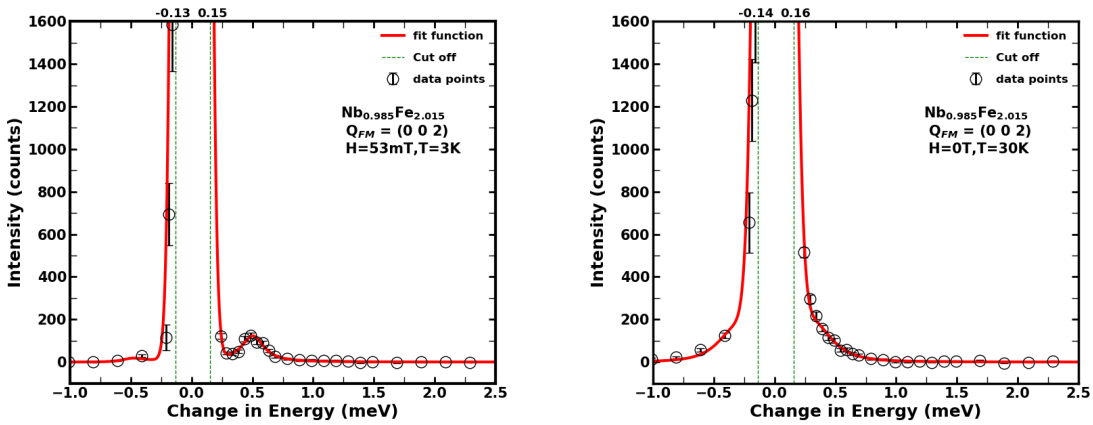

(a) (b)

Figure 5.5: Representative plots of the data fitted with DHO function at different regime. (a) Data measured at $H = 53$ mT, $T = 3$K (b) Data measured at $H = 0$ T, $T = 30$ K. The solid line (red) is the DHO fit function. The vertical green dashed lines delimit the energy range including the maximum of the elastic line that was excluded from the whole signal fit.

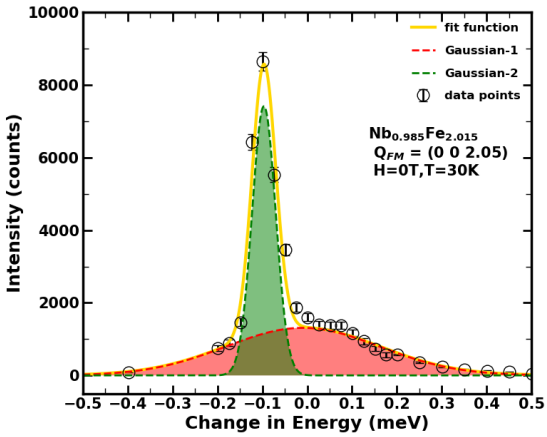

Figure 5.6: Representative plot of two Gaussian functions fitted to elastic line of the Q position (0 0 2.05) measured at $H = 0$ T, $T = 30$ K. The solid yellow line represents the whole fit function including the elastic and inelastic line using Equation.(5.7) (f_{DHO} is used for fitting the inelastic part). The green and red shaded area and the dashed lines represent de-convoluted Gaussian functions composed of the elastic line data.

5.5 Results

In this section, we report the results obtained across key areas of the H‖c-T phase diagram (see Figure.(5.1)). The focus has been on the evolution of the low energy magnetic excitations.

Figure.(5.7) shows the plots for different ℓ positions measured across Q_{FM} at various (H, T) points in the phase diagram, they are as follows, Figure.(5.7a) very close to SDW-PM transition, Figure.(5.7b) at the TCP ($H = 53$ mT and $T = 27$ K), and Figure.(5.7c) and Figure.(5.7d) are measured at FM-PM transitions. All the excitation spectra measured at various points in the phase diagram across Q_{FM} are dominated by quasielastic scattering. The observations close to the SDW-PM transition are similar to earlier studies of $Nb_{1-y}Fe_{2+y}$ [55, 74]. In the points (H, T) above the TCP, there is a FM-PM crossover while the SDW phase is completely suppressed at field $H = 53$ mT and temperature $T = 26.5$ K as it was shown in Chapter(4).

The plots in the Figure.(5.7) shows the whole signal fitted with DHO model using the Equation.(5.7) except the $Q_{FM} = (0\ 0\ 2)$ position where we only included the tail of the elastic line (up to 1% of the maximum elastic line amplitude). For the Q position (0 0 2.3) far away from Q_{FM}, the intensity of the elastic line shows a substantial drop.

The fit parameters extracted by fitting the DHO model (Equation.(5.7)) to the magnetic excitations of the Q positions (0 0 ℓ) are shown in Figure.(5.8) and Figure.(5.9). Figure.(5.8) shows the ℓ dependence of the fit parameters χ_0 and Γ, and Figure.(5.9) shows the ℓ dependence of the fit parameters D and E_0.

For H= 0 T and T = 30 K (Figure.(5.8a)), the χ_0 has a maximum at $\ell = 2.15$ r.l.u. and Γ has a minimum at the same position of $\Gamma \approx 0.115 \pm 0.011$ meV. The obtained value for Γ is found to be close to the resolution of the instrument. Due to the closeness of the reported Γ value to the instrumental resolution the value can only be interpreted as an upper bound of the true value of Γ. The ℓ dependence of the fit parameters at TCP (H=53mT, T=27K, see Figure.(5.8b)) shows that χ_0 has a maximum and Γ has a minimum ($\Gamma \approx 0.140 \pm 0.009$ meV, value close to the instrumental resolution, due to the closeness of the reported Γ value to the instrumental resolution the value can only be interpreted as an upper bound of the true value of Γ) at $\ell = 2.15$ r.l.u., similar to the result at H = 0 T at the SDW-PM phase transition. However, here, at the TCP, there is an additional local maximum in the ℓ dependence of χ_0 at $\ell_{FM} = 2$. Also, Γ increases much less towards ℓ_{FM} than in the case of H = 0 T at the SDW-PM transition. For the measurements at FM-PM phase transitions above the TCP, the

ℓ dependence of the χ_0 and Γ behaviour is qualitatively similar to the findings at the TCP for H=100 mT, T=31 K (Figure.(5.8c)), and the H=0 T result for the H=200mT, T=37 K (Figure.(5.8d), showing a maximum for χ_0 and Γ a minimum with value $\Gamma \approx 0.152 \pm 0.026$ meV, also the value is found to be close to the instrument resolution and due to the closeness of the reported Γ value to the instrumental resolution the value can only be interpreted as an upper bound of the true value of Γ.

The ℓ dependence of the fit parameters D and E_0 (Figure.(5.9)) shows that for all the measurements, D increases while E_0 stays fairly constant up to $\ell = 2.15$ r.l.u, before increasing as well.

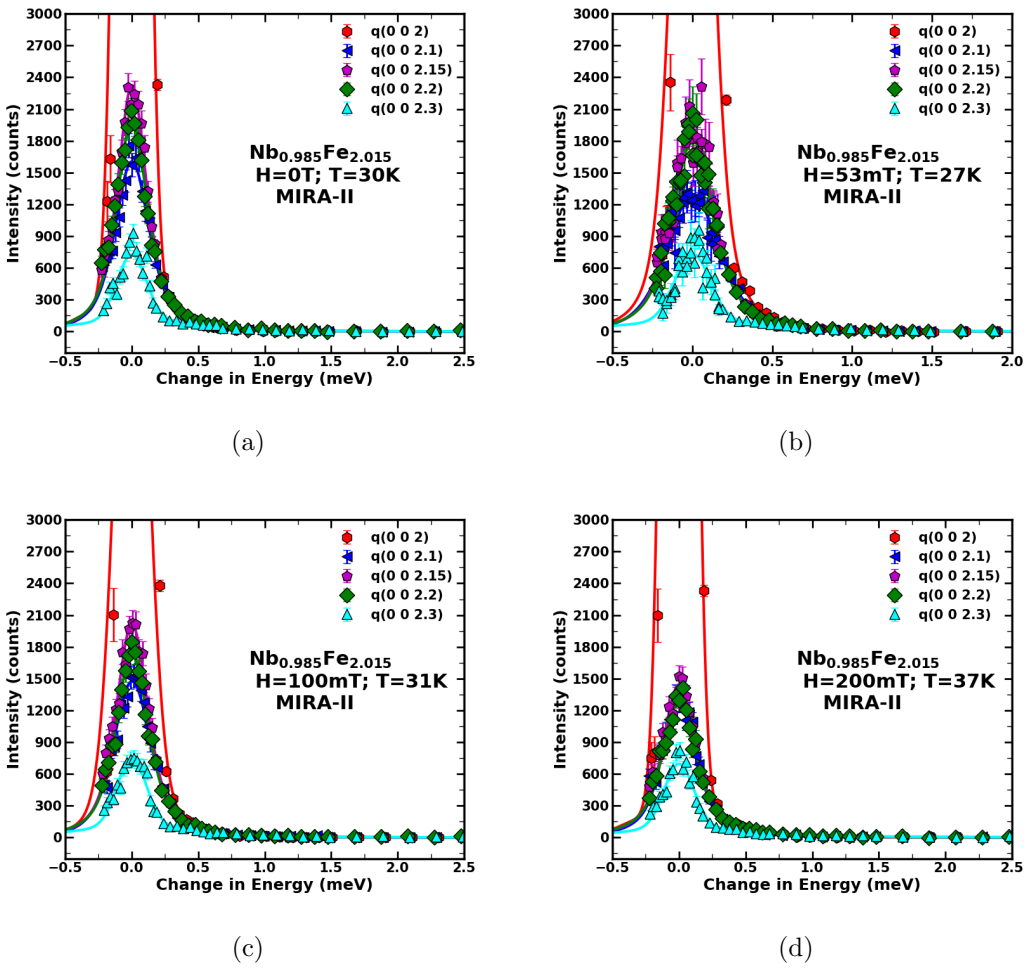

Figure 5.7: Representative plots of the magnetic excitations measured across Q_{FM} in the ℓ direction (a) H = 0 T, T = 30 K , (b) H = 53 mT, T = 27 K , (c) H = 100 mT, T = 31 K and (d) H = 200 mT, T = 37 K. The magnetic excitations are background corrected and fitted (solid lines) with DHO function.

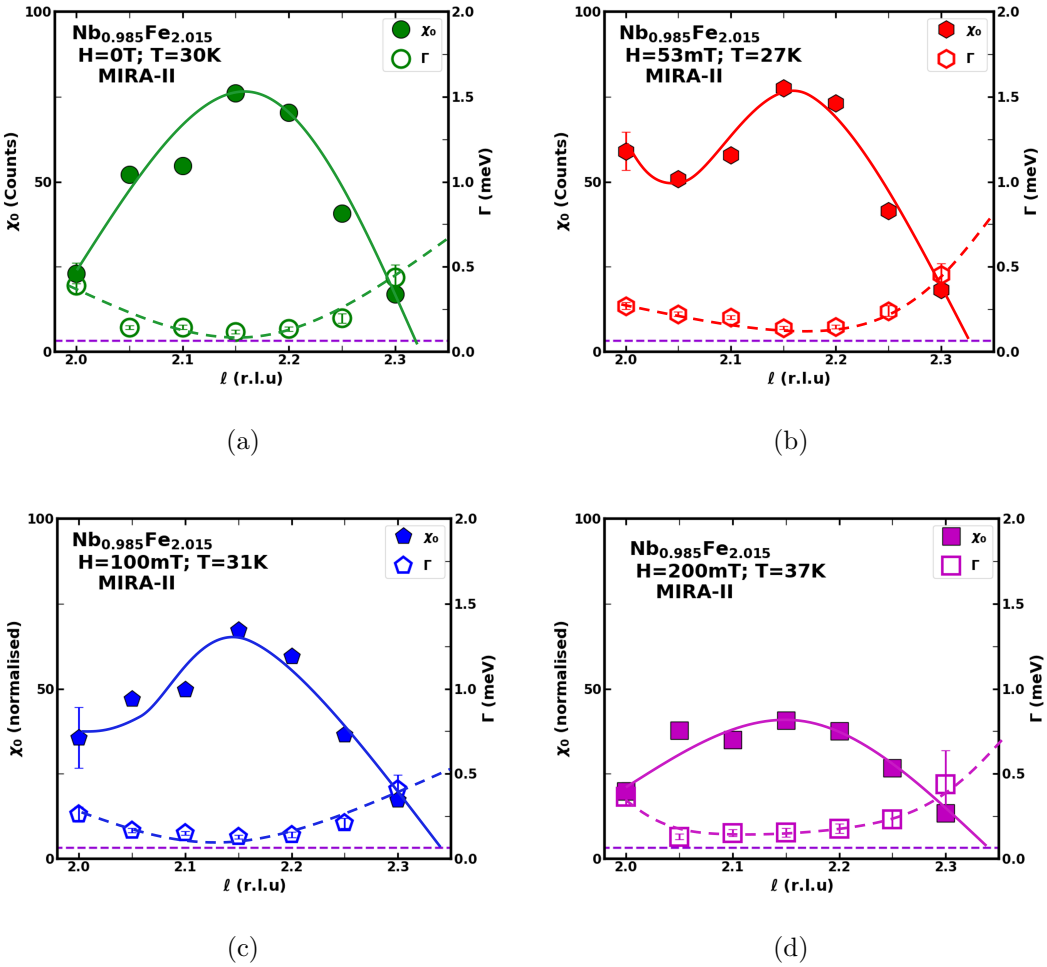

Figure 5.8: ℓ dependence of the fit parameters resonance amplitude (χ_0) and Gamma (Γ) extracted by fitting DHO function to the magnetic excitations measured across Q_{FM} = (0 0 2) at (a) H = 0 T, T = 30 K , (b) H = 53 mT, T = 27 K, (c) H = 100 mT, T = 31 K and (d) H = 200 mT, T = 37 K. Lines are guides to the eye. Purple dashed line represents the MIRA-II instrument resolution (0.064 meV).

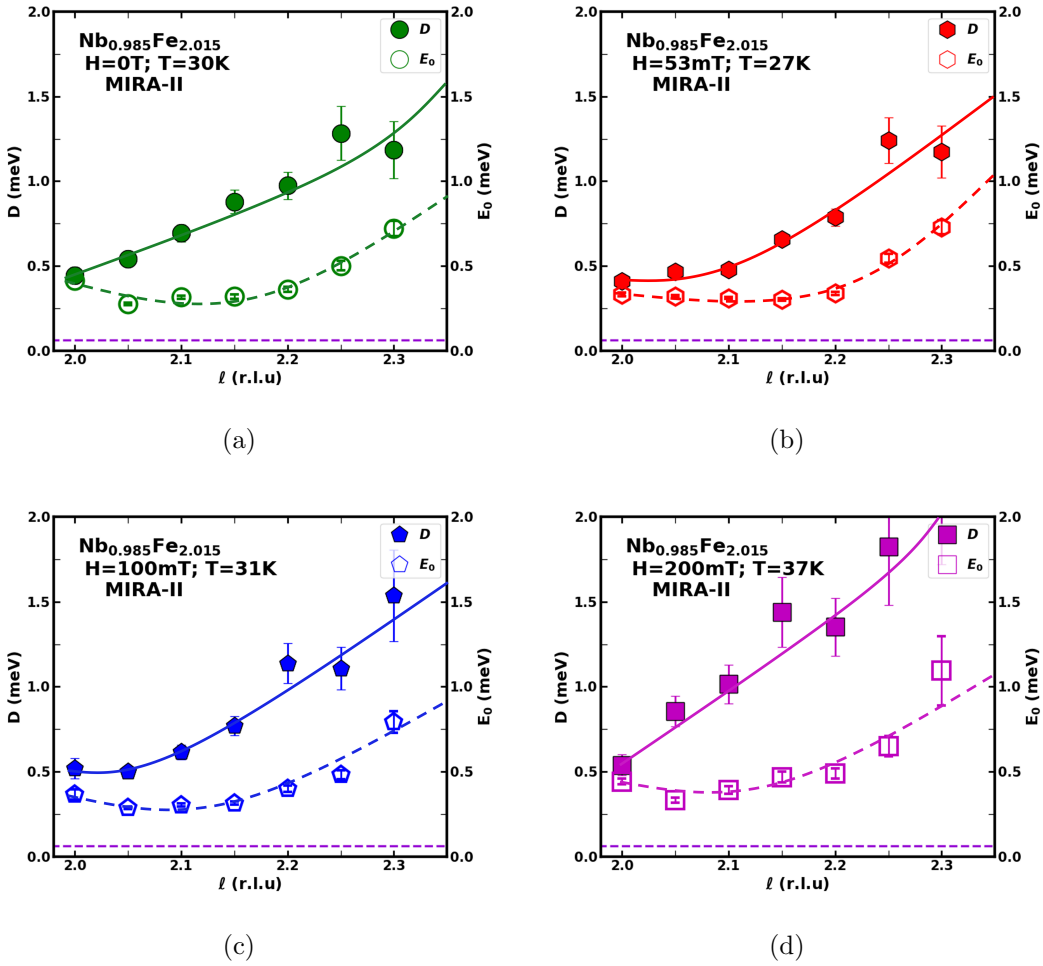

Figure 5.9: ℓ dependence of the fit parameters damping factor (D) and resonance energy (E_0) extracted by fitting DHO function to the magnetic excitations measured across Q_{FM} = (0 0 2) at (a) H = 0 T, T = 30 K , (b) H = 53 mT, T = 27 K, (c) H = 100 mT, T = 31 K and (d) H = 200 mT, T = 37 K. Lines are guides to the eye. Purple horizontal dashed line represents the instrument resolution (0.064 meV) of MIRA-II.

5.5.1 l dependence of the magnetic excitations at low temperature and at critical field (H_{tr} = 53 mT)

The low energy magnetic excitations at H_{tr} but at low temperature well below the TCP are shown in the Figure.(5.10). The magnetic excitations have been fitted with DHO model using the Equation.(5.7). A distinct inelastic peak for the magnetic excitations can be observed for the Q_{FM} position (red curve) at $\approx$ 0.5 meV, while on moving away from the Q_{FM} position the peak becomes less pronounced.

The ℓ dependence of the fit parameters extracted are shown in the Figure.(5.11). The resonance amplitude (χ_0) and Γ are is shown Figure.(5.11a). χ_0 has a maximum and Γ a minimum at $\ell = 2.15$ r.l.u. However, additionally, χ_0 has a local maximum at $\ell = 2$. The ℓ dependence of the fit parameter resonance energy and damping parameter is shown in Figure.(5.11b). The damping factor slowly increases with increases in the ℓ where as the resonance energy appears to show a shallow minimum at $\ell = 2.15$ r.l.u.

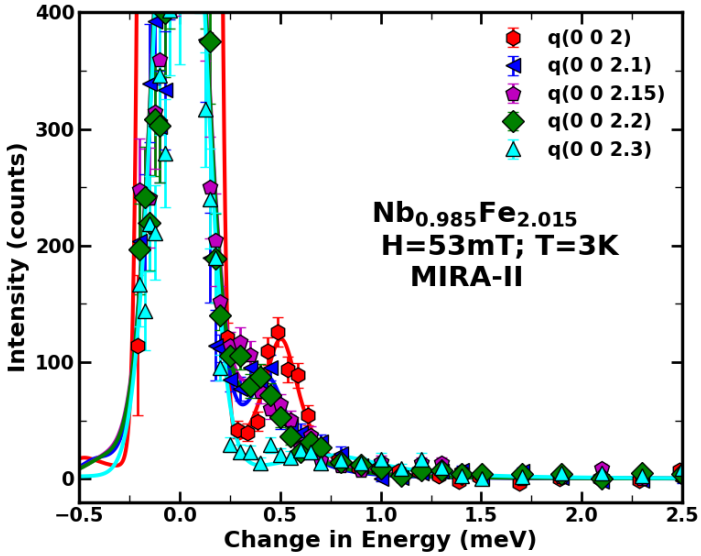

Figure 5.10: Representative plots of the magnetic excitations measured across Q_{FM} in the ℓ direction at field $H = 53$ mT, $T = 3$ K. The magnetic excitations are background corrected and fitted (solid lines) with DHO function.

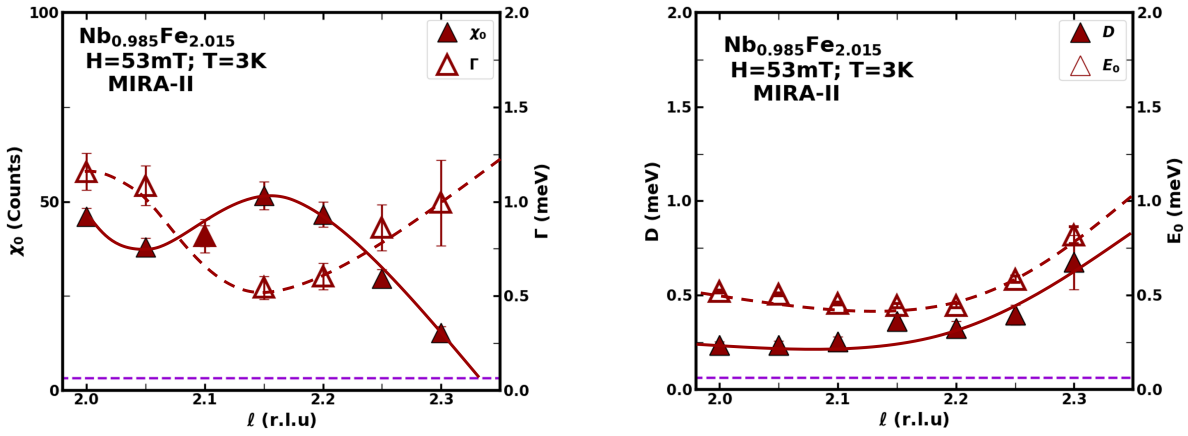

(a) (b)

Figure 5.11: ℓ dependence of the fit parameters extracted by fitting DHO function to the magnetic excitations measured across Q_{FM} = (0 0 2) at H = 53 mT, T = 3 K. (a) Resonance amplitude (χ_0) (normalised with the value measured at Q_{FM} = (0 0 2) r.l.u) and Gamma (Γ). (b) Damping factor (D) and resonance energy (E_0). Lines are guides to the eye. Purple horizontal dashed line represents the instrument resolution (0.064 meV) of MIRA-II.

5.6 Discussion

In the Section(5.5) we presented the evolution of low energy magnetic excitations measured at various points in the H‖c-T phase diagram (see Figure.(5.1)) and their analysis with the DHO model.

Earlier inelastic neutron scattering experiments on Fe-rich $Nb_{1-y}Fe_{2+y}$ within the ferromagnetic regime at zero field showed that the magnetic excitation spectra are dominated by weakly damped excitations with an excitation energy of ≈ 0.5 meV. Surprisingly, an unusual dispersion has been observed at low temperatures deep in the ferromagnetic phase: both Γ and E_0 show minima away from Q_{FM} at $\ell \approx$ 2.15 - 2.2 and maxima in χ_0 are located in this area. This suggests that SDW fluctuations play an important role even away from the SDW phase. In the measurements presented here at H_{tr} = 53 mT at 3 K this trend seems to be continued: χ_0 and Γ continue to show a maximum and minimum, respectively, away from Q_{FM} at ℓ = 2.15 r.l.u, so the SDW spin fluctuations that dominate at zero field in the FM phase survive the small applied field.

The measurements presented here near the SDW-PM transition at $H = 0$ T are in reasonable

agreement with previous results. χ_0 shows a clear maximum at $\ell = 2.15$ r.l.u. and Γ values between $\ell = 2$ r.l.u. and $\ell = 2.2$ r.l.u. are small. One small difference is that Γ actually has a minimum at $\ell = 2.15$ r.l.u., which was not clearly observed in previous studies. We note that the result presented here is qualitatively expected at a second-order SDW-PM transition. The results near at the TCP shown here are similar. The main change to the $H = 0$ T case is the addition of a local maximum in χ_0 at Q_{FM} and the simultaneous suppression of Γ there. The expected behaviour at the TCP are a diverging χ_0 and $\Gamma = 0$ at both Q_{FM} and Q_{SDW}, so two types of critical fluctuations. The difference between this expectation and the observations could be due to instrumental resolution as well as slight sample inhomogeneity that leads to a smearing out of the TCP.

For the SDW-PM phase transition earlier neutron scattering measurements at H=0 T [55,74] found the following characteristics: a trend for a χ_0 maximum at $\ell \approx 2.15$ - 2.2 as well as broad minimum of Γ reaching from $\ell \approx 1.8$ to 2.2 r.l.u. with values of $\Gamma < 0.5$ meV.

The magnetic field evolution of the Γ and static susceptibility of Q_{FM} and Q_{SDW} obtained from the quasi elastic scattering measured at SDW-PM transition, TCP, and FM-PM crossover are displayed in Figure.(5.12). Here, Q_{SDW} is defined as $\ell = 2.15$ r.l.u. We note that the observed ℓ_{SDW} for this sample is ≈ 0.1 r.l.u. However, it is plausible to assume that the location of extrema in χ_0 and Γ point to the intrinsic SDW ordering wave vector component and that the observed smaller ℓ_{SDW} values reflect the additional influence of FM interactions.

From the Figure.(5.12a), it can be seen that χ_0 for Q_{SDW} stays fairly constant with maximum value which is greater than the χ_0 obtained for Q_{FM} until the TCP (H_{tr}=53 mT, T=26.5 K) and then decreases in higher fields. χ_0 for Q_{FM} on the other hand show maximum around the TCP.

The evolution of the Γ with magnetic field displayed in Figure.(5.12b) shows that for Q_{FM} it exhibits a minimum near TCP. Surprisingly, the field evolution of Γ for Q_{SDW} on the other hand is fairly constant with value $\approx 0.13 \pm 0.01$ meV close to the instrument resolution (Due to the closeness of the reported Γ value to the instrumental resolution the value can only be interpreted as an upper bound of the true value of Γ). Although the static susceptibility point towards that the fluctuations are likely critical for both wave vectors at TCP, but the evolution of the Γ beyond TCP observed suggests the transitions may be a crossover with field.

Let's consider which evolution of χ_0 and Γ would be expected (taking into account the finite instrumental resolution). Along the SDW-PM transition line χ_0 at Q_{SDW} should be

constant and larger than χ_0 at Q_{FM}. The latter should catch up at the TCP. Along the FM-PM crossover region both should fall towards higher fields but χ_0 at Q_{SDW} more so than at Q_{FM}. Γ at Q_{SDW} should be zero within the instrumental resolution along the SDW-PM transition and up to the TCP and should then rise along the FM-PM crossover. Γ at Q_{FM} should be finite at the SDW-PM transition and fall to zero within the instrumental resolution at the TCP. It should then rise again along the FM-PM crossover but slower than Gamma at Q_{SDW}.

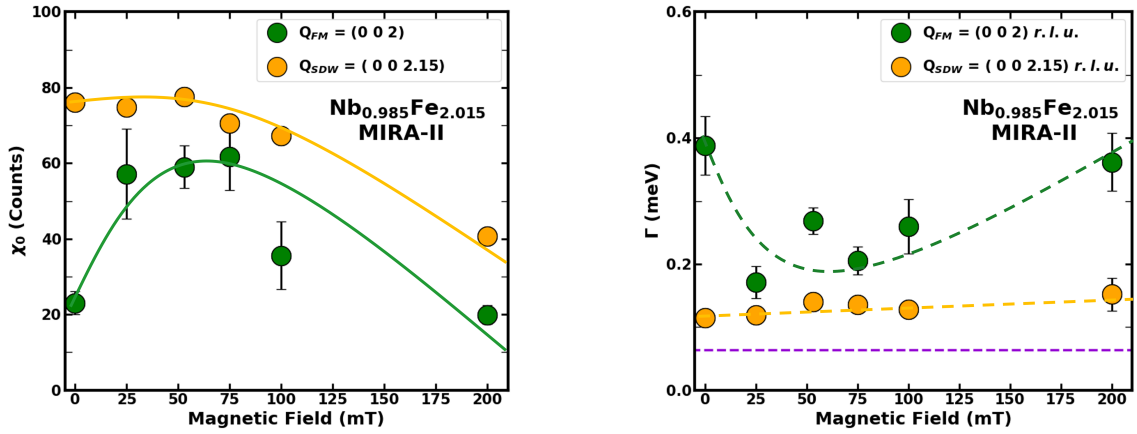

(a) (b)

Figure 5.12: The magnetic field dependence of fit parameters (a) Resonance amplitude (χ_0) and (b) Gamma (Γ) obtained by fitting the DHO model for the low energy magnetic excitations of the $Nb_{0.985}Fe_{2.015}$ system measured at the positions Q_{FM} and Q_{SDW}. The solid and dashed lines are guides to the eye. Purple horizontal dashed line represents the instrument resolution (0.064 meV) of MIRA-II.

Comparing this to the observations shown in Figure.(5.12) shows that there is broad qualitative agreement except for the the SDW spin fluctuations along the FM-PM crossover that stay more enhanced and softer than expected. This is not understood but mirrors the observation deep in the FM state that the system's proximity to SDW order is noticeable far away in the phase diagram from this ordered state.

6

Transverse field evolution of magnetic excitation spectrum in Fe-rich $NbFe_2$

In Chapter(5) we investigated the evolution of the magnetic excitation spectrum during longitudinal magnetic field tuning. From previous neutron scattering studies, the y and T dependence of magnetic excitation spectrum reflects the system's proximity to the ferromagnetic (FM) and spin density wave (SDW) phases [28]. In Chapter(4) we observed that in the magnetic phase diagram for H||a the ferro magnetic signals beyond 1 T is difficult to follow which might suggest that the phase transition PM-FM turns into a cross over. In this chapter we investigate the evolution of the magnetic excitation spectrum during and beyond suppression of the SDW order by transverse magnetic field tuning.

6.1 Introduction

We measured the transverse field evolution of magnetic excitations using the unpolarised inelastic neutron scattering method in $Nb_{0.981}Fe_{2.020}$ sample with cold neutron multi disk-chopper spectrometer (MCS)- LET (ISIS, UK) and triple axis spectrometer (TAS) - 4F2 (LLB, France). The experiments are performed with the support of the beam scientist Dr Robert Bewley and Dr David Voneshen at ISIS, UK for the LET project and Dr Jean-Michel Mignot at LLB, France for the 4F2 projects. With LET the data are measured with three different E_i's in an extended region of (Q, ω) space simultaneously for different magnetic fields. At 4F2 we collected additional data in a selected (Q, ω) range during two beamtimes "LLB-I" and "LLB-II". The remainder of the this chapter is organised as follows: first we present the data acquisition and correction of the data measured at both LET and 4F2 in Sections.(6.2 and 6.3). The fitting and analysis is presented in Section.(6.4). The analysed results are presented in Section.(6.5).

Finally we discuss our results in Section.(6.6).

6.2 Data acquisition

In this section we present the details on the data acquisition practised during the experiment. We start with the LET followed by the 4F2 instrument. To measure the magnetic excitations with LET, the E_i's we used are: E_i=1.94 meV, E_i = 3.16 meV, E_i = 6.03 meV. Figure.(6.1) shows the resolution and the range of energy transfers we could cover for the E_i's. It can be seen that the higher the energy resolution the smaller is the energy window. A good compromise between the accessible E range and the resolution was found for E_i = 3.16 meV space and therefore we focus here on the E_i = 3.16 meV data. To investigate the field evolution of magnetic excitation spectrum we collected data at H = 0 T, 2.75 T, 3.5 T and 4.25 T at temperature T = 2 K. To study the temperature dependence of the magnetic excitations at 3.5 T we measured data additionally at H = 3.5 T and T = 37.4 K.

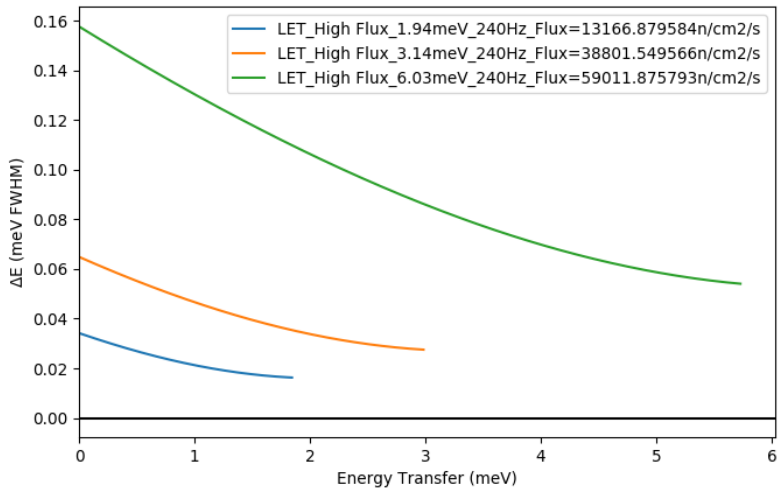

Figure 6.1: LET resolution and the range of the energy transfers for different E_i's used during the experiment provided by the instrument software. The legend indicates the information on the flux of the incoming neutron beam for the E_i's used.

To visualize and analyse the selected portion of the scattering data in (Q, ω) space lower dimensional cuts are used. At 4F2, measurements were made using vertically and horizontally focused monochromator and analyser in constant Q mode. The final wave vector k_f[1] was fixed at the value of 1.3 Å^{-1}. The scattering data were collected at different magnetic fields between

[1]The final neutron energy (E_f) equivalent of k_f = 1.3 Å^{-1} is 3.50 meV.

the range $H = 0$ T and 5 T at temperature $T = 4$ K and 1.6 K for the LLB-I and LLB-II respectively.

6.3 Data Correction

6.3.1 LET

6.3.1.1 Background Analysis

In this section we will outline the processing of the raw scattering data collected with LET. The background scattering data has been collected with a measurement of the empty sample holder at $H = 0$ T and $T = 150$ K and otherwise identical conditions as for the sample measurements, to subtract it from the raw scattering data.

Figure.(6.2) shows the 2D cuts created from S(Q, ω) of the background scattering measured with $E_i = 3.16$ meV. The bin widths used for 1D and 2D cuts of the (Q, ω) space are given in Table.(6.1). To get an overview of the elastic and inelastic background data, energy integration over the ranges [-0.2,0.2] meV (Figure.(6.2a)) and [0.2,4] meV (Figure.(6.2b)) was done, respectively.

Table 6.1: Bin widths for the low dimensional cuts from S(Q,ω) scattering data.

Bin width	2D	1D cut
ℓ	0.03 r.l.u	0.09 r.l.u
h	0.01 r.l.u	0.03 r.l.u
η	0.2 r.l.u	0.2 r.l.u
dE	0.3 meV	0.09 meV

Figure.(6.2c) shows the background signal in a section of the $\ell - E$ plane where important sample signals have been observed, too (see below). From Figure.(6.2c) we identified two strong intensities along the ℓ direction ranges from (0 0 -2.3) to (0 0 -2.1) and (0 0 -2.05) to (0 0 -1.7) at energies close to 0.5 meV and 2.5 meV respectively. We analysed the spurions carefully to subtract them from the raw sample signal at the respective ℓ positions.

In the following we describe the analysis of the background signals by fitting of 1D cuts showing the E dependence at fixed Q positions. The 1D data cuts are obtained by using the cut parameters given in Table.(6.1). The background signal in E scans at fixed Q is well described by the fit function given in Equation.(6.1) that contains three Gaussians and a constant contribution.

fit function:

$$f(x) \longmapsto A_1 \mathrm{exp}\Big(-\frac{(\mathrm{x}-\mathrm{a})^2}{2\sigma_1^2}\Big) + A_2 \mathrm{exp}\Big(-\frac{(\mathrm{x}-\mathrm{b})^2}{2\sigma_2^2}\Big) + A_3 \mathrm{exp}\Big(-\frac{(\mathrm{x}-\mathrm{c})^2}{2\sigma_3^2}\Big) + cst, \qquad (6.1)$$

where A_1, A_2, are the amplitudes of the Gaussians that describe the elastic line, A_3 is the amplitude of the Gaussian that describes the spurious signal. a, b and c are the centres of the peaks and σ_1, σ_2, σ_3 are the peak widths. cst is the constant function.

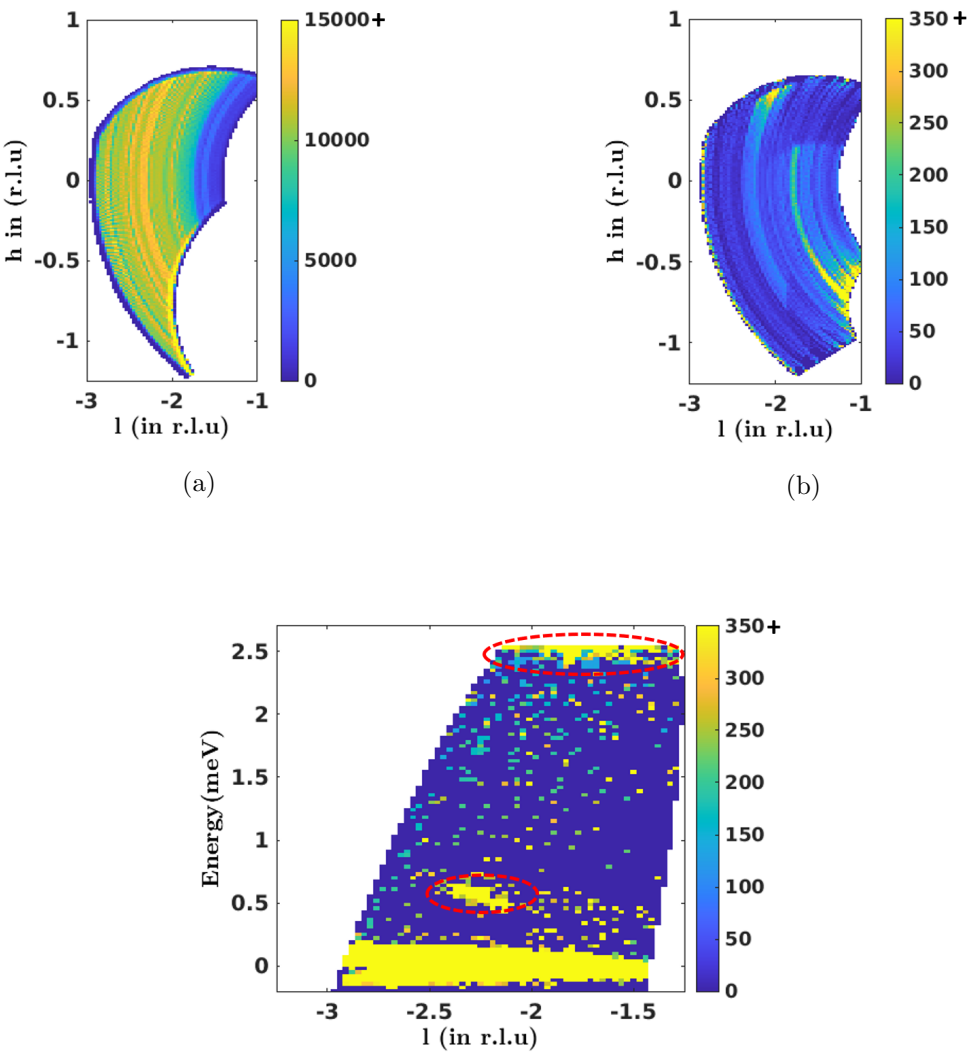

Figure 6.2: LET background scattering measured without sample. (a) & (b) : 2D plots in $h-\ell$ plane ($k = 0$) data with signal integrated (a) over [-0.2, 0.2] and (b) over [0.2, 4] meV. (c) : Background scattering in the $\ell - E$ plane ($h = k = 0$), the red dashed ellipses encircle spurious signals. The colour scale represents the intensities of the scattered neutrons.

Figure.(6.3a) shows fits to the E dependence of the background signal in the range from (0 0 -2.05) to (0 0 -1.7) The peak centre of the suprion is fixed at 2.5 meV, the limit of the data collection range. The fit parameters are shown in the Figure.(6.3b).

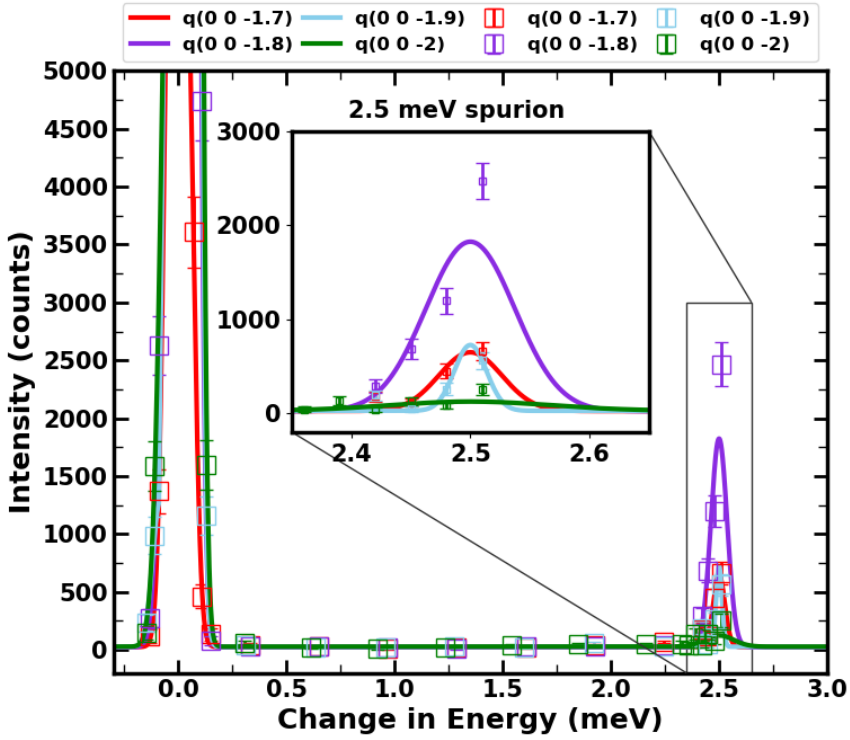

(a)

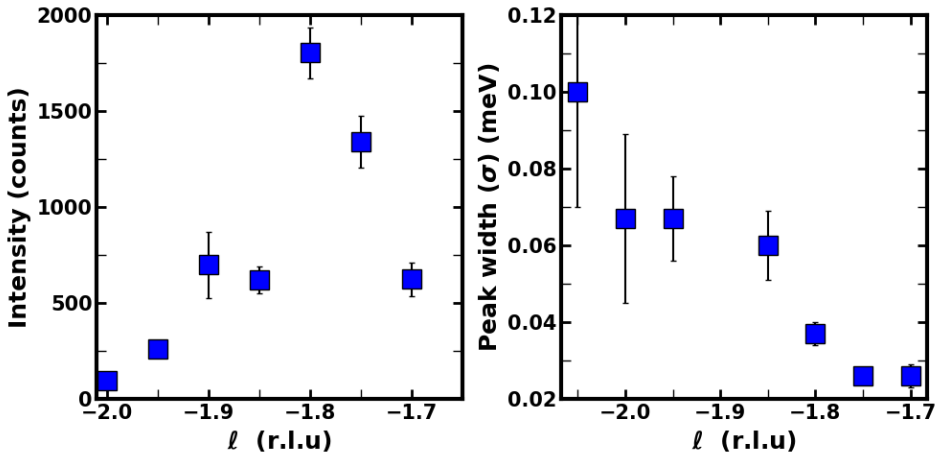

(b)

Figure 6.3: (a) : The analysis of spurious background signal at 2.5 meV. The solid lines represents Gaussian fits. The inset shows the magnified view of the spurion. (b) : ℓ dependence of the Gaussian fit parameters.

Figure.(6.4a) shows fits to the E dependence of the background signal in the range from (0 0 -2.1) and (0 0 -2.3). The peak properties of the signal fitted are shown in the Figure.(6.4b).

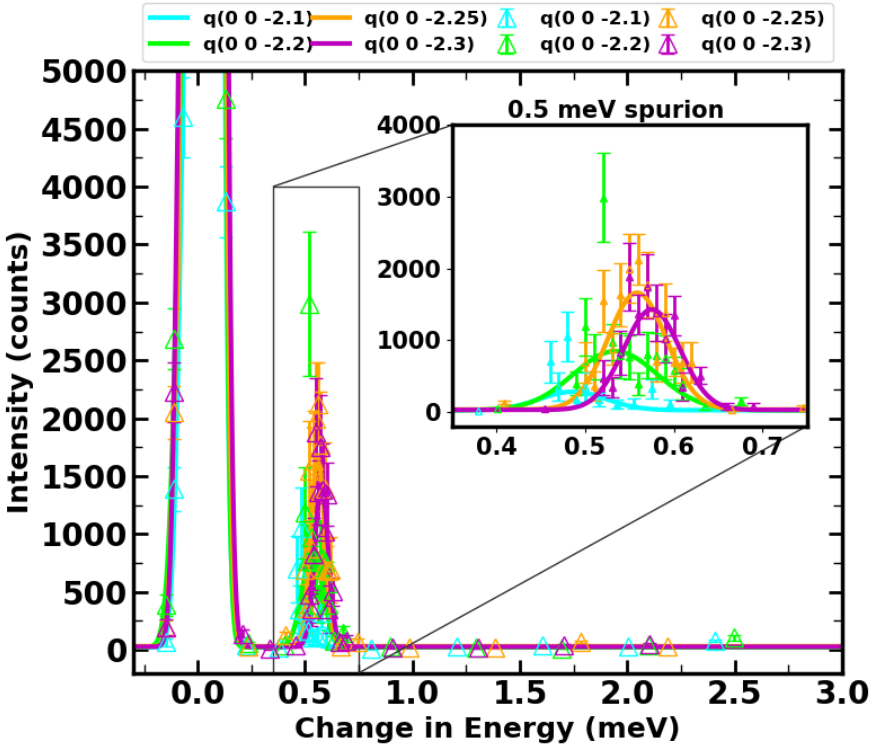

(a)

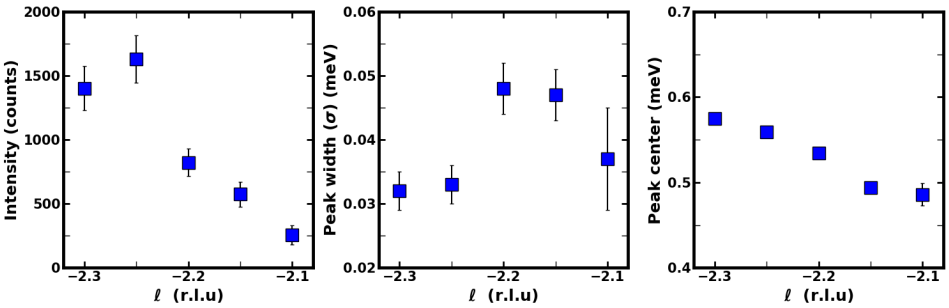

(b)

Figure 6.4: (a) : The analysis of spurious background signal near 0.5 meV. The solid lines represents Gaussian fits. The inset shows the magnified view of the spurion. (b) : ℓ dependence of the Gaussian fit parameters.

To eliminate the contributions of 2.5 meV and 0.5 meV spurion from the raw scattering data, we have subtracted the background given by the fit function (Equation.(6.1) with the obtained fit parameters.

6.3.2 4F2

To identify and analyse the magnetic excitations from the scattering data measured with 4F2 instrument, the implementation of corrections and normalisation of the raw data has to be done manually. We will explain in this section how we process the measured data.

6.3.2.1 Monitor correction

The monitor correction are applied to the data using the experimentally determined k_i dependent correction factor (see Chapter(3))

6.3.2.2 Data normalisation

Data was normalised with respect to a corrected monitor count of 5000, which corresponded to a counting time of approximately 5 minutes.

6.3.2.3 Energy shift correction

The elastic line in the 4F2 data is often seen to be shifted from its nominal zero energy position by an amount of the order of up to $E_s \approx 0.02$ meV, as observed similarly in in MIRA-2. We compensated for E_s by applying corresponding corrections before fitting the data as explained in Subsection(5.3.2). Appendix.(B.7) contains the representative plot of energy shift correction.

6.4 Data fitting and analysis

In this section, we will explain how we fitted LET and LLB data after the necessary corrections were applied to the raw scattering data as explained in the previous sections. To extract the physical parameters, we fitted the whole signal including the elastic line for all measured Q positions except for the Bragg position Q_{FM} = (0 0 -2) and the Q positions in the vicinity of Q_{FM} (i.e, Q positions (0 0 -2.05) and (0 0 -1.95) or equivalent, in the case of LET measurements only). In this case the fits would be dominated by the large intensities of the elastic line and lead to large errors in the fit parameters describing the magnetic excitations. In such a case, we only included the tail of the elastic line up to 10% of its maximum value in the fitted data.

6.4.1 Fit functions

We used three-parameters damped harmonic oscillator function (DHO) and two-parameters over-damped harmonic oscillator function (ODHO) to fit the data as explained in Subsection.(5.4.1). For the fields below H = 3.5 T, we generally used DHO function to fit the data due to the presence of a distinct inelastic peak away from the elastic signal. For fields at H = 3.5 T and above, we used ODHO function to fit the data using Equation.(5.5) where the magnetic excitations are either very soft or overall rather weak. To analyse the data measured at high temperature (T = 37.4 K) with LET instrument at field H = 3.5 T, we used DHO function because of the the presence of an inelastic peak away from the elastic signal due to the thermal activation.

6.4.2 Detailed balance

To account for detailed balance (see Chapter(3)) this has also been included via the factor in Equation.(6.2).

$$f_{db(E,T)} = \frac{1}{|1 - \exp(\frac{-\mathrm{E}}{\mathrm{k_B T}})|} \tag{6.2}$$

6.4.3 Representative examples of the fits

Figure.(6.5) shows the representative examples of the plots fitted with DHO or ODHO functions to the data measured at LET and LLB-I with a constant. The examples show the data fitted with DHO function measured at LET at $H = 0$ T, $T = 2$ K (Figure.(6.5a)) and ODHO function fitted to the data measured at 4F2 at H =3.5 T, $T = 4$ K (Figure.(6.5b)) for Q_{FM} = (0 0 -2).

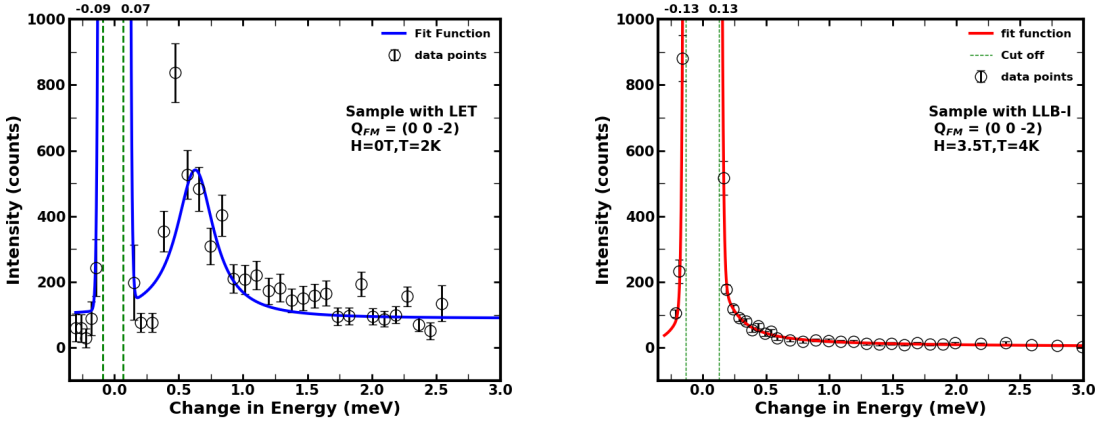

(a) (b)

Figure 6.5: Representative plots of fitted example data sets measured at LET and 4F2. (a) Data measured at LET at $H = 0$ T, $T = 2$ K fitted with DHO function with a constant. (b) Data measured at 4F2 at $H = 3.5$T, $T = 4$K fitted with ODHO function with a constant. The solid lines (blue and red) are the fit functions. The vertical green dashed lines delimit the energy range including the maximum of the elastic line that was excluded from the whole signal fit.

In the damped regime, the magnetic excitations form a distinct peak away from the elastic line (Figure.(6.5a)), in the overdamped regime the signal becomes quasi elastic where the features of the magnetic excitations are hard to distinguish from the elastic line (Figure.(6.5b)). Fits at or near the ferromagnetic ordering wave vector (Q_{FM} = (0 0 -2) and (0 0 -1.95) or equivalent) are obtained by excluding the counts above 10% of the maximum elastic line intensity. Due to the instrument's finite resolution ellipsoids the detected signals are often composed of two Gaussian peaks at the elastic line for the Q positions measured at LET (for all Q positions) and 4F2 (for only certain Q positions). In those cases, to fit the whole signal we used two Gaussian functions to fit the elastic line along with the functions of detailed balance, DHO or ODHO for the inelastic part of the signal and a constant term.

Figure.(6.6) shows representative examples of two Gaussian peaks observed at the elastic line for selected Q positions scanned at 4F2 and LET fitted using Equation.(5.7) with a constant term. The constant term is added in all the fits for the data measured at various beam-time to account for the background scattering in the data.

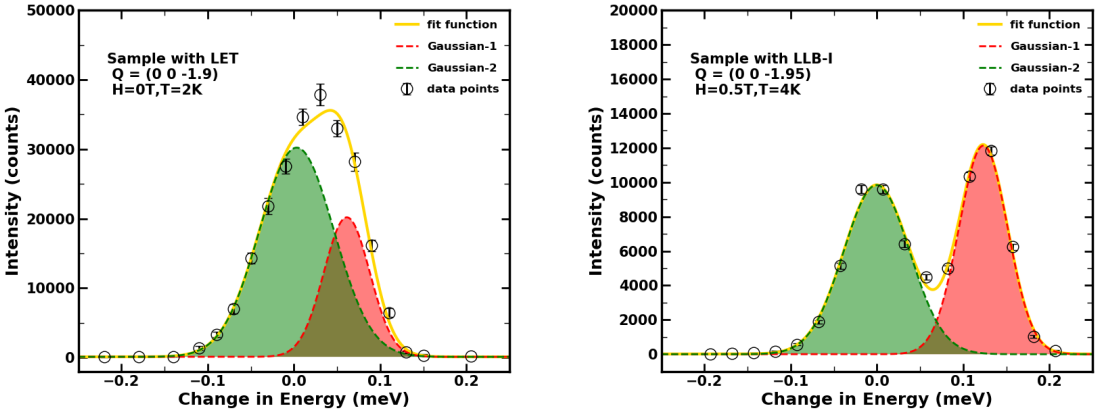

(a) (b)

Figure 6.6: Representative plots of two Gaussian functions fitted to the elastic lines measured at LET and 4F2. (a) Data measured at LET at $H = 0$ T, $T = 2$ K (b) Data measured at LLB-I at $H = 0.5$ T, $T = 4$ K. The solid yellow line represents the elastic line data fitted using the whole fit function using Equation.(5.7) with a constant, (f_{DHO} was used to fit the inelastic part). The green and red shaded area and the dashed lines represent Gaussian functions composed of the elastic line data.

6.5 Results

In this section we investigate transverse field (H‖a) evolution of the low-energy magnetic excitations as measured on LET at ISIS and on 4F2 at LLB. We will focus in particular on the question where with respect to Q_{FM} and Q_{SDW} the excitations become soft.

Figure.(6.7) displays the measurements of the low energy magnetic excitations in the reciprocal space measured at different magnetic fields and the base temperature $T_b = 2$ K with LET using $E_i = 3.16$ meV. The bin widths used to create those plots are given in Table.(6.1). To get an overview of the inelastic signals, we integrated the energy over the range [0.2, 4] meV. From the figures we can clearly see the magnetic excitations range from (0 0 -2.35) to (0 0 -1.65) (encircled in the red dashed lines) in the integrated low-energy range. Our investigation is divided into three parts, Firstly, we explore the evolution of magnetic excitations at ferromagnetic Q position (Q_{FM} = (0 0 -2)) r.l.u. to locate the critical field (H_c). In the second part, we present the ℓ and h dependence of the magnetic excitations measured at different magnetic fields. In the third part, we explore the temperature dependence of the magnetic excitation spectra at

the critical field (H_c).

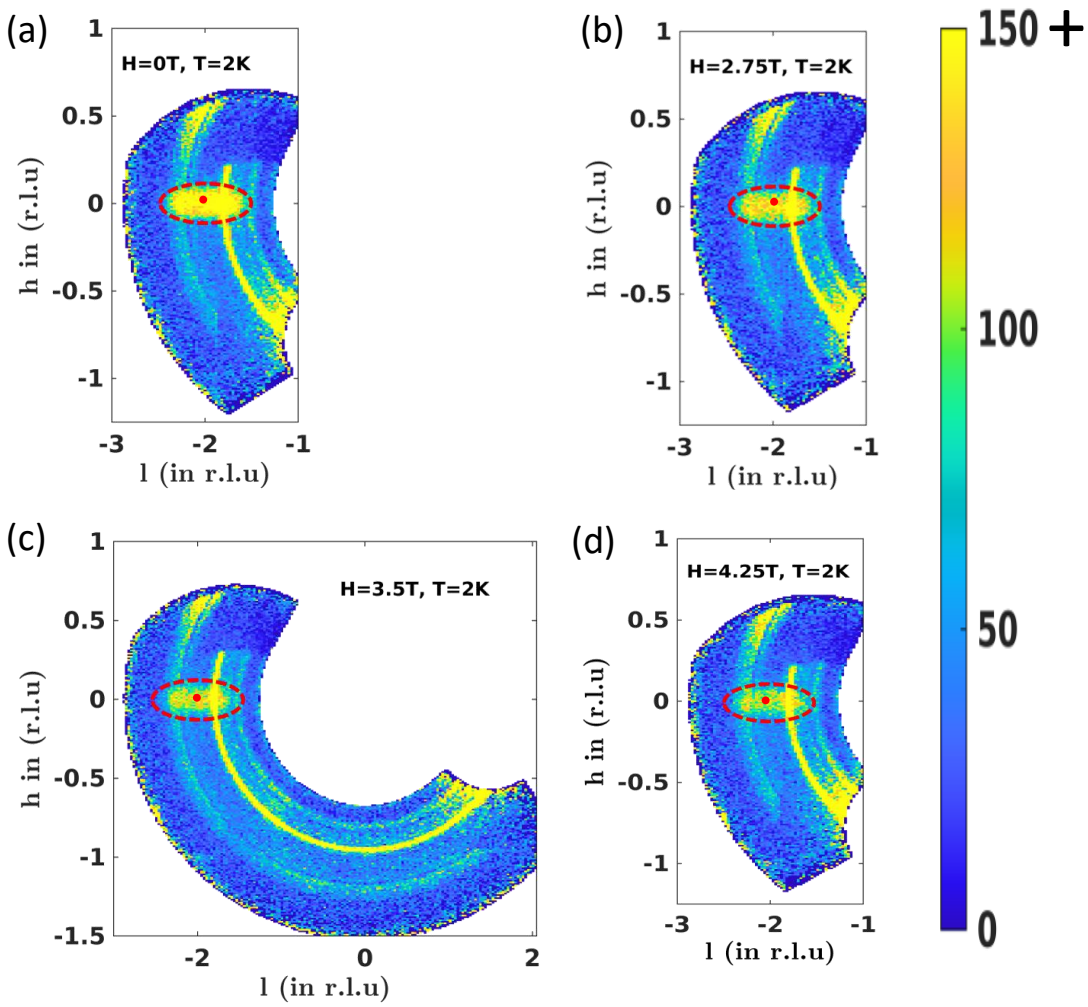

Figure 6.7: Transverse field dependence of low energy inelastic scattering at 2 K. Plots show integrated signals in the range [0.2, 4] meV, excluding the elastic line. (a) $H = 0$ T, $T = 2$ K (b) $H = 2.75$ T, $T = 2$ K (c) $H = 3.5$ T, $T = 2$ K (d) $H = 4.25$ T, $T = 2$ K. The high intensity in the red ellipse shows the visibility of the magnetic excitations in the ℓ direction. The red dot inside the ellipse indicates the Q_{FM} = (0 0 -2). The colour scale represents the neutron intensities. The circular features represents the powder lines

6.5.1 Magnetic field evolution of low energy excitations at Q_{FM}

The overview of the inelastic data in Figure.(6.7) shows that a large number of magnons are found in the reciprocal-space region around (0 0 -2) position. Here we investigate the transverse

magnetic field evolution of the low energy magnons particularly at the ferromagnetic position Q_{FM} for identifying, in particular any critical field where the magnetic excitations become soft or enhanced.

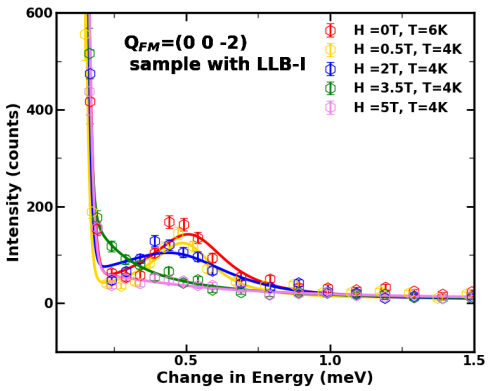

(a)

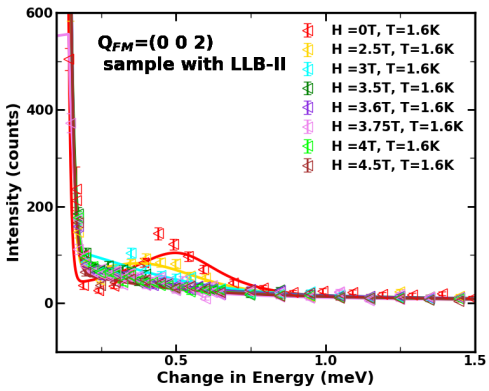

(b)

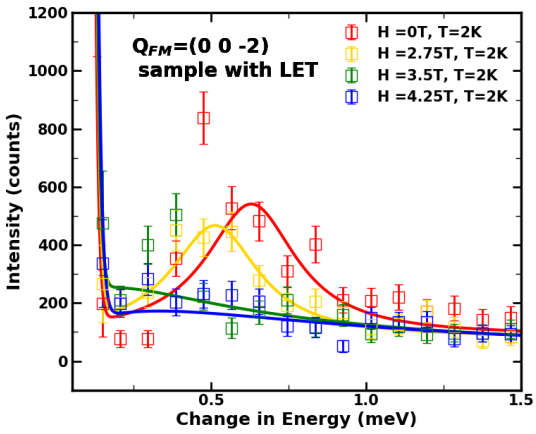

(c)

Figure 6.8: (a) : Representative plots of magnetic excitations measured at Q_{FM} = (0 0 -2) or equivalent ((0 0 2) measured with 4F2) at different magnetic fields and base temperatures during beamtimes (a) LLB-I, (b) LLB-2 and (c) LET. Fits to the data are indicated by solid lines.

Figure.(6.8) shows representative data measured at the Q_{FM} position. We fitted the data obtained below the magnetic field 3.5 T using DHO function and for the data measured at 3.5 T and above, we used ODHO function. In the FM state, at field H = 0 T, the low energy

magnetic excitations have a distinct peak away from the elastic line which can be described with a resonance energy parameter. As the magnetic field is increased the latter gets softer and the signal becomes quasi-elastic at the field H = 3.5 T and for higher fields the signals become weaker. Figure.(6.8b) shows the magnetic excitations were measured for more magnetic fields at the field around H=3.5 T during the LLB-II beamtime.

The fitted parameters describing the field evolution of the magnetic excitations measured in different instruments at Q_{FM} position are shown in Figure.(6.9). It shows the field dependence of the line width (Γ) and the resonance amplitude (χ_0) of the excitations. The χ_0 values have been normalised to the H = 0 T values at each beamtime.

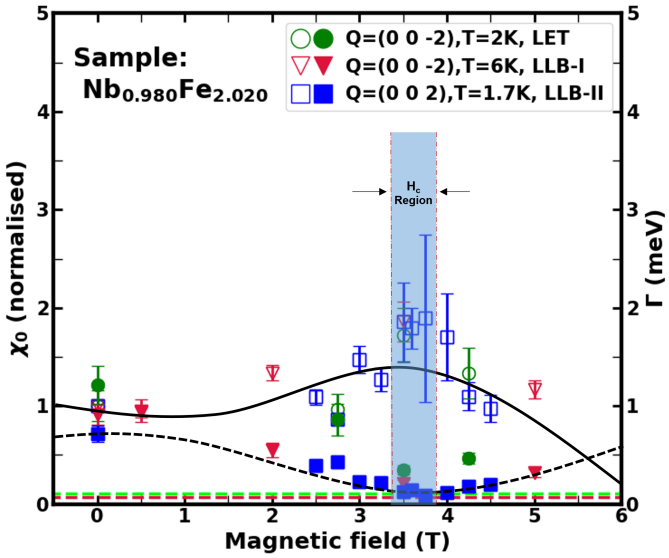

Figure 6.9: Field evolution of fit parameters extracted by fitting DHO and ODHO functions to the magnetic excitations observed at Q_{FM} = (0 0 -2) or equivalent position measured during different beamtimes and at different instruments. The empty and full marker shows resonance amplitude (χ_0) (normalised with the value measured at field H = 0 T) and line width (Γ) respectively. The blue shaded area represents a field region around H_c = 3.6 T where the magnetic excitations become critical. The black solid and dashed curves are guides to the eye. Crimson and lime horizontal dashed lines indicate the instrument resolutions of 4F2 (0.066 meV) and LET (0.108 meV) instruments respectively.

In the FM state, with increasing magnetic field Γ is gradually decreasing and reaching to a minimum value $\Gamma \approx 0.142 \pm 0.024$ meV close to the instrument resolution around a critical filed of $H_c \approx 3.6$ T. Due to the closeness of the reported Γ value to the instrumental resolution

the value can only be interpreted as an upper bound of the true value of Γ. For higher fields, the values recover. At the same time, the resonance amplitude (χ_0) is gradually increasing with increasing field and reach a maximum. Above H=4T, values decrease as the magnetic signals become weaker.

6.5.2 l dependence of magnetic excitations

From the previous section, we identified the field H_c around which the magnetic excitations measured at Q_{FM} position are getting soft. In this section, we look at the ℓ dependence of the low energy magnetic excitations measured at different magnetic fields.

Figure(6.10) displays 2D plots showing the ℓ dependence of the low energy magnetic excitations measured with LET at the base temperature T_b =2 K using E_i = 3.16 meV. The bright yellow stripe around zero energy transfer represents the elastic line.

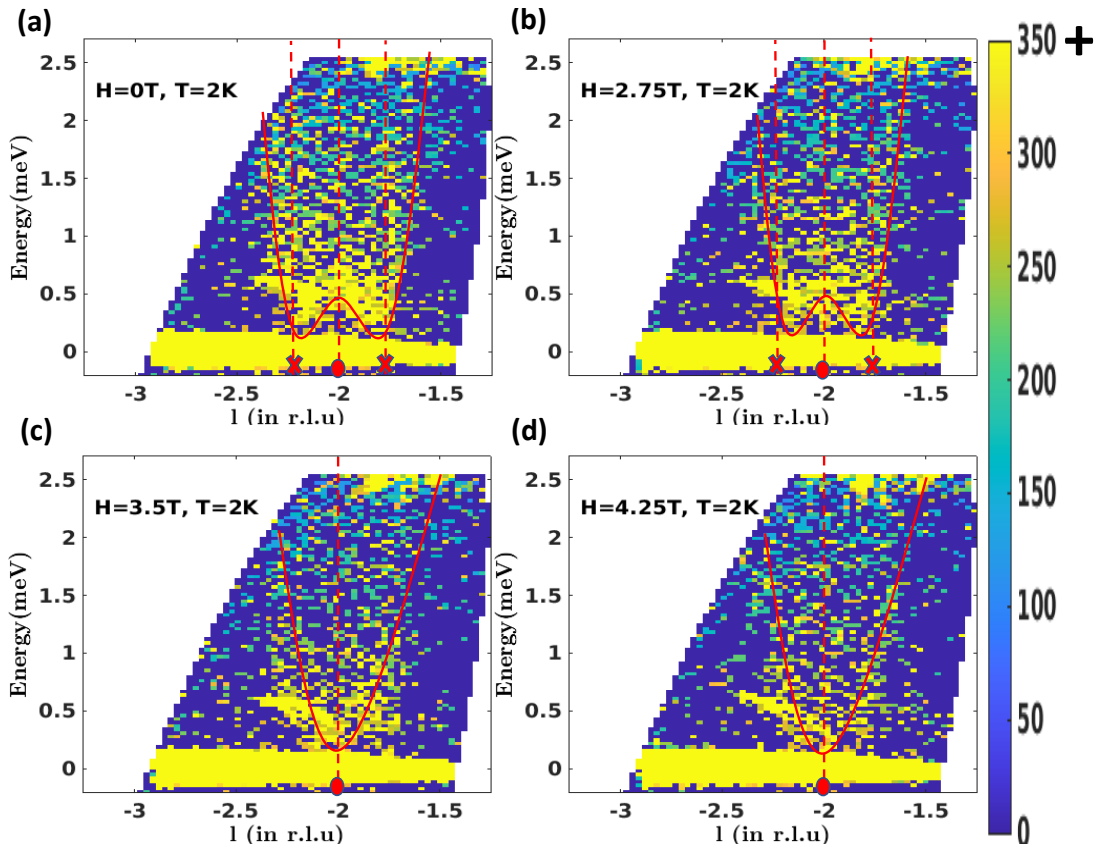

Figure 6.10: The ℓ dependence around Q_{FM} = (0 0 -2) of the magnetic excitations measured with LET at different magnetic fields at 2 K(a) H=0T (b) H=2.75T (c) H=3.5T (d) H=4.25T. The red solid line indicates the guide to the eye for the dispersion of the magnetic excitations along ℓ direction. The red disk and crosses (each with a dashed line on top) indicate respectively Q_{FM} and Q_{SDW} positions. The colour scale represents the neutron intensities.

At field H = 0 T and T_b = 2 K the sample lies deep in the FM state and we expect the excitation energy to be lowest for the Q_{FM} = (0 0 -2) r.l.u. position (marked red circle). However, from Figure.(6.10 a) we can see that the minima of the dispersion are found on either side of the Q_{FM} position instead. Also, we observe that in the FM state an energy gap of approx. 0.2 meV is present. Above the energy transfer 0.2 meV, a well-defined dispersion curve is observed with features as explained. Figure.(6.11) shows the 1D plots of the Q_{FM} position where a well defined peak for the magnetic excitations are observed above the energy gap approx. 0.2 meV for magnetic fields H = 0 T and H = 2.75 T, and they are absent for the fields H = 3.5 T and H = 4.25 T. These features in the dispersion of the magnetic excitations are as observed similarly in the previous neutron scattering studies done by Poulten and Lucas with LET [55, 74].

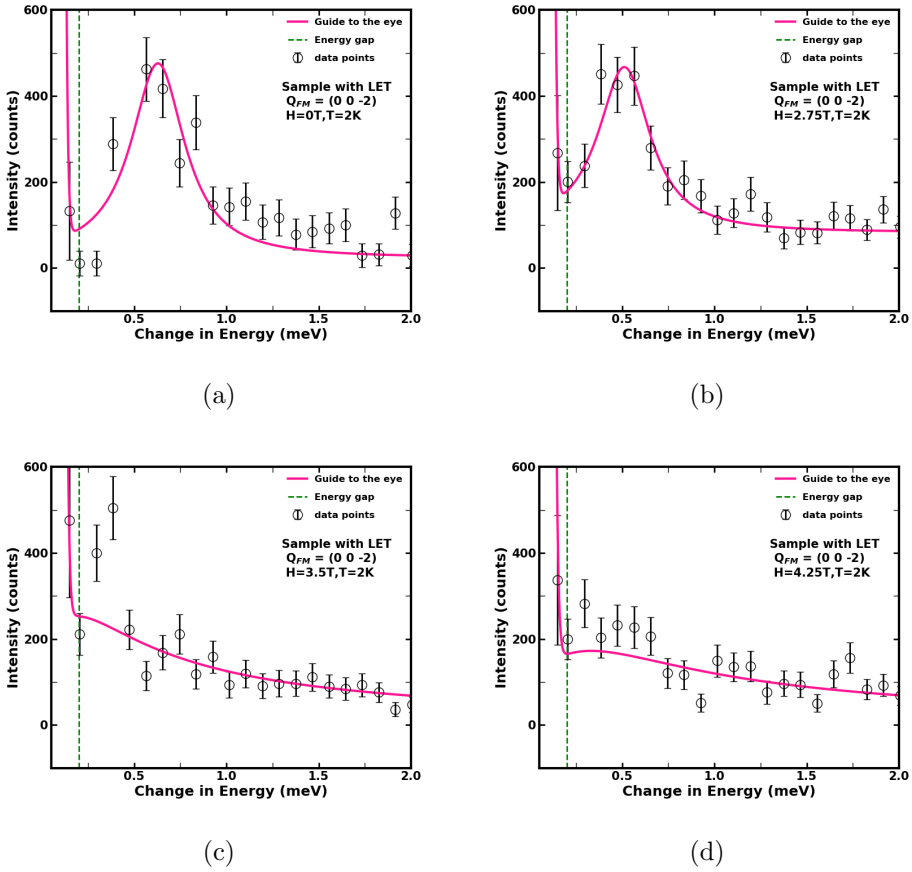

Figure 6.11: (a) : Representative plots of magnetic excitations measured at Q_{FM} = (0 0 -2) with LET at different magnetic fields and base temperature 2K. (a) H = 0 T , (b) H = 2.75 T, (c) H = 3.5 T and (d) H = 4.25 T. The solid line is guide to the eye. The green vertical dashed line indicates the energy gap $E_g \approx 0.2$ meV.

With increasing field, H = 2.75 T, T =2 K (Figure.(6.10b)), we see that the positions of the minima are moving towards the Q_{FM} and also the maximum of the excitation energy at Q_{FM} position is decreased with applied field (ses Figure.(6.11b)). However, the energy gap $\approx$ 0.2 meV is still present. For the fields H = 3.5 T and H = 4.25 T the shape of the dispersion curves are changed (see Figures.(6.10c & d)). The minima are now at Q_{FM} and the energy gap observed at fields H = 0 T and H = 2.75 T is now closed at the fields H = 3.5 T and 4.25 T close to the resolution of LET (ses Figure.(6.11c&d)).

In the following, we will look at the field regimes $H < H_c$, $H = H_c$ and $H > H_c$. Figure.(6.12) lists the fields and the instruments used to measure the ℓ dependence in different regimes in a schematic table. Figure.(6.12b) displays the representative plot obtained at H = 0T, T = 2 K to indicate the different ℓ positions.

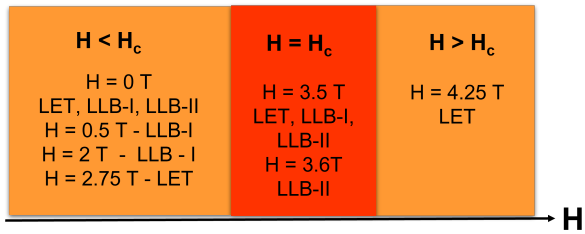

(a)

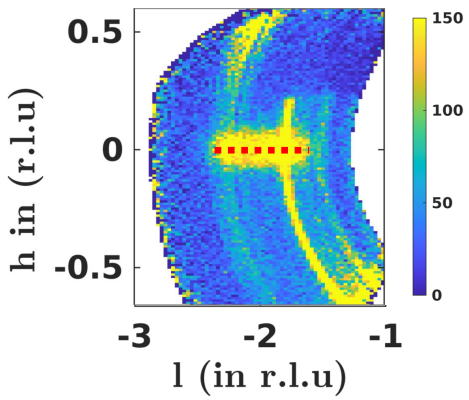

(b)

Figure 6.12: (a) Schematic table listing for different field regimes the measurement fields and beamtimes. (b) Representative plot (measured at H=0T, T=2K) showing the integrated inelastic scattering in the range [0.2, 4] meV from measurements at LET. The colour scale represents neutron intensity. The red dots denote the q positions for which the energy dependence of the scattering has been analysed.

6.5.2.1 $\mathbf{H < H_c}$:

In this subsection, we look at the ℓ dependence of the magnetic excitations in the region $H < H_c$. We measured neutron scattering data in this region at the fields H = 0 T, 0.5 T, 2 T and 2.75 T at the base temperature $T_b < 7$ K during beamtimes LET and LLB-I.

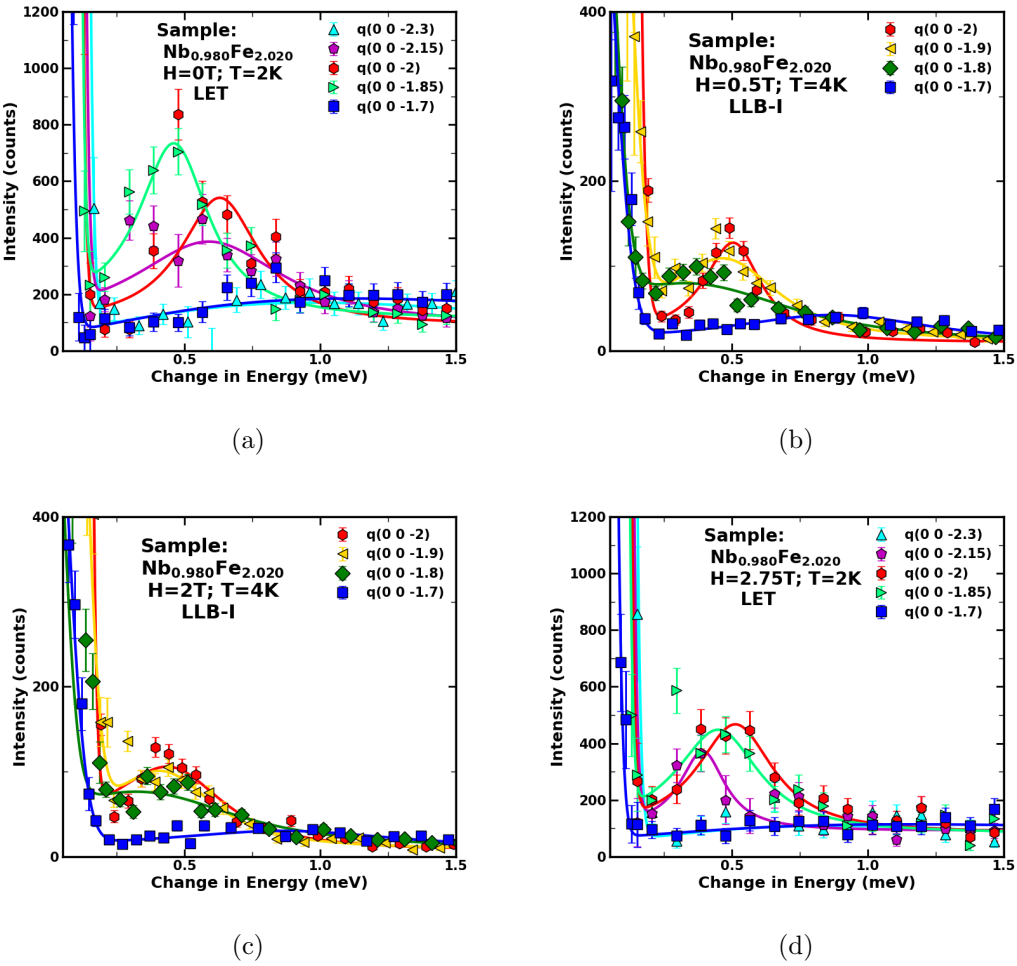

Figure 6.13: Representative plots of the magnetic excitations measured across Q_{FM} in the ℓ direction at different magnetic fields. (a) H=0T, T=2K - LET (b) H=0.5 T, T=4 K - LLB-1 (c) H=2 T, T=4 K - LLB-I (d) H=2.75T, T=2K - LET. The magnetic excitations are fitted (solid lines) with DHO function.

Figure.(6.13) shows representative plots of the ℓ dependence of magnetic excitations measured at different magnetic fields. The magnetic excitations below the critical field ($H < H_c$), where the sample is in the FM state have a distinct peak outside the elastic line which can be described with a resonance energy parameter. The data measured at different fields were fitted with DHO function with a constant. From Figure.(6.13) we could make the following qualitative observations within the $H<H_c$ regime: the excitation spectra tend to show distinct peaks, away from Q_{FM} the resonance energies tend to increase and the amplitudes to decrease, and with increased field the resonance energies tend to decrease. Appendix.(B.2) contains additional information on the data set in the $H<H_c$ regime including fit details.

The fitted parameters describing the evolution of the ℓ dependence of the magnetic excitations with field are shown in Figure.(6.14) and Figure.(6.15).

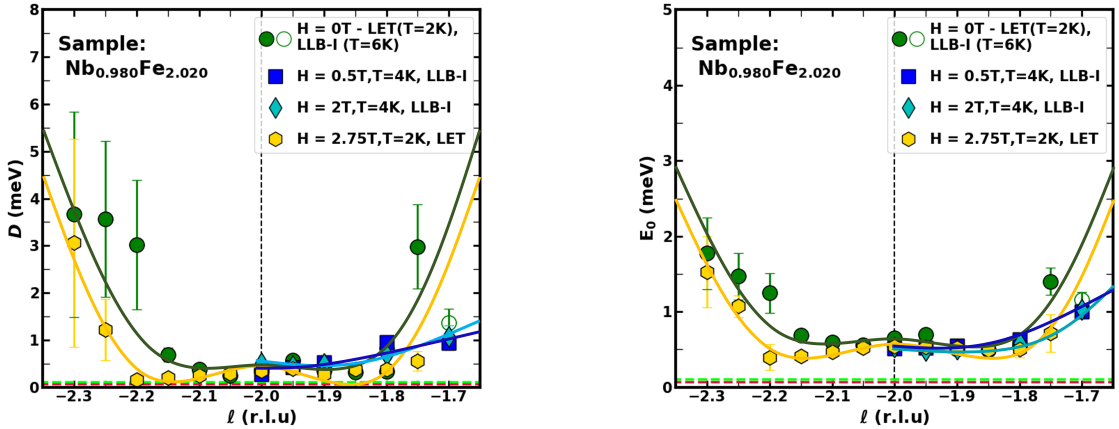

(a) (b)

Figure 6.14: Field evolution of fit parameters extracted by fitting DHO function to the magnetic excitations measured across Q_{FM} = (0 0 -2) r.l.u along ℓ direction in different instruments. (a) Damping factor (D). (b) Excitation energy (E_0). The empty and full marker indicates data measured at LLB-I and LET respectively. The solid lines indicate the guide to the eye capturing the general trend of the fit parameters along ℓ direction. Crimson and lime horizontal dashed lines indicate the instrument resolutions of 4F2 (0.066 meV) and LET (0.108 meV) instruments respectively.

Figure.(6.14) shows the ℓ dependence of the damping factor (D) and resonance energy (E_0). The main observation is that for both parameters the values are lowest around Q_{FM}. In a ℓ window of almost 0.4 r.l.u. there is little change. Field induced changes are also only subtle for H<H_c. Figure.(6.15a) shows the ℓ dependence of the resonance amplitude (χ_0). The resonance amplitude is normalised with values at Q_{FM} = (0 0 -2) for all the fields. For field H = 0 T, the χ_0 value has a maximum away from Q_{FM} position. The maximum is becoming less pronounced on increasing field. The ℓ dependence on Γ is shown in Figure.(6.15b). At H=0 T, Γ reaches a minimum of about 0.52±0.28 meV away from Q_{FM}. The main effect of increasing field is the suppression of the local maxima around Q_{FM}. The larger error bars in the values of Γ for the far away Q positions are due to the magnetic excitations becoming weaker.

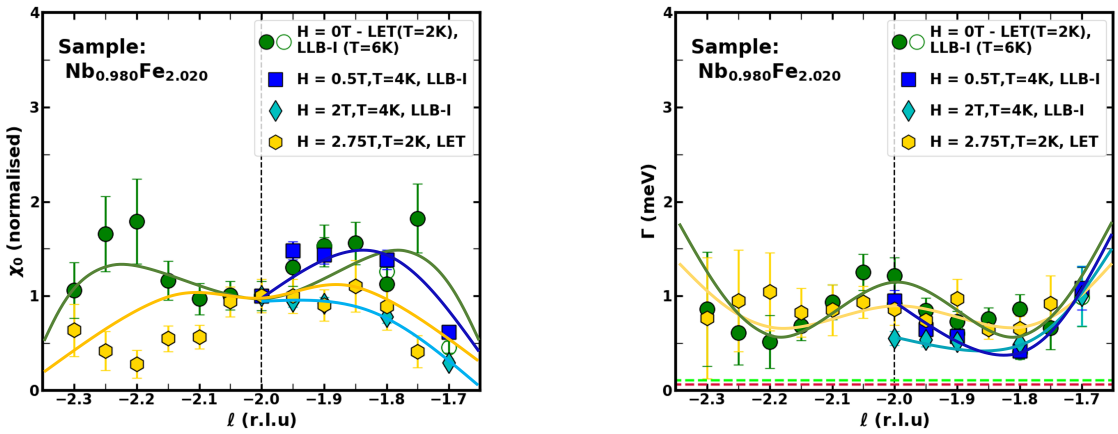

(a) (b)

Figure 6.15: ℓ dependence across Q_{FM}= (0 0 -2) of (a) resonance amplitude and (b) Γ at H<H_c. Values of χ_0 have been normalised to the values measured at Q_{FM}. The solid lines indicate the guide to the eye. Crimson and lime horizontal dashed lines indicate the instrument resolutions of 4F2 (0.066 meV) and LET (0.108 meV) instruments respectively.

6.5.2.2 H = H_c :

Here we look at the magnetic excitations in the region where H $\approx$ H_c = 3.6 T. Figure.(6.16) shows representative plots of the magnetic excitations measured with LET (Figure.(6.16a)) and during LLB-II (Figure.(6.16b)). Appendix.(B.3) contains details of fitting for data obtained in the critical-field regime.

From Figure.(6.16), reveals substantial quasielastic scattering in the region near Q_{FM}. The weight of the signal is shifted to higher energies and appears to be reduced overall for Q positions further moved from Q_{FM}. The fit parameters describing the ℓ dependence of the magnetic excitations at H $\approx$ H_c are shown in Figure.(6.17. Figure.(6.17a) shows the ℓ dependence of the resonance amplitude and has a maximum near Q_{FM}. Figure.(6.17b), shows that Γ, on the other hand, has a minimum near Q_{FM} with $\Gamma \approx 0.349 \pm 0.048$ (measured with LET at H_c = 3.5 T) and 0.142 $\pm$ 0.024 meV (measured with LLB-II at H_c = 3.6 T) respectively. Due to the closeness of the reported Γ value to the instrumental resolution the value can only be interpreted as an upper bound of the true value of Γ, of the two result the latter carries more weight as it is supported by measurements with better statistics.

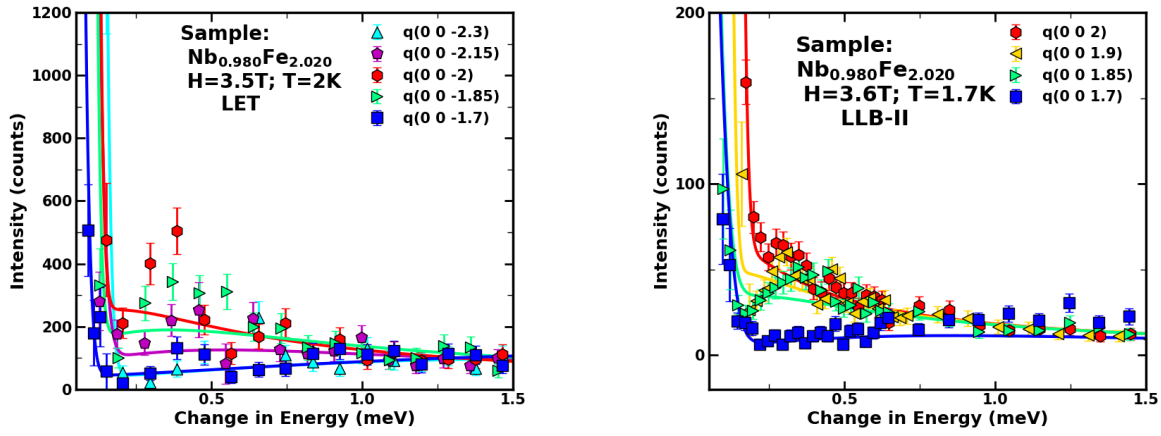

(a) (b)

Figure 6.16: Representative plots of the magnetic excitations measured near H_c across Q_{FM} in the ℓ direction with LET and during LLB-II. (a) H=3.5T, T=2K - LET (b) H=3.6 T, T=1.7 K - LLB-II. The solid lines are fits using the over damped harmonic oscillator model. LET data fit quality has been affected by reduced statistics.

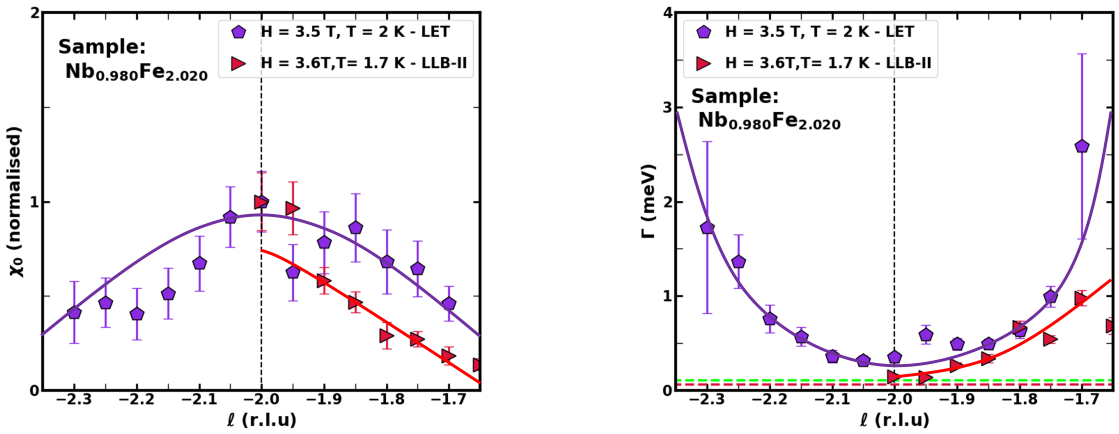

(a) (b)

Figure 6.17: ℓ dependence across Q_{FM} = (0 0 -2) of (a) resonance amplitude χ_0 and (b) Γ at H approx H_c. Values of χ_0 have been normalised to the values at Q_{FM}. χ_0 shows a clear maximum and Γ a clear minimum near Q_{FM}. Solid lines are guides to the eye. Crimson and lime horizontal dashed lines indicate the instrument resolutions of 4F2 (0.066 meV) and LET (0.108 meV) instruments respectively.

6.5.2.3 H > H_c :

Now we look at the evolution of magnetic excitations above the critical field. To look at the ℓ dependence of the magnetic excitations, we measured data at field H = 4.25T with LET and they are fitted using the ODHO model. Figure.(6.18) shows representative plots of the magnetic excitations measured across Q_{FM} in the ℓ directions. We can see from the figure that the excitations appear quasi-elastic and become weaker when moving away from Q_{FM}. Appendix.(B.4) contains details of fitting for data obtained above the critical-field.

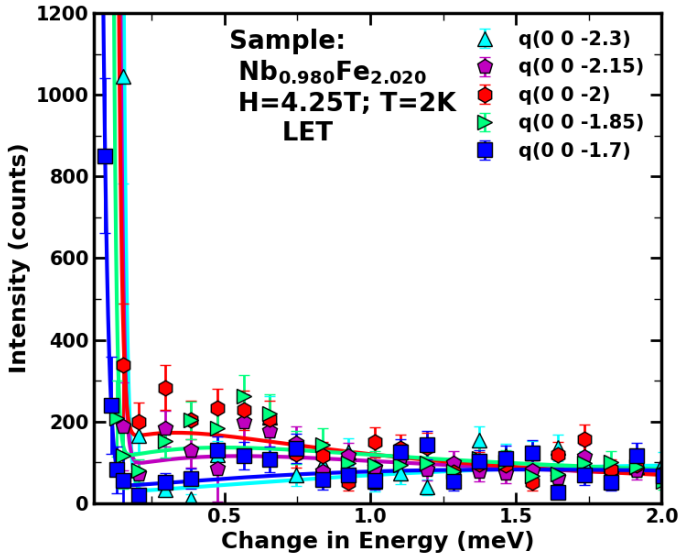

Figure 6.18: Representative plots of the magnetic excitations measured across Q_{FM} in the ℓ direction at H =4.25 T > H_c The magnetic excitations are fitted (solid lines) using ODHO function.

Figure.(6.19) displays the ℓ dependence of the resonance amplitude (χ_0) and line width (Γ) obtained by fitting the ODHO model. The resonance amplitude is normalised with value at Q_{FM} = (0 0 -2). The results are qualitatively similar to the findings near H_c in that χ_0 has a maximum and the line width Γ has a minimum near Q_{FM}. Γ is slightly larger at $H > H_c$ with the value at Q_{FM} of $\Gamma \approx 0.467 \pm 0.057$ meV (above the limit of the energy resolution of the instrument).

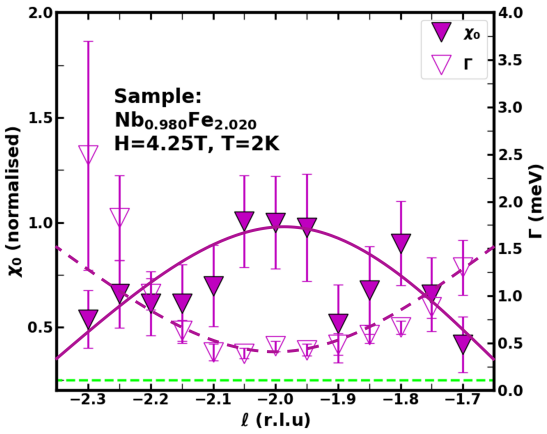

Figure 6.19: ℓ dependence across Q_{FM}= (0 0 -2) of the resonance amplitude χ_0 and linewidth Γ at H = 4.25 T > H_c. χ_0 shows a clear maximum and Gamma a clear minimum near Q_{FM}. Lines are guides to the eye. Lime horizontal dashed line indicates the instrument resolution of LET (0.108 meV) instrument.

6.5.3 h dependence of magnetic excitations at the critical field (H_c)

To investigate the dispersion of the magnetic excitations in the h direction at the critical field we collected data across Q_{FM} = (0 0 2) r.l.u. at H_c = 3.6 T, T = 1.7 K. Figure.(6.20) shows representative scans of the magnetic excitations. It appears that with increasing h value the spectral weight is reduced and shifted to higher energies.

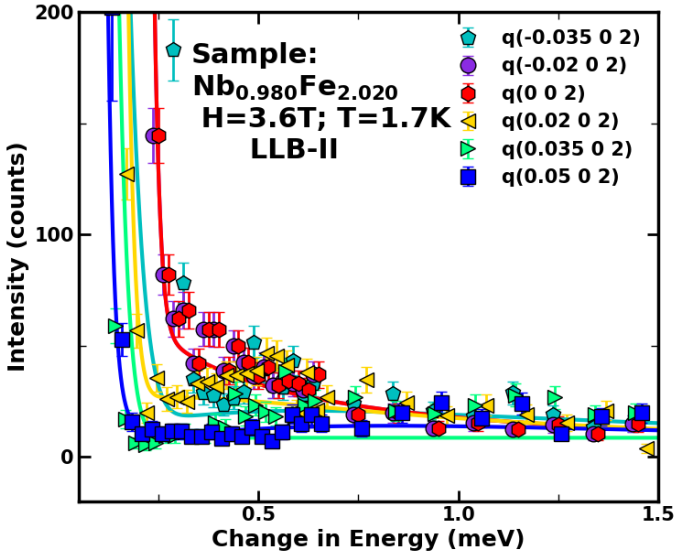

Figure 6.20: Representative plots of the magnetic excitations measured across Q_{FM} in the h direction. The magnetic excitations are fitted (solid lines) using ODHO model.

Appendix.(B.5) contains details of fitting for the h dependent data set obtained at the critical-field.

The h dependence of the fit parameters, resonance amplitude (χ_0) and line width (Γ) extracted from the fits are displayed in Figure.(6.21). The resonance amplitude is normalised with value at Q_{FM} = (0 0 2) r.l.u. The χ_0 shows a maximum at Q_{FM} position and on moving away, the values are decreasing rapidly compared to the ℓ dependence at H=H_c. The Γ shows a minimum at Q_{FM} and increases with increasing h magnitude.

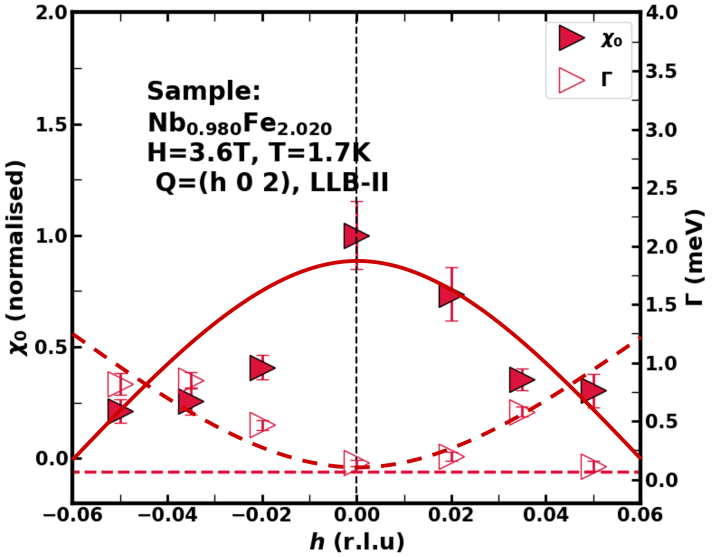

Figure 6.21: h dependence of the resonance amplitude (χ_0), normalised with the value measured at Q_{FM} = (0 0 2) r.l.u and line width (Γ) extracted by fitting ODHO model to the magnetic excitations measured across Q_{FM} = (0 0 2) r.l.u at H = 3.6 T, T = 1.7 K. The lines are guides to the eye. Crimson horizontal dashed line indicates the instrument resolution of 4F2 (0.066 meV) instrument.

6.5.4 Temperature dependence of magnetic excitations at the critical field (H_c) region

In this section, we will investigate the temperature dependence of the magnetic excitations measured in the critical field region. First, we look at the temperature dependence of the magnetic excitations at the Q_{FM} position measured at H_c=3.6 T and then we observe the dispersion along ℓ direction measured at H_c=3.5 T.

Figure.(6.22) shows the temperature dependence at the Q_{FM} position at H_c fitted with the over damped harmonic oscillator model for T=1.6 K and damped harmonic oscillator model for T = 15 and 32.5 K. The figure demonstrates the thermal activation of the magnetic excitations. Figure.(6.23) displays the temperature dependence of the fit parameters, resonance amplitude (χ_0) normalised with the value obtained at T=1.6 K and line width (Γ). With the increase in the temperature, the χ_0 values are gradually decreasing whereas Γ is slowly increasing.

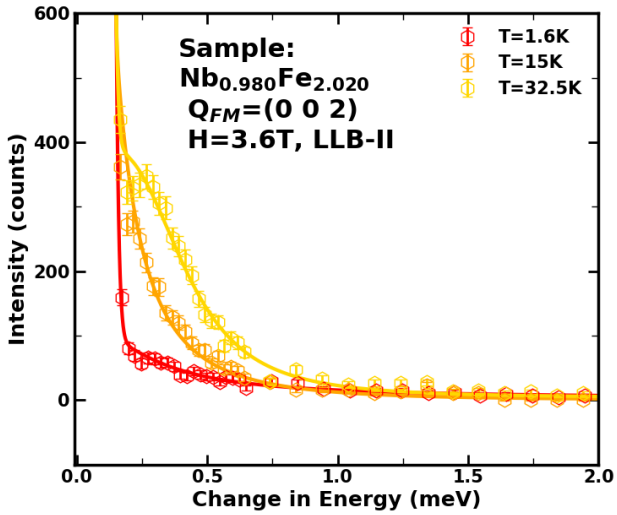

Figure 6.22: Temperature dependence of the magnetic excitations at Q_{FM} at $H_c = 3.6$ T. The magnetic excitations are fitted (solid lines) with damped (T = 32.5 and 15 K) and over-damped (T = 1.6 K) harmonic oscillator models.

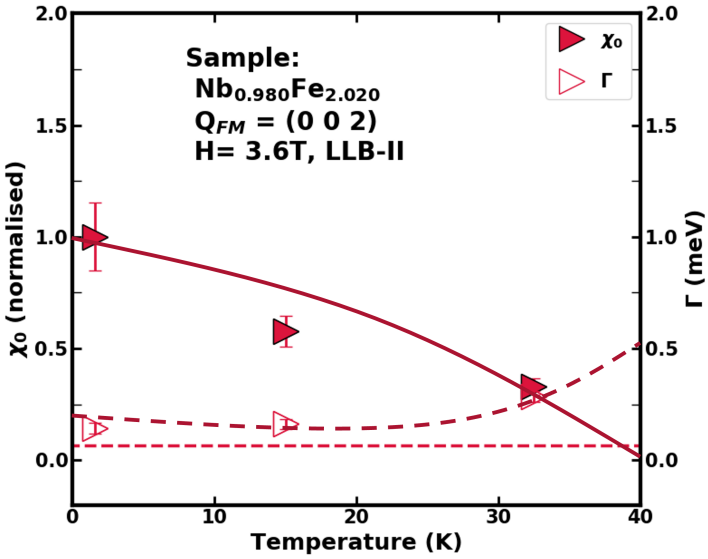

Figure 6.23: Temperature dependence of the fit parameters; resonance amplitude (χ_0) normalised with the value measured at T = 1.6 K and line width (Γ), extracted by fitting the magnetic excitations with the DHO and ODHO model at Q_{FM} = (0 0 2) at H = 3.6 T. Lines are guides to the eye. Crimson horizontal dashed line indicates the instrument resolution of 4F2 (0.066 meV) instrument.

6.5.4.1 l dependence of the critical field magnetic excitations at high temperature

To look at the magnetic excitations at high temperature regime we measured data at H=3.5 T, T=37.4 K. Figure.(6.24) displays an overview of the location of the magnetic excitations in the reciprocal space. To get an overview of the inelastic signals we integrated the energy over the range [0.2, 4] meV (Figure.(6.24a)). If we compare this with magnetic excitation measured at T=2 K (see Figure.(6.7d)), we can see a significant enhancement in the intensity due to thermal activation. The ℓ dependence of the magnetic excitation is shown in Figure.(6.24b) and exhibits the shape similar to low-temperature measurement at T= 2 K but with increased neutron counts. Appendix.(B.6) contains fitting details of this data set.

Figure.(6.25) shows representative scans of the magnetic excitations measured across Q_{FM} in the ℓ direction. As we can see that the magnetic excitations measured across Q_{FM} position have a pronounced intensity peak for Q_{FM} whereas moving away from that the signal intensities are reduced and the spectral weight shifts to higher energy. The ℓ dependence of the fit parameters of the damped harmonic oscillator model for the magnetic excitations is displayed in Figure.(6.26).

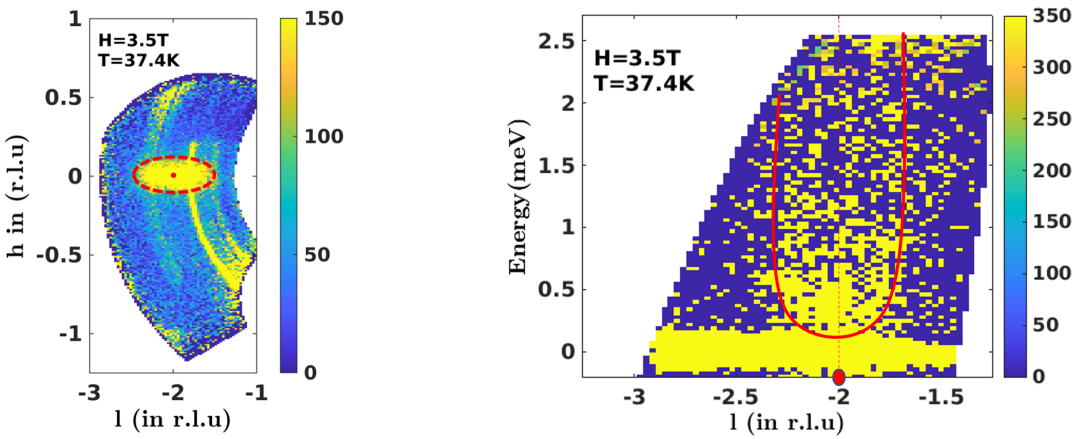

(a) (b)

Figure 6.24: Overview of the magnetic excitations measured at H=3.5T,T=37.4K (a) : Excitations in h - ℓ plane (h 0 ℓ) in integration range [0.2, 4] meV. The red ellipse shows the region with substantial amount low-energy excitations. The red dot indicates the Q_{FM} =(0 0 -2) position. (b) : The ℓ and energy dependence of the magnetic excitations. The solid line is a guide to the eye. The colour scales represent the neutron intensities.

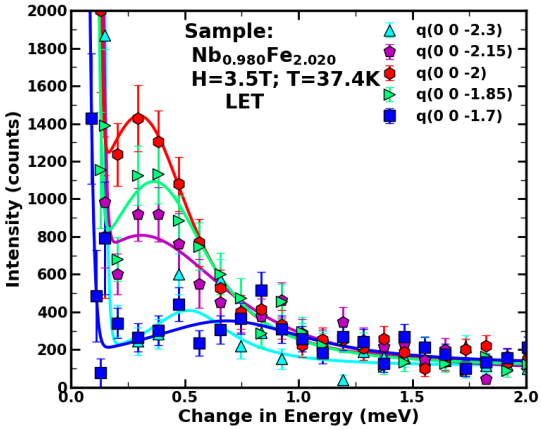

Figure 6.25: Representative plots of the magnetic excitations measured across Q_{FM} in the ℓ direction with LET at H=3.5 T, T=37.4 K. The magnetic excitations are fitted (solid lines) with DHO function.

The resonance amplitude (χ_0) and line width (Γ) are shown in Figure.(6.26a). The χ_0 shows a maximum at the Q_{FM} position and Γ, on the other hand, has minimum near Q_{FM} with $\Gamma \approx 0.464 \pm 0.091$ meV similar to the low T case where Gamma showed a stronger ℓ dependence (see Figure.6.17). The fit parameters, damping factor (D) and resonance energy (E_0) are shown in Figure. (6.26b). Both parameters have a minimum near Q_{FM} and are weakly changing in this area and increasing further away from Q_{FM}.

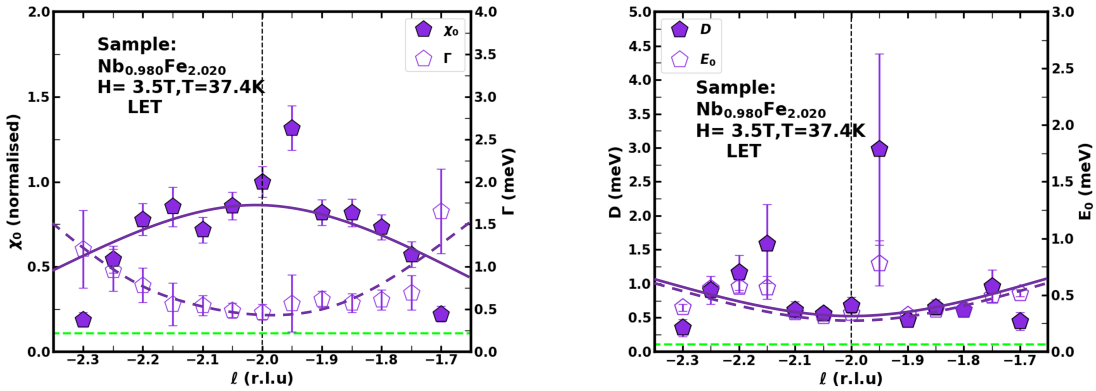

(a) (b)

Figure 6.26: ℓ dependence of the fit parameters of the magnetic excitations measured across Q_{FM} = (0 0 -2) at H = 3.5 T, T = 37.4 K . (a) Resonance amplitude (χ_0)(normalised with the value measured at Q_{FM} = (0 0 -2)) and Γ. (b) Damping factor (D) and resonance energy (E_0). Lines are guides to the eye. Lime horizontal dashed line indicates the instrument resolution of LET (0.108 meV) instrument.

6.6 Discussion

The low energy magnetic excitations are well fitted with DHO and ODHO models below the critical field H_c and H_c at high temperature, and at H_c and fields above respectively, at Q_{FM} and at (0 0 ℓ) positions across Q_{FM}. In the FM state, the low energy magnetic excitations of Q_{FM} have shown that with increasing magnetic field the resonance energy (E_0) and Γ are both gradually decreasing and reaching a minimum, $\Gamma \approx 0.142 \pm 0.024$ meV close to the instrumental resolution and due to the closeness of the reported Γ value to the instrumental resolution the value can only be interpreted as an upper bound of the true value of Γ. and the damping factor (D) and resonance amplitude (χ_0) are gradually increasing and reach a maximum around the critical field of $H_c \approx 3.6$ T (see Figure.(6.17)). The observed result of minimum in the value for Γ close to the energy resolution suggests a possible existence of quantum critical point (QCP) but at the same time only a weak enhancement of χ_0 suggests the transition could be a crossover. These observations from the results suggest both options are possible for the existence of putative FM-QCP with field tuning as our data does not give a concrete evidence for the final answer. The weak enhancement indicative of the crossover behaviour at the critical field could be the instrument resolution or the sample inhomogeneity that lead to a smearing out the of critical field.

For the ℓ dependence of the magnetic excitations at low temperature in zero field we expected that the Γ and χ_0 to be minimum and maximum respectively, at Q_{FM} however, we can see that the minima and maxima of the excitations are found on either side of the Q_{FM} position respectively instead. The Γ reaches a minimum of about 0.52 $\pm$ 0.28 meV away from Q_{FM}. A local maximum on the other hand for Γ observed at Q_{FM} in the FM regime $\approx$ 1.213 $\pm$ 0.193 meV. The main effect of increasing field was the suppression of local maximum. For field at $H = H_c$, the local maximum of the Γ for Q_{FM} was almost reduced to zero close to the instrument resolution. In FM regime, there was a finite energy gap observed for the magnetic excitations in the ℓ window of almost 0.4 r.l.u approximately 0.2 meV, the effect of increasing field was found to be however subtle. At $H = H_c$, the finite energy gap observed was closed, whereas, for $H > H_c$ though the energy gap is closed but finite Γ was observed. The χ_0 and Γ for Q_{FM} at $H > H_c$ found to show maximum and minimum respectively with no energy gap.

Previously it was observed by Poulten *et.al* and Lucas *et.al* that in the FM regime at zero field, the influence of SDW interactions lead to minimum and maximum at Q_{SDW} for Γ and χ_0 respectively where the modified spin fluctuation model (FM+SDW) by considering such effect were able to explain the behaviour of the spin fluctuations [55,74]. These features are observed similarly in our work as well for the zero field measurements of the magnetic excitations which survives to at least $H = 2$ T. The excitation spectrum for the field at H_c and above has been observed that the features are similar to the conventional type of excitations predicted by the spin fluctuation theory (see Chapter(2)) for ferromagnetic critical transitions.

The magnetic excitations measured for the h dependence shows that low energy excitations are predominately located in the vicinity of the ℓ axis even at the H_c. The temperature dependence of the low energy excitations shows thermal activation of spin fluctuations. Presence of large number of low-energy spin fluctuations is expected to lead to non-Fermi liquid (nFL) behaviour in resistivity, magnetic susceptibility, and specific heat capacity, *etc* at H_c that should show up in unusual exponents in the temperature dependence of these quantities. This might indicate a transverse-field induced unmasking of the FM QCP.

7 Summary

The system $NbFe_2$ has been investigated as a prime candidate of a system with ferromagnetic quantum criticality (FM-QCP) masked by spin density wave order. Before this work magnetic order and excitations of large single crystals had already been studied by neutron scattering across the composition temperature phase diagrams. In this work the evolution with field of the $NbFe_2$ system has been explored. The Fe-rich samples studied contained a ferromagnetic (FM) ground state and spin density wave (SDW) and paramagnetic phase at higher temperature. Longitudinal fields H‖c and transverse fields H‖a have been applied.

With magnetic neutron diffraction in longitudinal fields for $Nb_{0.985}Fe_{2.015}$ the extent of the spin density wave in to the H‖c-T phase diagram has been mapped by measuring the SDW peak at (1 0 -2+ℓ_{SDW}) additionally the field evolution of onset of ferromagnetism has been measured at the weak nuclear position at (1 0 2). The resulting magnetic phase diagram reveals the location of tricritical point (TCP) at H_{tr}=53 mT and T_{tr} = 26.5 K.

In magnetic neutron diffraction $Nb_{0.980}Fe_{2.020}$ in transverse field the same reciprocal space positions have been used to map out the H‖a-T phase diagram. The suppression of SDW order has been observed at critical field of 1 T. The FM-PM transition can be followed up to about 2.5 T until where it remains constant at about 34 K. So it was not possible to follow the expected suppression of the unmasked FM-PM to low temperature in this measurement.

With inelastic neutron scattering in longitudinal field the evolution of spin fluctuations across the QCP has been observed in $Nb_{0.985}Fe_{2.015}$. At low temperature in the ferromagnetic phase an unusual dispersion with the minimum in the dispersion near the SDW wave vector has been observed at H_{tr}=53 mT. The TCP has been found to feature simultaneously enhanced and soft FM and SDW spin fluctuations. Along the SDW-PM transition line and at the TCP the spin fluctuation spectra show fairly conventional features. However the SDW spin fluctuation

stay more soft and enhanced at higher fields than expected.

With inelastic neutron scattering in $Nb_{0.980}Fe_{2.020}$ system in transverse field the ferromagnetic low energy excitations at (0 0 2) have been observed to show softening and an enhancement at low temperature that indicate existence of a field induced unmasked ferromagnetic quantum critical point at a H=3.6 T. How ever the possibility of quantum crossover cannot be excluded.

In the future, polarised neutron diffraction measurements that have partially been done during this thesis project by me using POLI instrument at FRM-2 reactor, Germany could reveal details of the SDW and FM phases and finally settle whether $NbFe_2$ could be a ferrimagnet and presented a rare case of ferrimagnetic quantum criticality. Also, the growth of more Fe rich crystals for neutron scattering would allow projects of measuring the low-energy magnetic excitations in the vicinity of the Lifshitz point in the zero field composition-temperature phase diagram. Measurements of stoichiometric crystals suitable for neutron scattering could allow to explore the low-energy magnetic excitations in the vicinity of the suspected Quantum Tricritical Point [51].

A

Longitudinal field evolution of magnetic excitation spectrum in Fe-rich $NbFe_2$ - additional data

A.1 H=0T, T=30K

Table A.1: The Fitting details of the magnetic signals measured at H=0T, T=30K.

H=0 T, T= 30 K			
(0 0 ℓ)	**FitFunction**	**No. Gaussian Peak**	**Constant**
2	DHO	1	NO
2.05	DHO	2	NO
2.1	DHO	1	NO
2.15	DHO	1	NO
2.2	DHO	1	NO
2.25	DHO	1	NO
2.3	DHO	1	NO
2.4	DHO	2	NO

A.2 H=53 mT, T=27 K

Table A.2: The Fitting details of the magnetic signals measured at H=53 mT, T=27 K.

H=53 mT, T= 27 K			
(0 0 ℓ)	**FitFunction**	**No. Gaussian Peak**	**Constant**
2	DHO	1	NO
2.05	DHO	2	NO
2.1	DHO	1	NO
2.15	DHO	1	NO
2.2	DHO	1	NO
2.25	DHO	1	NO
2.3	DHO	1	NO
2.4	ODHO	2	NO

A.3 H=100 mT, T=31 K

Table A.3: The Fitting details of the magnetic signals measured at H=100 mT, T=31 K.

H=100 mT, T= 31 K			
(0 0 ℓ)	**FitFunction**	**No. Gaussian Peak**	**Constant**
2	DHO	1	NO
2.05	DHO	2	NO
2.1	DHO	1	NO
2.15	DHO	1	NO
2.2	DHO	1	NO
2.25	DHO	1	NO
2.3	DHO	1	NO
2.4	ODHO	1	NO

A.4 H=200 mT, T=37 K

Table A.4: The Fitting details of the magnetic signals measured at H=200 mT, T=37 K.

H=200 mT, T= 37 K			
(0 0 ℓ)	**FitFunction**	**No. Gaussian Peak**	**Constant**
2	DHO	1	NO
2.05	DHO	2	NO
2.1	DHO	1	NO
2.15	DHO	1	NO
2.2	DHO	1	NO
2.25	DHO	1	NO
2.3	DHO	1	NO
2.4	ODHO	2	NO

A.5 H=53 mT, T=3 K

Table A.5: The Fitting details of the magnetic signals measured at H=53 mT, T=3 K.

H=200 mT, T= 37 K			
(0 0 ℓ)	**FitFunction**	**No. Gaussian Peak**	**Constant**
2	DHO	1	NO
2.05	DHO	2	NO
2.1	DHO	1	NO
2.15	DHO	1	NO
2.2	DHO	1	NO
2.25	DHO	1	NO
2.3	DHO	1	NO
2.4	ODHO	1	NO

A.6 Additional measurements

Table A.6: The Fitting details of the magnetic signals measured at (H=25 mT, T=30 K), (H=75 mT, T=29 K) and (H=200 mT, T=3 K)

H=25mT, T= 30 K			
(0 0 ℓ)	**FitFunction**	**No. Gaussian Peak**	**Constant**
2	DHO	1	NO
2.05	DHO	2	NO
H=75mT, T= 29 K			
(0 0 ℓ)	**FitFunction**	**No. Gaussian Peak**	**Constant**
2	DHO	1	NO
2.05	DHO	2	NO
H=200mT, T= 3 K			
(0 0 ℓ)	**FitFunction**	**No. Gaussian Peak**	**Constant**
2	DHO	1	NO

B

Transverse field evolution of magnetic excitation spectrum in Fe-rich $NbFe_2$ - additional data

B.1 Fit details of low energy excitations at Q_{FM} at different fields

Table B.1: The Fitting details of the magnetic signals measured at Q_{FM} with different magnetic fields.

LET			
Magnetic Field (H)	FitFunction	No. Gaussian Peak	Constant
0	DHO	1	Yes
2.75	DHO	1	Yes
3.5	ODHO	1	Yes
4.25	ODHO	1	Yes

LLB-I			
Magnetic Field (H)	FitFunction	No. Gaussian Peak	Constant
0.5	DHO	1	Yes
2	DHO	1	Yes
3.5	ODHO	1	Yes
5	ODHO	1	Yes

LLB-II			
Magnetic Field (H)	FitFunction	No. Gaussian Peak	Constant
0	DHO	1	Yes
2.5	DHO	1	Yes
2.75	DHO	1	Yes
3	DHO	1	Yes
3.25	DHO	1	Yes
3.5	ODHO	1	Yes
3.6	ODHO	1	Yes
3.75	ODHO	1	Yes
4	ODHO	1	Yes
4.25	ODHO	1	Yes
4.5	ODHO	1	Yes

B.2 H < H_c

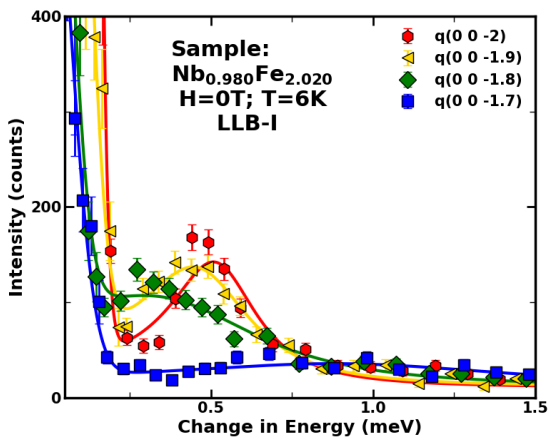

Figure B.1: Representative plots of the magnetic excitations measured across Q_{FM} in the ℓ direction at magnetic field H=0T, T=6 K with LLB-I . The magnetic excitations are fitted (solid lines) with a damped harmonic oscillator model.

Table B.2: The Fitting details of the magnetic signals measured at different magnetic fields with LET.

LET						
(0 0 ℓ)	**H=0T, T= 2K**			**H=2.75T, T= 2K**		
	FitFunction	No. Gaussian Peak	Constant	FitFunction	No. Gaussian Peak	Constant
-2.30	DHO	2	Yes	DHO	2	Yes
-2.25	DHO	2	Yes	DHO	2	Yes
-2.20	DHO	2	Yes	DHO	2	Yes
-2.15	DHO	2	Yes	DHO	2	Yes
-2.10	DHO	2	Yes	DHO	2	Yes
-2.05	DHO	1	Yes	DHO	1	Yes
-2.00	DHO	1	Yes	DHO	1	Yes
-1.95	DHO	1	Yes	DHO	1	Yes
-1.90	DHO	2	Yes	DHO	2	Yes
-1.85	DHO	2	Yes	DHO	2	Yes
-1.80	DHO	2	Yes	DHO	2	Yes
-1.75	DHO	2	Yes	DHO	2	Yes
-1.70	DHO	2	Yes	DHO	2	Yes

Table B.3: The Fitting details of the magnetic signals measured at different magnetic fields with LLB-I.

LLB-I , 4F2				
Magnetic Field	(0 0 ℓ)	FitFunction	No. Gaussian Peak	Constant
H=0T, T= 6K	-2.00	DHO	1	Yes
	-1.90	DHO	2	Yes
	-1.80	DHO	1	Yes
	-1.70	DHO	1	Yes
	-1.70	DHO	1	Yes
H=0.5T, T= 4K	-2.00	DHO	1	Yes
	-1.95	DHO	2	Yes
	-1.90	DHO	2	Yes
	-1.80	DHO	1	Yes
	-1.70	DHO	1	Yes
	-1.70	DHO	1	Yes
H=2T, T= 4K	-2.00	DHO	1	Yes
	-1.95	DHO	2	Yes
	-1.90	DHO	2	Yes
	-1.80	DHO	2	Yes
	-1.70	DHO	1	Yes
	-1.70	DHO	1	Yes

B.3 H = H_c

Table B.4: The Fitting details of the magnetic signals measured in the critical regime with LET and LLB-II.

Magnetic Field and Instrument	(0 0 ℓ)	FitFunction	No. Gaussian Peak	Constant
H=3.5T, T= 2K LET	-2.30	ODHO	2	Yes
	-2.25		2	
	-2.20		2	
	-2.15		2	
	-2.10		2	
	-2.05		1	
	-2.00		1	
	-1.95		1	
	-1.90		2	
	-1.85		2	
	-1.80		2	
	-1.75		2	
	-1.70		2	
H=3.6T, T= 1.7K LLB-II, 4F2	2.05	ODHO	2	Yes
	2.00		1	
	1.95		2	
	1.90		2	
	1.85		1	
	1.80		1	
	1.75		1	
	1.70		1	
	1.65		1	

B.4 H > H_c

Table B.5: The Fitting details of the magnetic signals measured above the critical regime with LET .

(0 0 ℓ)	H=4.25T, T= 2K - LET		
	FitFunction	No. Gaussian Peak	Constant
-2.30	ODHO	2	Yes
-2.25		2	
-2.20		2	
-2.15		2	
-2.10		2	
-2.05		1	
-2.00		1	
-1.95		1	
-1.90		2	
-1.85		2	
-1.80		2	
-1.75		2	
-1.70		1	

B.5 h dependence of magnetic excitations at the critical field (H_c) region

Table B.6: The Fitting details of the magnetic signals measured in h direction across Q_{FM} in the critical regime with LLB-II.

LLB-II, 4F2			
(h 0 2)	**H=3.6T, T= 1.7K**		
	FitFunction	No. Gaussian Peak	Constant
0.05	ODHO	1	Yes
0.035		1	
0.02		2	
0		1	
-0.02		3	
-0.05		2	

B.6 Temperature dependence of magnetic excitations at the critical field (H_c) region

Table B.7: The Fitting details of the magnetic signals measured at high temperature in the critical regime with LET.

(0 0 ℓ)	H=3.5T, T= 37.5K -LET		
	FitFunction	No. Gaussian Peak	Constant
-2.30	DHO	2	Yes
-2.25	DHO	2	Yes
-2.20	DHO	2	Yes
-2.15	DHO	2	Yes
-2.10	DHO	2	Yes
-2.05	DHO	1	Yes
-2.00	DHO	1	Yes
-1.95	DHO	1	Yes
-1.90	DHO	2	Yes
-1.85	DHO	2	Yes
-1.80	DHO	2	Yes
-1.75	DHO	2	Yes
-1.70	DHO	1	Yes

B.7 Energy shift correction

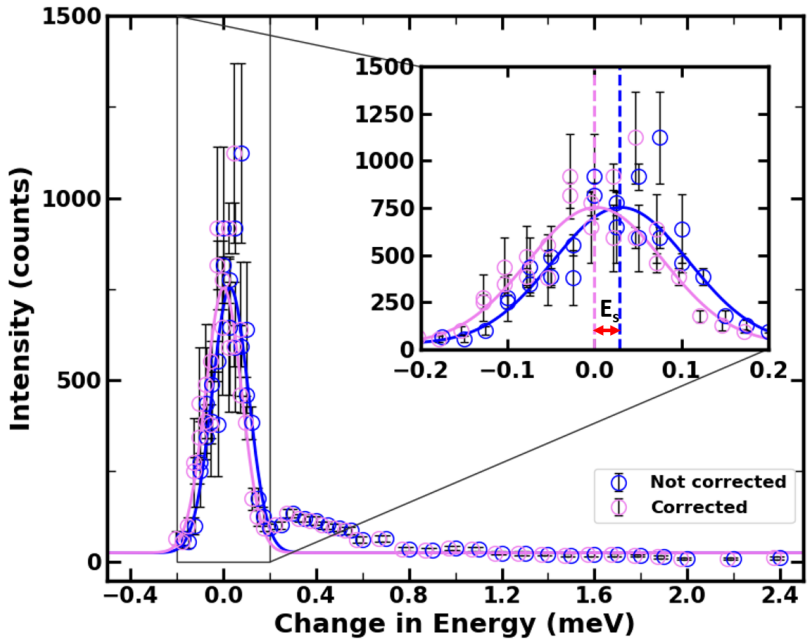

Figure B.2: Representative illustration of the energy shift correction for the Q position (0 0 -1.8) measured at H=0 T and T=6 K during LLB-I at 4F2. The data shows the energy scan with uncorrected (blue) and corrected (violet) energy shift. The inset shows the magnified view of the elastic line with uncorrected Gaussian fit centred at E_s (blue dased line) and energy shift corrected at 0 meV (violet dashed line). The solid lines represents the Gaussian fits (Equation.(B.1))

Figure.(B.2) illustrates the energy shift in the measured data collected during LLB-I at 4F2 for the representative Q position (0 0 -1.8) at H = 0 T and T = 6 K. The Figure consists of energy scan with uncorrected (blue) and corrected (violet) scattering data. We obtained the energy shift (E_s) by fitting three parameter Gaussian function with a constant given in Equation.(B.1),

Gaussian function:

$$f(x) \longmapsto A\exp\Big(-\frac{(\mathrm{x}-\mathrm{b})^2}{2\sigma^2}\Big) + \mathrm{Cst} \tag{B.1}$$

where A is the amplitude of the Gaussian peak, b is the centre of the peak, σ is the peak width and Cst is a constant. The data was then corrected by adding the offset energy (E_s) to the energy transfer.

Bibliography

[1] S. L. Sondhi, S. M. Girvin, J. P. Carini, and D. Shahar, "Continuous quantum phase transitions," *Rev. Mod. Phys.*, vol. 69, pp. 315–333, Jan 1997.

[2] J. Scholz, J. Kelso, and G. Schöner, "Nonequilibrium phase transitions in coordinated biological motion: Critical slowing down and switching time," *Physics Letters A*, vol. 123, no. 8, pp. 390–394, 1987.

[3] S. Sachdev, "Quantum criticality: competing ground states in low dimensions," *Science*, vol. 288, no. 5465, pp. 475–480, 2000.

[4] P. Coleman and A. J. Schofield, "Quantum criticality," *Nature*, vol. 433, no. 7023, pp. 226–229, 2005.

[5] O. Stockert, J. Arndt, E. Faulhaber, C. Geibel, H. S. Jeevan, S. Kirchner, M. Loewenhaupt, K. Schmalzl, W. Schmidt, Q. Si, and F. Steglich, "Magnetically driven superconductivity in CeCu2Si2," *Nature Physics*, vol. 7, no. 2, pp. 119–124, 2011. [Online]. Available: https://doi.org/10.1038/nphys1852

[6] F. M. Grosche, I. R. Walker, S. R. Julian, N. D. Mathur, D. M. Freye, M. J. Steiner, and G. G. Lonzarich, "Superconductivity on the threshold of magnetism in CePd2si2and CeIn3," *Journal of Physics: Condensed Matter*, vol. 13, no. 12, pp. 2845–2860, mar 2001.

[7] S. Jiang, H. Xing, G. Xuan, C. Wang, Z. Ren, C. Feng, J. Dai, Z. Xu, and G. Cao, "Superconductivity up to 30 k in the vicinity of the quantum critical point in BaFe2(as1-xPx)2," *Journal of Physics: Condensed Matter*, vol. 21, no. 38, p. 382203, aug 2009.

[8] T. Vojta, D. Belitz, T. R. Kirkpatrick, and R. Narayanan, "Quantum critical behavior of itinerant ferromagnets," *Annalen der Physik*, vol. 8, no. 7-9, pp. 593–602, 1999.

[9] A. V. Chubukov, C. Pépin, and J. Rech, "Instability of the quantum-critical point of itinerant ferromagnets," *Physical review letters*, vol. 92, no. 14, p. 147003, 2004.

[10] C. Pfleiderer, S. Julian, and G. Lonzarich, "Non-Fermi-liquid nature of the normal state of itinerant-electron ferromagnets," *Nature*, vol. 414, no. 6862, p. 427, 2001.

[11] D. Belitz, T. Kirkpatrick, and J. Rollbühler, "Tricritical behavior in itinerant quantum ferromagnets," *Physical review letters*, vol. 94, no. 24, p. 247205, 2005.

[12] T. R. Kirkpatrick and D. Belitz, "Universal low-temperature tricritical point in metallic ferromagnets and ferrimagnets," *Phys. Rev. B*, vol. 85, p. 134451, Apr 2012.

[13] R. B. Griffiths, "Thermodynamics Near the Two-Fluid Critical Mixing Point in He^3 - He^4," *Phys. Rev. Lett.*, vol. 24, pp. 715–717, Mar 1970.

[14] M. Uhlarz, C. Pfleiderer, and S. M. Hayden, "Quantum Phase Transitions in the Itinerant Ferromagnet $ZrZn_2$," *Phys. Rev. Lett.*, vol. 93, p. 256404, Dec 2004.

[15] V. Taufour, D. Aoki, G. Knebel, and J. Flouquet, "Tricritical Point and Wing Structure in the Itinerant Ferromagnet UGe_2," *Phys. Rev. Lett.*, vol. 105, p. 217201, Nov 2010.

[16] S. Nakamura, T. Sakakibara, Y. Shimizu, S. Kittaka, Y. Kono, Y. Haga, J. c. v. Pospíšil, and E. Yamamoto, "Wing structure in the phase diagram of the Ising ferromagnet URhGe close to its tricritical point investigated by angle-resolved magnetization measurements," *Phys. Rev. B*, vol. 96, p. 094411, Sep 2017.

[17] M. Otero-Leal, F. Rivadulla, S. S. Saxena, K. Ahilan, and J. Rivas, "Nature of the high-pressure tricritical point in mnsi," *Phys. Rev. B*, vol. 79, p. 060401, Feb 2009.

[18] T. Goto, Y. Shindo, H. Takahashi, and S. Ogawa, "Magnetic properties of the itinerant metamagnetic system $Co(S_{1-x}Se_x)_2$ under high magnetic fields and high pressure," *Phys. Rev. B*, vol. 56, pp. 14 019–14 028, Dec 1997.

[19] U. S. Kaluarachchi, S. L. Bud'ko, P. C. Canfield, and V. Taufour, "Tricritical wings and modulated magnetic phases in LaCrGe3 under pressure," *Nature Communications*, vol. 8, no. 1, p. 546, 2017.

[20] Y. J. Uemura, T. Goko, I. M. Gat-Malureanu, J. P. Carlo, P. L. Russo, A. T. Savici, A. Aczel, G. J. MacDougall, J. A. Rodriguez, G. M. Luke, S. R. Dunsiger, A. McCollam, J. Arai, C. Pfleiderer, P. Böni, K. Yoshimura, E. Baggio-Saitovitch, M. B. Fontes, J. Larrea, Y. V. Sushko, and J. Sereni, "Phase separation and suppression of critical dynamics at

quantum phase transitions of MnSi and (Sr1-xCax)RuO3," *Nature Physics*, vol. 3, no. 1, pp. 29–35, 2007.

[21] N. Doiron-Leyraud, I. Walker, L. Taillefer, M. Steiner, S. Julian, and G. Lonzarich, "Fermi-liquid breakdown in the paramagnetic phase of a pure metal," *Nature*, vol. 425, no. 6958, p. 595, 2003.

[22] M. Brando, D. Belitz, F. M. Grosche, and T. R. Kirkpatrick, "Metallic quantum ferromagnets," *Rev. Mod. Phys.*, vol. 88, p. 025006, May 2016.

[23] S. S. Saxena, P. Agarwal, K. Ahilan, F. M. Grosche, R. K. W. Haselwimmer, M. J. Steiner, E. Pugh, I. R. Walker, S. R. Julian, P. Monthoux, G. G. Lonzarich, A. Huxley, I. Sheikin, D. Braithwaite, and J. Flouquet, "Superconductivity on the border of itinerant-electron ferromagnetism in UGe2," *Nature*, vol. 406, no. 6796, pp. 587–592, 2000. [Online]. Available: https://doi.org/10.1038/35020500

[24] N. T. Huy, A. Gasparini, D. E. de Nijs, Y. Huang, J. C. P. Klaasse, T. Gortenmulder, A. de Visser, A. Hamann, T. Görlach, and H. v. Löhneysen, "Superconductivity on the border of weak itinerant ferromagnetism in ucoge," *Phys. Rev. Lett.*, vol. 99, p. 067006, Aug 2007. [Online]. Available: https://link.aps.org/doi/10.1103/PhysRevLett.99.067006

[25] G. Abdul-Jabbar, D. A. Sokolov, C. D. O?neill, C. Stock, D. Wermeille, F. Demmel, F. Krüger, A. G. Green, F. Lévy-Bertrand, B. Grenier *et al.*, "Modulated magnetism in PrPtAl," *Nature Physics*, vol. 11, no. 4, p. 321, 2015.

[26] S. Grigera, R. Perry, A. Schofield, M. Chiao, S. Julian, G. Lonzarich, S. Ikeda, Y. Maeno, A. Millis, and A. Mackenzie, "Magnetic field-tuned quantum criticality in the metallic ruthenate $Sr_3Ru_2O_7$," *Science*, vol. 294, no. 5541, pp. 329–332, 2001.

[27] D. Moroni-Klementowicz, M. Brando, C. Albrecht, W. J. Duncan, F. M. Grosche, D. Grüner, and G. Kreiner, "Magnetism in Nb_{1-y} Fe_{2+y}: Composition and magnetic field dependence," *Physical Review B - Condensed Matter and Materials Physics*, vol. 79, no. 22, pp. 1–11, 2009.

[28] P. G. Niklowitz, M. Hirschberger, M. Lucas, P. Cermak, A. Schneidewind, E. Faulhaber, J.-M. Mignot, W. J. Duncan, A. Neubauer, C. Pfleiderer, and F. M. Grosche, "Ultrasmall Moment Incommensurate Spin Density Wave Order Masking a Ferromagnetic Quantum Critical Point in $NbFe_2$," *Phys. Rev. Lett.*, vol. 123, p. 247203, Dec 2019.

[29] M. Schmid, "Schematic view of the spins in a material with ferromagnetic ordering," December 2006, accessed on 09.12.2021. [Online]. Available: https://commons.wikimedia.org/wiki/File:Ferromagnetic_ordering.svg

[30] S. Blundell, *Magnetism in condensed matter.* Oxford University Press, 2001.

[31] M. Schmid. (2006, December) Schematic view of the spins in a material with antiferromagnetic ordering. Accessed on 09.12.2021. [Online]. Available: https://commons.wikimedia.org/wiki/File:Antiferromagnetic_ordering.svg

[32] M. Schmid. (2006, December) Schematic view of the spins in a material with ferrimagnetic ordering. Accessed on 09.12.2021. [Online]. Available: https://commons.wikimedia.org/wiki/File:Ferrimagnetic_ordering.svg

[33] G. Jaeger, "The Ehrenfest Classification of Phase Transitions: Introduction and Evolution," *Archive for History of Exact Sciences*, vol. 53, no. 1, pp. 51–81, 1998.

[34] B. Cowan, *Topics In Statistical Mechanics.* Imperial College Press, 2005.

[35] Dr Rudolf Winter. Landau theory. Accessed on 10.12.2021. [Online]. Available: https://users.aber.ac.uk/ruw/teach/334/landau.php

[36] M. Vojta, "Quantum phase transitions," *Reports on Progress in Physics*, vol. 66, no. 12, p. 2069, nov 2003. [Online]. Available: https://dx.doi.org/10.1088/0034-4885/66/12/R01

[37] J. Als-Nielsen and R. J. Birgeneau, "Mean filed theory, the ginzburge criterion, and marginal dimensionality of phase transitions," *Am. J. Phys*, vol. 45, no. 6, June 1977. [Online]. Available: https://aapt.scitation.org/doi/10.1119/1.11019

[38] Vectorized version by AG Caesar, original by DG85. (2018, Dmarch) Phase diagram of a second order quantum phase transition. Accessed on 10.12.2021. [Online]. Available: https://commons.wikimedia.org/wiki/File:QuantumPhaseTransition.svg

[39] G. Lonzarich and M. Springford, *Electron: A Centenary Volume.* Cambridge University Press Cambridge, 1997.

[40] Y. Takahashi, *Spin fluctuation theory of itinerant electron magnetism.* Springer, 2013, vol. 9.

[41] A. J. Millis, "Effect of a nonzero temperature on quantum critical points in itinerant fermion systems," *Phys. Rev. B*, vol. 48, pp. 7183–7196, Sep 1993. [Online]. Available: https://link.aps.org/doi/10.1103/PhysRevB.48.7183

[42] D. Tompsett, R. Needs, F. Grosche, and G. Lonzarich, "Doping-driven magnetic instabilities and quantum criticality of $NbFe_2$," *Physical Review B*, vol. 82, no. 15, p. 155137, 2010.

[43] S. Ishida, S. Asano, and J. Ishida, "Electronic Structures and Magnetic Properties of the C14 Laves Phase Compounds $ZrMn_2$, $TiFe_2$ and $NbFe_2$," *Journal of the Physical Society of Japan*, vol. 54, no. 10, pp. 3925–3933, 1985.

[44] S. Asano and S. Ishida, "Magnetism and crystal structure of laves phase compounds," *Journal of Physics F: Metal Physics*, vol. 18, no. 3, pp. 501–515, mar 1988.

[45] S. Asano and S. Ishida, "Competition of magnetism in iron laves phase compounds," *Journal of Physics: Condensed Matter*, vol. 1, no. 44, pp. 8501–8508, nov 1989.

[46] N. Takayama and M. Shimizu, "Electronic structure and paramagnetic susceptibility of the C14 Laves phase compound $NbFe_2$," *Journal of Physics F: Metal Physics*, vol. 18, no. 5, pp. L83–L86, may 1988.

[47] A. Subedi and D. J. Singh, "Band structure and itinerant magnetism in quantum critical $NbFe_2$," *Phys. Rev. B*, vol. 81, p. 024422, Jan 2010.

[48] Y. Yamada and A. Sakata, "Weak Antiferromagnetism in $NbFe_2$," *Journal of the Physical Society of Japan*, vol. 57, no. 1, pp. 46–49, 1988.

[49] M. Crook and R. Cywinski, "Magnetic transition in nb1-yfe2+y," *Journal of Magnetism and Magnetic Materials*, vol. 140-144, pp. 71–72, 1995, international Conference on Magnetism.

[50] M. Shiga and Y. Nakamura, "Magnetic properties of stoichiometric and off-stoichiometric nbfe2," *Journal of the Physical Society of Japan*, vol. 56, no. 11, pp. 4040–4046, 1987.

[51] S. Friedemann, W. J. Duncan, M. Hirschberger, T. W. Bauer, R. Küchler, A. Neubauer, M. Brando, C. Pfleiderer, and F. M. Grosche, "Quantum tricritical points in $NbFe_2$," *Nature Physics*, vol. 14, no. 1, pp. 62–67, 2018.

[52] T. D. Haynes, I. Maskery, M. W. Butchers, J. A. Duffy, J. W. Taylor, S. R. Giblin, C. Utfeld, J. Laverock, S. B. Dugdale, Y. Sakurai, M. Itou, C. Pfleiderer, M. Hirschberger, A. Neubauer, W. Duncan, and F. M. Grosche, "Ferrimagnetism in Fe-rich $NbFe_2$," *Phys. Rev. B*, vol. 85, p. 115137, Mar 2012.

[53] M. Kurisu, Y. Andoh, and Y. Yamada, "Magnetic properties of $NbFe_2$ single crystal," *Physica B: Condensed Matter*, vol. 237-238, pp. 493–495, 1997, proceedings of the Yamada Conference XLV, the International Conference on the Physics of Transition Metals.

[54] M. Brando, W. Duncan, D. Moroni-Klementowicz, C. Albrecht, D. Grüner, R. Ballou, and F. Grosche, "Logarithmic Fermi-liquid breakdown in $NbFe_2$," *Physical review letters*, vol. 101, no. 2, p. 026401, 2008.

[55] M. T. Lucas, "Order and excitations near the spin density-wave masked ferromagnetic quantum critical point in $Nb_{1-y}Fe_{2+y}$," Ph.D. dissertation, Royal Holloway University of London, 2020.

[56] Pfleiderer, C and Böni, P and Franz, C and Keller, T and Neubauer, A and Niklowitz, PG and Schmakat, P and Schulz, M and Huang, Y-K and Mydosh, JA and others, "Search for electronic phase separation at quantum phase transitions," *Journal of Low Temperature Physics*, vol. 161, no. 1, pp. 167–181, 2010.

[57] A. Neubauer, "Single crystal growth of intermetallic compounds with unusual low temperature properties," Ph.D. dissertation, Technical University of Munich, 2011.

[58] S. Friedemann, M. Brando, W. J. Duncan, A. Neubauer, C. Pfleiderer, and F. M. Grosche, "Ordinary and intrinsic anomalous Hall effects in $Nb_{1-y}Fe_{2+y}$," *Phys. Rev. B*, vol. 87, p. 024410, Jan 2013. [Online]. Available: https://link.aps.org/doi/10.1103/PhysRevB.87.024410

[59] N. Pottier, "Physique statistique hors d'équilibre : équation de Boltzmann, réponse linéaire." Sep. 2006, lecture. [Online]. Available: https://cel.archives-ouvertes.fr/cel-00092930

[60] J. Chadwick, "Possible Existence of a Neutron," *Nature*, vol. 129, no. 3252, p. 312, 1932.

[61] R. P. Feynman, *Feynman lectures on physics.* Boston, MA: Addison Wesley Longman, 1970.

[62] G. L. Squires, *Introduction to the Theory of Thermal Neutron Scattering*, 3rd ed. Cambridge University Press, 2012.

[63] (2019, May) An illustration of the scattering geometry. Accessed on 05.12.2021. [Online]. Available: https://pan-learning.org/wiki/index.php/File:Fig2dot1v3.png

[64] G. Shirane, S. M. Shapiro, and J. M. Tranquada, *Neutron scattering with a triple-axis spectrometer: basic techniques.* Cambridge University Press, 2002.

[65] I. A. Zaliznyak and S. H. LEE, "Magnetic neutron scattering." [Online]. Available: https://www.osti.gov/biblio/15009517

[66] J. M. Carpenter and C.-K. Loong, *Elements of Slow-Neutron Scattering: Basics, Techniques, and Applications.* Cambridge University Press, 2015.

[67] Raymond, Stéphane, "Magnetic excitations," *JDN*, vol. 13, p. 02003, 2014. [Online]. Available: https://doi.org/10.1051/sfn/20141302003

[68] (2013) Experimental facilities. Laboratoire Lèon Brillouin. Accessed on 07.12.2021. [Online]. Available: https://www-llb.cea.fr/en/fr-en/spectros-llb.pdf

[69] "4f2 : Cold neutron three axis spectrometer," 2003. [Online]. Available: https://www-drecam.cea.fr/llb/spectros/pdf/4f2-llb.pdf

[70] R. Georgii, T. Weber, G. Brandl, M. Skoulatos, M. Janoschek, S. Mühlbauer, C. Pfleiderer, and P. Böni, "The multi-purpose three-axis spectrometer (TAS) MIRA at FRM IIs," *Nuclear Instruments and Methods in Physics Research Section A: Accelerators, Spectrometers, Detectors and Associated Equipment*, vol. 881, pp. 60–64, 2018.

[71] R. Bewley, J. Taylor, and S. Bennington., "Let, a cold neutron multi-disk chopper spectrometer at isis," *Nuclear Instruments and Methods in Physics Research Section A: Accelerators, Spectrometers, Detectors and Associated Equipment*, vol. 637, no. 1, pp. 128–134, 2011.

[72] R. Ewings, A. Buts, M. Le, J. Van Duijn, I. Bustinduy, and T. Perring, "Horace: software for the analysis of data from single crystal spectroscopy experiments at time-of-flight neutron instruments," *Nuclear Instruments and Methods in Physics Research Section A: Accelerators, Spectrometers, Detectors and Associated Equipment*, vol. 834, pp. 132–142, 2016.

[73] J. N. Poulten, "Composition-tuned magnetic order and excitations in $nb_{1-x}fe_{2+x}$ and pressure-induced changes in structural and optical properties of cu_2oseo_3," Ph.D. dissertation, Royal Holloway University of London, 2018.